AD-A098 966   CALIFORNIA UNIV BERKELEY DEPT OF MATERIALS SCIENCE A--ETC   F/G 11/2
IMPACT DAMAGE AND EROSION OF CERAMICS AND COMPOSITES.(U)
DEC 80   A G EVANS, N BURLINGAME, S S CHIANG   N00014-79-C-0159

UNCLASSIFIED   NL

1 OF 3
AD
A098966

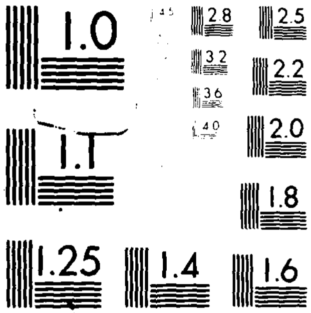
1.0
4.5
2.8
2.5
3.2
2.2
3.6
4.0
2.0
1.1
1.8
1.25
1.4
1.6

MICROCOPY RESOLUTION TEST CHART

NATIONAL BUREAU OF STANDARDS-1963-A

LEVEL II

AD A098966

12

IMPACT DAMAGE AND EROSION OF CERAMICS AND COMPOSITES

Final Report to
Office of Naval Research
Contract No.: N00014-79-C-0159
January 1, 1930 - December 31, 1930

by

A. G. Evans
University of California
Berkeley, California 94720

and

N. Burlingame, S. S. Chiang, D. R. Clark, M. Drory,
K. T. Faber, W. L. Fraser, M. E. Gulden, M. D. Huang,
W. Kennedy, W. M. Kriven, D. B. Marshall, J. L. Routbort,
R. O. Scattergood, D. K. Shetty, A. V. Virkar

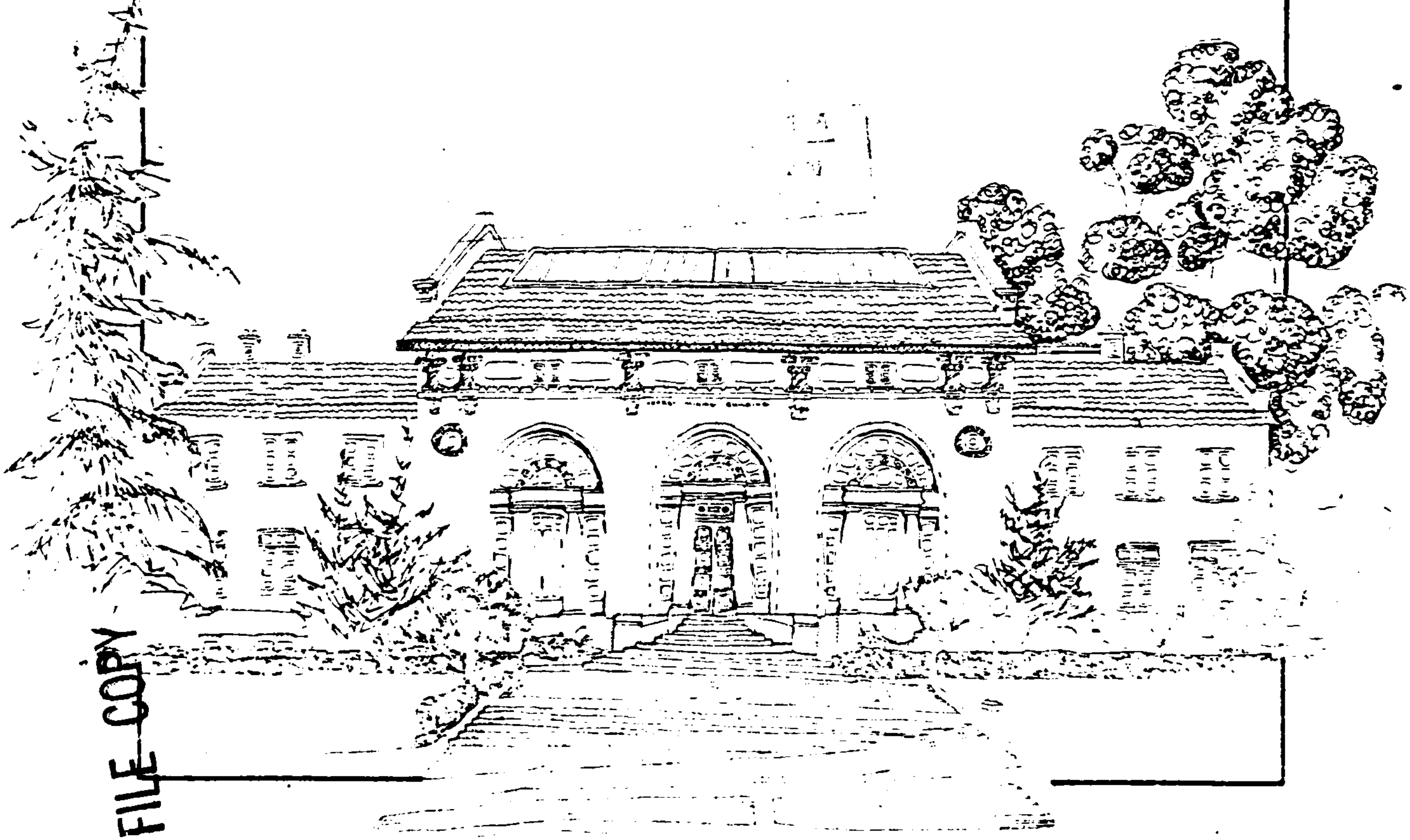

DTIC FILE COPY

Reproduction in whole or in part is permitted for any purpose of the United States Government.

81 4

SECURITY CLASSIFICATION OF THIS PAGE (When Data Entered)

REPORT DOCUMENTATION PAGE	READ INSTRUCTIONS BEFORE COMPLETING FORM
1. REPORT NUMBER / 2. GOVT ACCESSION NO. AD-A098966	3. RECIPIENT'S CATALOG NUMBER
4. TITLE (and Subtitle) Impact Damage and Erosion of Ceramics and Composites.	5. TYPE OF REPORT & PERIOD COVERED Final Report Jan [redacted] Dec [redacted] 1980
	6. PERFORMING ORG. REPORT NUMBER (21)
7. AUTHOR(s) A. G. Evans	8. CONTRACT OR GRANT NUMBER(s) N00014-79-C-0159
9. PERFORMING ORGANIZATION NAME AND ADDRESS Materials Science and Mineral Engineering University of California Berkeley, CA 94720	10. PROGRAM ELEMENT, PROJECT, TASK AREA & WORK UNIT NUMBERS
11. CONTROLLING OFFICE NAME AND ADDRESS Office of Naval Research, Code 471 Arlington, VA 22217	12. REPORT DATE 31 Dec~~ember 31,~~ 1980
	13. NUMBER OF PAGES 230
14. MONITORING AGENCY NAME & ADDRESS (if different from Controlling Office) (12)	15. SECURITY CLASS. (of this report) Unclassified
	15a. DECLASSIFICATION DOWNGRADING SCHEDULE

16. DISTRIBUTION STATEMENT (of this Report)

[redacted]

17. DISTRIBUTION STATEMENT (of the abstract entered in Block 20, if different from Report)

18. SUPPLEMENTARY NOTES

19. KEY WORDS (Continue on reverse side if necessary and identify by block number)

Ceramics, fracture, martensite transformations, thermal shock, indentation fracture, grain size, toughness

20. ABSTRACT (Continue on reverse side if necessary and identify by block number)

Studies of the mechanical strength of ceramics~~ have~~ been conducted. These range from studies of toughness to indentation fracture, thermal shock and erosion. The central theme of this report concerns the study of those facets of mechanical behaviors that influence the structural integrity of ceramic components.

406137

DD FORM 1 JAN 73 1473 EDITION OF 1 NOV 65 IS OBSOLETE

TECHNICAL ARTICLES

I. A. V. Virkar, D. K. Shetty and A. G. Evans, "On the Grain Size Dependence of Strength."

II. A. G. Evans, N. Burlingame, M. Drory and W. Kriven, "Martensite Transformations in Zirconia: Particle Size Effects and Toughening."

III. K. T. Faber, M. D. Huang, and A. G. Evans, "Quantitative Studies of Thermal Shock in Ceramics: Based on a Novel Test Technique."

IV. A. G. Evans and K. T. Faber, "Toughening of Ceramics by Circumferential Microcracking."

V. A. G. Evans and D. R. Clark, "Residual Stresses & Microcracking Induced by Thermal Contraction Inhomogeneity."

VI. S. S. Chiang, D. B. Marshall and A. G. Evans, "A Simple Method for Adhesion Measurements."

VII. W. M. Kriven, W. L. Fraser and S. W. Kennedy, "The Martensite Crystallography of Tetragonal Zirconia."

VIII. A. G. Evans and D. B. Marshall, "Wear Mechanics in Ceramics."

IX. D. B. Marshall, A. G. Evans, M. E. Gulden, J. L. Routbort and R. O. Scattergood, "Particle Size Distribution Effects on Solid Particle Erosion in Brittle Materials."

UTEC 80-077

CHAPTER 1

ON THE GRAIN-SIZE DEPENDENCE OF STRENGTH

by

Anil V. Virkar[*], D. K. Shetty[+] and A. G. Evans[†]

Accession For
NTIS GRA&I ☒
DTIC TAB ☐
Unannounced ☐
Justification Per Letter on File
By
Distribution/
Availability Codes
A

[*] Department of Materials Science & Engineering,
University of Utah, Salt Lake City, Utah 84112

[+] Batelle Laboratories, Columbus, Ohio

[†] Materials and Molecular Research Division, Lawrence
Berkeley Laboratory and Department of Materials Science
and Mineral Engineering, University of California,
Berkeley, California 94720

Recently, Evans[1] has presented a dimensional analysis of the dependence of strength on grain size, which extended some earlier conclusions established by Singh et al.[2] In this analysis, a variation in local fracture toughness, K^c_{eff}, with crack length, a, was used to determine the fracture criticality. Specifically, the fracture toughness was chosen to vary between the single crystal K^c_s and polycrystal K^c_p values. This choice permitted a range of K^c_p/K^c_s to be identified wherein stable crack growth preceded fracture; causing the strength within this range to become independent of the initial crack length. This behavior resulted in the natural emergence of a reciprocal square root grain size law for the fracture strength.

The crack extension characteristics were illustrated by selecting a particular functional relation for the local toughness (fig. 1)

$$K^c_{eff} = K^c_s\,[1 + \kappa\chi/(1+\chi)] \qquad (1)$$

where $\kappa = K^c_p/K^c_s - 1$, $\chi = a/d\omega$, d is the grain size and ω is a dimensionless constant. This relation permitted a maximum in the stress to be established (fig. 2) at the relative crack length χ_c given by;

$$\chi_c = \frac{\chi-2+\kappa\sqrt{1-8/\kappa}}{2(\kappa+1)} \qquad (2)$$

This stress maximum provided the final relation for the failure strength[+];

$$\sigma_f = \sqrt{\pi}\,K^c_p/4\sqrt{d\omega} \qquad (3)$$

However, this choice for the toughness function only allowed a maximum stress to exist for $\kappa>8$.

[+] There is a typographical error in ref. 1 which has led to the omission of ω in eqns. (14) and (15).

The intent of the present note is to demonstrate that the absence of a stress maximum (and hence, of stable crack extension) for $\kappa<8$ is merely a consequence of the particular analytic function (eqn. 1) chosen to represent K^c_{eff}. Other choices yield stable crack extension for much smaller values of κ, in accord with the expectations of recent experimental observations.[3,4]

A particular limitation of the toughness function selected by Evans occurs at small crack lengths. Although the function reduces to K^c_s as $a \rightarrow 0$, it does not approach K^c_s asymptotically (only asymptotic behavior at large crack lengths was invoked in the choice of the function). Yet, a range of crack lengths, for which the crack extension resistance is given approximately by the single crystal value, $K^c_{eff} \approx K^c_s$, is expected for real systems. It can be readily demonstrated that the choice of a reasonable toughness function, that is also asymptotic at small crack lengths, provides the requisite stable crack extension for small values of K^c_p/K^c_s. A pertinent function has the form;

$$K^c_{eff} = K^c_s \left[1 + \kappa(1-e^{-\chi^2})\right] \qquad (4)$$

This function is compared with eqn. (1) in fig. 1. Differentiation yields the critical normalised crack length;

$$[(\kappa+1)/\kappa]\, e^{\chi_c^2} - 1 = 4\chi_c^2 \qquad (5)$$

Inspection of eqn. (5) indicates that χ_c exists for all positive values of κ. A regime of stable crack extension will thus occur for any value of K^c_p/K^c_s, as illustrated in fig. 2. It is noted that a stable growth region is encouraged by an extended range of uniform crack extension resistance, $K^c_{eff} \approx K^c_s$. The crack extension stress diminishes continuously within the single crystal range and hence, permits the stress to increase when the crack encounters a regime of increasing crack growth resistance.

However, it is emphasized that a region of increasing crack extension stress does not ensure that stable crack extension will be observed. It is also required that the initial crack length be large enough to allow the initial extension stress to be less than the stress maximum, as discussed in ref. 1. An extensive single crystal region of crack growth resistance is thus conducive to a crack length independent fracture stress only if the pre-existent crack is substantially extended into the single crystal region.

The potential for stable crack growth has thus been demonstrated for any system. Its existence in a particular system will depend upon the functional form of the local toughness and the initial crack length. A complete description of strength behaviors thus requires an experimental determination of the local toughness. One of us (A. V. Virkar) is currently engaged in the study of toughness on the local level.

ACKNOWLEDGEMENTS: The above work was supported by the National Science Foundation under Grant No. DMR-78-10016.and the Office of Naval Research under contract No. N0014-79-C-0159.

REFERENCES

1. A. G. Evans, "A Dimensional Analysis of the Grain Size Dependence of Strength," J. Am. Ceram. Soc., 63. [1-2], 115-116 (1980).
2. J. P. Singh, A. V. Virkar, D. K. Shetty and R. S. Gordon, "Strength-Grain Size Relations in Polycrystalline Ceramics," J. Am. Ceram. Soc. 62, [3-4], 179-183 (1979).
3. Anil V. Virkar, "Electrical-Mechanical Analog Applied to Crack Growth Studies in Glass-Glass Ceramic Composites," J. Am. Ceram. Soc., 63 [3-4], 219-223 (1980).
4. Anil V. Virkar, "Simulated Strength - Grain Size Study Using Glass-Glass Ceramic Composite System," submitted to Journal of Materials Science, (1979).

CHAPTER II

MARTENSITIC TRANSFORMATIONS IN ZIRCONIA: PARTICLE SIZE EFFECTS AND TOUGHENING

by

A. G. Evans, N. Burlingame, M. Drory and W. M, Kriven

Department of Materials Science and Mineral Engineering,
University of California,
Berkeley, CA 94720

MARTENSITIC TRANSFORMATIONS IN ZIRCONIA:
PARTICLE SIZE EFFECTS AND TOUGHENING

by

A. G. Evans, N. Burlingame, M. Drory and W. M. Kriven
Materials Science and Mineral Engineering
University of California
Berkeley, CA 94720

Abstract

The incidence of martensitic transformations in systems containing ZrO_2 particles (or precipitates) depends upon the size of the particles. The origin of this size effect is demonstrated to reside in the twinned or variant structure of the transformed phase, by virtue of a surface area related strain energy term. Predicted critical particle sizes correlate quite well with observations on two ZrO_2 systems. The particle size effect can also be incorporated into toughening analyses, in order to predict both optimum toughening conditions and toughening trends. The predictions again correlate favorably with toughness data for ZrO_2 containing materials.

I. INTRODUCTION

Martensitic transformations (involving a tetragonal to monoclinic crystal structure change) have been observed in zirconia precipitates[1,2,3] or particles[4,5]. The incidence of this transformation depends upon the size of the particle[1,2,3]: a phenomena that has not yet been adequately explained[†]. The initial intent of the present paper is to identify the origin of the size effect and to provide a basis for the quantitative prediction of the critical transformation condition. These results contain implications for the increase in fracture toughness that can be achieved in the presence of a size distribution of predominantly tetragonal ZrO_2 particles[5,7]. The interpretation of toughening effects in systems containing zirconia particles thus constitutes a second theme of the paper.

Martensitic transformations in zirconia can occur in accord with either of the two lattice invariant deformation processes, twinning or slip[8,9]. A relatively large shear is expected to accompany transformation for most permissable lattice invariant processes (viz. a shear strain along the habit plane of $\sim$14%). This large shear strain results in the formation of a series of variants (Fig. 1); especially when the transformation occurs within particles embedded in a matrix (such that the macroscopic shape deformation is subject to constraint). Transformed particles thus contain a series of sheared plates in which alternate plates have experienced shear deformations of opposite sign (Fig. 1). A significant macroscopic shear is not expected, therefore, whenever there are either a large number of variants or, in general, for an even number of variants.

[†] A size effect has been anticipated for situations in which the transformation yields microcracks[6] (notably, single phase polycrystalline ZrO_2). However, the transformation of isolated ZrO_2 particles is not usually accompanied by microcracking[1,3]. An alternate explanation must be sought for these systems.

The strain energy change that accompanies the martensitic transformation should be strongly influenced by the variant or twin structure of the martensite. Evidently, for a particle of specified size, the higher the variant (twin) density, the lower is the strain energy, and the larger the interface energy (associated with the parent/product, or twin, interface). The energy changes attributed to the twinned structure of the martensite are considered to be the source of the transformation size effect.

An analysis of the strain energy of spherical twinned particles has been presented by Kato et al[10], illustrating the diminution in strain energy that accompanies an increase in twin density. This solution is an essential source of the quantitative trends in strain energy pertinent to the analysis of size effects. This solution is augmented in the present paper by a two dimensional analysis of the stress and strain energy distributions in twinned (or variant) martensites, which provides the additional information (regarding strain energy localization) needed to address issues related to size effects. Both analyses pertain only to systems with homogeneous elastic constants; the critical size predictions are thus restricted to such systems (a close approximation is a system of ZrO_2 precipitates in a cubic ZrO_2 matrix). However, approximations pertinent to the analysis of transformations in the presence of elastic inhomogeneity are suggested. The critical transformation sizes predicted by the analysis are compared with results for ZrO_2[1,3] and for Al_2O_3/ZrO_2 alloys[11].

The size effect also has a significant influence on the toughening that can be experienced in the presence of an array of tetragonal ZrO_2

particles. A previous toughening analysis[12, 13] is extended to include a size distribution of particles: to yield predictions of the optimum toughening and of toughening trends. The predictions are compared with experimental results[1,7].

2. STRESS AND STRAIN ENERGIES ASSOCIATED WITH TWINNED PARTICLES

The stress distributions that develop in martensite plates containing twins or variants can be determined straightforwardly (in the absence of elastic modulus inhomogeneity) by adopting an Eshelby approach[14] (Fig. 2). The stresses within the twinned plates are determined from the sum of the uniform shear stresses needed to restore the unconstrained twins to their original shape (Fig. 2) and the non-uniform stresses that arise from applying the body forces, at the twin boundaries and parent/product interfaces, needed to establish continuity of stress[6,15] (Fig. 2). The stresses within the parent phased derive exclusively from the body forces. The spatially dominant stresses induced by twinning are the shears τ_{xy}.[†] The shear stresses at a location (y,z) with respect to the twin interface (Fig. 2c), that derive from a line body force of magnitude P, at a distance x from the interface (Fig. 2), are given by[17];

$$\tau_{xy} = \frac{P}{4\pi} \frac{y}{[(x+z)^2+y^2]} \left[(1-\nu) + 2(1+\nu) \frac{(x+z)^2}{[(x+z)^2+y^2]} \right] \qquad (1)$$

[†] Normal stresses σ_{xx} and σ_{yy} also develop. These are singular at the twin/habit intersection, but decay very rapidly with distance (a logarithmic singularity)[16]. The normal stresses are essential to considerations of microcracking[16], but constitute a secondary contribution to the strain energy. The normal stresses are thus neglected for present purposes.

where ν is the Poisson ratio. The body forces needed to establish stress continuity are given by;

$$P = -(\mu\gamma_T/2)dx \tag{2}$$

where μ is the shear modulus and γ_T is the unconstrained shear strain associated with each twin (Fig. 2a). The stresses around a centrally located twin can be deduced by integrating the body forces over all twin and parent/product interfaces. The stresses within the parent phase for a particle with length L, width ℓ and twin spacing d are given, for ν=0.2, by;

$$\frac{\tau_{xy}}{\mu\gamma_T} = \frac{1}{4\pi}\sum_{\eta=1}^{\eta=L/4d}\left\{\int_{2\eta-1+y/d}^{2\eta+y/d}(\phi_1-\phi_2)d\beta + \int_{2\eta-2-y/d}^{2\eta-1-y/d}(\phi_1-\phi_2)d\beta \right.$$

$$\left. - \int_{2\eta-2+y/d}^{2\eta-1+y/d}(\phi_1-\phi_2)d\beta - \int_{2\eta-1-y/d}^{2\eta-y/d}(\phi_1-\phi_2)d\beta + 2\int_{z/d}^{z/d+\ell/d}(\zeta_1+\zeta_2-\zeta_3-\zeta_4)d\beta\right\} \tag{3}$$

where,

$$\phi_1 = \frac{(z/d)[0.8(z/d)^2+3.2\beta^2]}{[(z/d)^2+\beta^2]^2}\ , \quad \phi_2 = \frac{(z/d-\ell/d)[0.8(z/d-\ell/d)^2+3.2\beta^2]}{[z/d-\ell/d)^2+\beta^2]^2.}\ ,$$

the ζ terms are given by:

$$\zeta = \frac{\gamma[0.8\gamma^2+3.2\beta^2]}{[\beta^2+\gamma^2]^2}$$

such that γ is $(2\eta-1-w)$ for ζ_1, $(2\eta-2-w)$ for ζ_2, $(2\eta-1+w)$ for ζ_3 and $(2\eta-w)$ for ζ_4, and $\beta = x/d$.

The stresses within the twinned particles are deduced from Eqn. (3) by inserting the appropriate negative values for z/d, and superimposing a uniform shear stress (of unit normalized magnitude).

The resultant stresses are plotted in Fig. 3 at several locations, y/d. The same results pertain for all values of particle length, $L \gtrsim 10d$, and for all particle widths, $\ell \gtrsim 3d$. Two important characteristics are noted. Firstly, the zone of significant stress is confined to a region close to the plane of termination of the twins, i.e., the parent/product interface. This behavior arises because the alternating shears associated with adjacent twins tend to eliminate long range stresses (a result that should be expected from St. Venant's principle). Secondly, the stresses are a unique function of the normalized distance from the interface, z/d; independent of the absolute twin spacing, the twin dimension, and the particle dimension, (at least for $\ell/d \gtrsim 3$). This localization of the stresses and the scaling with d had previously been anticipated by Roitburd and Khachaturyan[18]. The stresses deduced from Fig. 3 can be approximately expressed (for $0.5 \;\; y/d \gtrsim 0.1$) by the analytic function;

$$\frac{\tau}{\mu \gamma_T} = F(z/d) \approx 1.5(z/d)^{0.7} e^{-2(z/d)^{1.7}} \tag{4}$$

For, $0.1 > y/d < 0$, the stresses decrease, monotonically, approaching zero at $y/d = 0$. A different result will, of course, pertain for twins adjacent to the extremities of the particle.

Since the stresses are confined to a zone close to the particle interface, it might be anticipated that the component of the strain energy associated with the twinning be more closely related to the surface area of the particle than its volume (note that the strain energy derived from the macroscopic shape change is solely dependent on the particle volume V), especially for large numbers of twins. A rough estimate of this strain energy term for a spherical particle of radius a is obtained by considering that the shear stresses in each twin are given by Eqn. (4). This estimate of the strain energy change is;

$$\Delta\phi^{m}_{T} \approx \frac{\mu(\gamma_T)^2}{2} (4\pi a^2)d \int_{-\ell/2d}^{\infty} F^2(z/d)d(z/d) \qquad (5)$$

$$\equiv \alpha\mu(\gamma_T)^2 \cdot a^2 d$$

Inserting the approximate F(z/d) suggested by Eqn. (4), the strain energy becomes,

$$\frac{\Delta\phi^{m}_{T}}{\mu V(\gamma_T)^2} = 0.2 \left(\frac{d}{a}\right) \equiv \frac{0.4}{n} \qquad (6)$$

where n is the number of twins in the particle ($n = 2a/d$). This is necessarily a lower bound result because the contribution from the normal stresses has been neglected. Recognition of the special significance of the surface area provides a useful perspective for interpreting and extending the numerical solution of Kato et al[10]. For a large number of twins it might be anticipated that the normalized energy, $\Delta\phi^{m}_{T}/\mu(\gamma_T)^2$, becomes inversely proportional to the number of twins, as exemplified by Eqn. (6). However, in order to permit the existence of more complex behavior at limited twin densities, a more general relation for the strain energy can be obtained by adopting the function;

$$\frac{\Delta\phi_T^m}{\mu(\gamma_T)^2 V} = \frac{\lambda_1}{\lambda_2+\eta} \tag{7}$$

where λ_1 and λ_2 are constants. A comparison of Eqn. (7) with the calculations of Kato et al[10] (Fig. 4) indicates a good correlation, with $\lambda_1 \sim 0.64$ and $\lambda_2 \sim 2.4$. The result for large η

$$\frac{\Delta\phi_T^m}{\mu(\gamma_T)^2} = \frac{0.64}{\eta} \tag{8}$$

is in modest agreement with the estimate obtained above, by focussing on the stresses in the vicinity of the particle interface.

3. TRANSFORMATION THERMODYNAMICS

The changes in thermodynamic potential that accompany the formation of a twinned martensite are the mechanical potential, $\Delta\phi^m$ (strain energy and interaction energy), the surface work, $\Delta\phi_s$, and the chemical potential, ΔF_c. The latter is independent of the extent of twinning, and for spherical particles of radius, a, the chemical free energy change per particle is simply;

$$\Delta F_c = -(4/3)\pi a^3 \Delta F_0 \tag{9}$$

where ΔF_0 is the Helmholtz free energy difference between unit volume of the two phases. The surface work reflects changes that occur at the martensite interface as well as the formation of twin (variant) boundaries. If the twin spacing is d, the total surface energy change $\Delta\phi_s$ for a spherical particle is;

$$\Delta\phi_s = 4\pi a^2 \Gamma_i + 2\pi a^2 \frac{(\eta-1)(\eta+1)}{3\eta} \Gamma_t \tag{10}$$

where Γ_i is the interface energy and Γ_t is the twin boundary energy. Evidently, for a large number of twins, d<<a, Eqn. (10) reduces to;

$$\Delta\phi_s \approx \frac{4\pi a^3}{3d}\Gamma_t \qquad (11)$$

The mechanical energy change can be considered to consist of two components: that due to the macroscopic shape change $\Delta\phi^m_m$ and that associated with the twinning $\Delta\phi_T$. The macroscopic component under conditions of constant applied stress $\acute{p}^A_{ij}$ includes a strain energy and an interaction energy (with the applied stress) and is given by[13];

$$\Delta\phi^m_m = \frac{4}{3}\pi a^3\left\{\Delta V\left[0.14E\Delta V-p^A\right]+\left[0.21E\acute{e}^T_{ij}\acute{e}^T_{ij}-\acute{p}^A_{ij}\acute{e}^T_{ij}\right]\right\} \qquad (12)$$

where ΔV is the volume strain, e^T_{ij} is the deviatoric component of the average particle transformation strain and p^A and $\acute{p}^A_{ij}$ are, respectively, the dilational and deviatoric components of the applied stress. The twin component is obtained directly from Eqn. (7) as;

$$\Delta\phi^m_T = (4/3)\pi a^3 E\gamma_T^2[0.13/(1.2+a/d)] \qquad (13)$$

This component does not involve a significant interaction energy with the applied stress, because of the alternating character of the twinning shear strains. It is not generally permissable, of course, to sum strain energy terms, unless they derive from different constituents of the applied stress. Hence, the twin component (which emanates from the shear stresses) can be combined directly with the dilational constituent of the macroscopic potential.

but should not be combined with the deviatoric constituent. However, as noted above, typical variant structures of transformed ZrO_2 particles indicate a small macroscopic shear deformation. It would thus appear permissable to neglect the deviatoric part of the macroscopic strain energy, for present purposes, thereby averting this difficulty. Additionally, it is noted that the spatial locations of the stresses created by twinning (localized near the interface) are quite differenct from those associated with the macroscopic shape change (uniformly distributed throughout the particle). Any error incurred if a simple summation of the mechanical energies were invoked should thus be quite small.

The total potential change associated with transformation can now be expressed as;

$$\frac{\Delta\Phi}{(4/3)\pi a^3} = -\Delta F_o + \Gamma_t/d + 3\Gamma_i/a + 0.14E\,\Delta V^2 - p^A\Delta V + 0.13E\gamma_T^2/(1.2+a/d) \qquad (14)$$

This basic result can be used to examine the existence of a driving force for the transformation and thereby, to estimate size effects, toughening, etc. The four variables that influence transformation in a given material are the chemical free energy ΔF_o (which is dependent on temperature and solute content), the particle size, the twin spacing and the applied stress. The only variable that is not readily specified a priori is the twin spacing. The twin structure presumably evolves in the nucleative stage of the transformation and hence, a minimization of $\Delta\Phi$ with respect to d (at constant a and p^A) does not necessarily provide a useful prediction of the expected twin spacing. Such an analysis ($\partial\Delta\Phi/\partial d=0$) would suggest that

$$d = \frac{1.9(\Gamma_t a)^{1/2}}{\gamma_T E^{1/2}[1-4.6\Gamma_t^{1/2}/\gamma_T(Ea)^{1/2}]} \tag{15a}$$

or, for $a \gg d$,

$$d = \frac{1.9(\Gamma_t a)^{1/2}}{\gamma_T E^{1/2}} \tag{15b}$$

Experimental results obtained by Kato et al[10] for iron particles in a Cu-Fe alloy are not consistent with this prediction; rather, d would appear to be approximately independent of the particle size. This experimental result is preferred for all subsequent developments in this paper because preliminary observations suggest a similar behaviour for ZrO_2[11,19]. Refinements that include a size dependence of d could be incorporated later, if it is substantiated that a significant size effect exists in the systems of interest.[†] However, it is noted here that the twin spacing should be independent of the chemical free energy change.

[†] A two-dimensional nucleation analysis involving a simple twin or variant has been reported by Roitburd and Kurdjumov[20]. At the critical nucleation condition a twin spacing/length relation identical to Eqn. (15), except for the numerical coefficient, was derived. Then, by assuming that the twin (variant) extended fully across the particle before broadening to the final dimension, a twin spacing proportional to the twin length was predicted. This prediction is even less consistent with the experimental results. Further studies of this phenomenon are clearly demanded.

4. PARTICLE SIZE EFFECTS

Particle size effects on transformation emerge by considering the condition wherein the total free energy change becomes incrementally negative. This condition will yield a minimum possible value for the critical particle size, a^c_{min}, at which transformation will initiate. This estimate of the critical size is most pertinent when the nucleation barrier is relatively small, i.e. the free energy at successive stages of partial transformation is only marginally in excess of the free energy of the fully transformed particle. Justification for the neglect of an appreciable nucleation barrier can only be effectively established (for a specific system) by a comprehensive comparison of the predicted and observed critical transformation dimension and its dependence on composition, temperature and elastic stiffness[†]. (It is noted that this comparison is most readily achieved with ceramic systems, because they exhibit negligible relaxation of the elastic strains by dislocation activity near the particle). Some favorable preliminary comparisons for ZrO_2 will be presented in this section.

Setting the total thermodynamic potential $\Delta\phi$ in Eqn. (14) to zero, the following relation for the lower bound critical size obtains;

$$\frac{3\Gamma_i}{a^c_{min}} + \frac{\Gamma_t}{d} + \frac{0.13E\gamma^2_T d}{1.2d+a^c_{min}} = \Delta F_o + P^A\Delta V - 0.14E\Delta V^2 \qquad (16)$$

If the twin spacing is considered to be insensitive to particle size[††], as the limited experimental observations suggest, then the critical particle size becomes;

[†] Critical transformation dimensions considerably in excess of the values based on the free energy of the fully transformed particle would suggest a size effect based on statistical arguments, through a spatial distribution of nucleation sites.

[††] It is noted that the present analysis would yield a size effect (attributable to strain energy localisation due to variant formation) provided that $d \propto a^n$ with $n<1$. It is not imperative that d be independent of a.

$$\frac{a^c_{min}}{d} = \frac{3\Gamma_i + 0.13E\gamma_T{}^2 d}{\Gamma_t + d(\Delta F_o + p^A\Delta V - 0.14E\Delta V^2)} - 1.2 \qquad (17)$$

When the interface energies are relatively small $(\Gamma_i/E\gamma_T{}^2 d<10^{-2}, \Gamma_t/d\Delta F_o<10^{-1})$, the relation for the critical size reduces to;

$$\frac{a^c_{min}}{d} \equiv \frac{\eta_c}{2} = \frac{0.13E\gamma_T{}^2}{\Delta F_o + p^A\Delta V - 0.14E\Delta V^2} - 1.2 \qquad (18)$$

which, in the absence of an applied stress, becomes:

$$\eta_c = \frac{0.27(\gamma_T/\Delta V)^2}{\Delta F_o/E\Delta V^2 - 0.14} - 2.4 \qquad (19)$$

A specific number of twins (or variants) is thus predicted at the critical condition.[+]

The preceding analysis pertains to systems with homogeneous elastic and thermal expansion properties. Modifications that incorporate elastic inhomogeneity and thermal expansion mismatch effects are of considerable importance. The effect of modulus inhomogeneity is difficult to anticipate because only the component of the strain energy associated with the macroscopic shape change can be readily analyzed. However, since the stresses associated with

---

[+] Since it is not yet known whether the variant spacing can be changed for a given material, it should not be assumed that a critical number of variants could be achieved for a variety of actual particle radii.

the twinning component of the strain energy are confined to the immediate vicinity of the particle interface, an average value of the modulus of the matrix and particle <E> may be used to afford an approximate measure of the strain energy change, viz;

$$\Delta\phi_T^m \simeq (4/3)\,\pi a^3 \langle E\rangle \gamma_T^2\,[0.13/(1.2 + a/d)] \tag{20}$$

The mechanical energy change associated with the particle dilation, for $\nu = 0.2$, is[13]

$$\Delta U_m = (4/3)\pi a^3 \left[\frac{E_p \beta \Delta V^2}{3.6(1+\beta)} - p^A \Delta V\right] \tag{21}$$

where β is the ratio of the elastic modulus of the matrix E_m to that of the particle, E_p. Modifying the preceding analysis in accord with these energy terms yields a new value for the variant density at the critical size;

$$n_c = \frac{6\Gamma_i + 0.13E_p(1+\beta)\gamma_T{}^2 d}{\Gamma_t + d[\Delta F_o - 0.28E_p\beta\Delta V^2/(1+\beta)]} - 2.4 \tag{22}$$

or, for relatively small interface energies;

$$n_c \approx \frac{0.13E_p(1+\beta)\gamma_T{}^2}{\Delta F_o - 0.28E_p\beta\Delta V^2/(1+\beta)} - 2.4 \tag{23}$$

The above predictions can be compared with experimental results obtained for partially stabilized ZrO_2[1,3], and for Al_2O_3/ZrO_2[11]. Transformation in partially stabilized ZrO_2 results in the formation of variants with about four variants within each particle.[1,3] The pertinent transformation parameters are [12]: $\Delta F_o \sim 230MPa$ (for transformation close to room temperature in partially stabilized ZrO_2, which is the critical condition of present interest), $E \sim 170GPa$, $\Delta V \sim 0.058$. The shear in the habit plane γ_T is ~ 0.14[8,9] and (for an even number of variants) there is no macroscopic shear deformation of the particle. The measured variant spacing[3] is $\sim 2 \times 10^{-7}m$. Hence, for typical upper bound values of the interface energies, $\Gamma_t \sim \Gamma_i \sim 1Jm^{-2}$, the magnitudes of the quantities, $\Gamma_i/E\gamma_T^2 d$ and $\Gamma_t/d\Delta F_o$ are $\sim 2 \times 10^{-3}$ and $\sim 2 \times 10^{-2}$ respectively. The interface energy terms in Eqn. (17) are thus of negligible magnitude. Noting that $\Delta F_o/E\Delta V^2$ is ~ 0.4, substitution of the remaining transformation parameters into Eqn. (17) indicates that the critical number of variants for transformation in the absence of an external stress is ~ 4. The prediction is thus consistent with the observed variant structure of transformed particles[1,3]. It is also noted that an applied stress will only significantly reduce the critical variant density (i.e., to ~ 2) if the hydrostatic component is in excess of $\sim 3GPa$. Such large stresses can only be encountered in the vicinity of a crack tip[21].

For the Al_2O_3/ZrO_2 system, the modulus ratio β is ~ 2.5 and hence, the number of variants at the critical size, derived from Eqn. (23), is

$$n_c = \frac{0.25E_p\gamma_T^2}{\Delta F_o - 0.2E_p\Delta V^2} - 2.4 \qquad (24)$$

The effective volume strain in the ZrO_2/Al_2O_3 system is smaller than in a ZrO_2 material because of the thermal expansion mismatch, $\Delta\alpha$, such that

$$\Delta V_{eff} = \Delta V - 3\Delta\alpha\Delta T \tag{25}$$

where ΔT is the cooling range. The incorporation of the effective volume change is equivalent to recognizing that the system is subject to a strain energy prior to transformation that derives from the expansion mismatch and hence, that the change in strain energy upon transformation is reduced (when $\Delta\alpha$ is positive). Inserting the effective volume change and the other transformation parameters into Eqn. (24), the number of variants at the critical size is ~6. Observations (Fig. 5) indicate 6-10 variants in critical-sized particles.

Particle size effects predicted by the thermodynamic requirements for complete transformation are thus consistent with observations of martensitic transformations in two ZrO_2 systems. A basis for further study, emphasizing effects of temperature and solute content on the transformation, is thus established. Also, a more comprehensive analysis of toughening than has previously been possible can now be attempted, as discussed in the following section.

5. TRANSFORMATION TOUGHENING

5.1 Analysis

The hydrostatic component of the stress needed to induce transformation (neglecting interface energy terms) is obtained from Eqn. (14) as;

$$p^A\Delta V = 0.14E\Delta V^2-\Delta F_0 + \frac{0.27E\gamma_T^2}{2.4+n} \qquad (26)$$

Noting that the hydrostatic stress near a crack tip is[22];

$$p^A = \frac{2K(1+\nu)}{3\sqrt{2\pi r}}\cos(\theta/2) \qquad (27)$$

where K is the stress intensity factor and (r,θ) are the coordinates with respect to the crack tip, the distance r_c from the crack tip at which a single particle will transform can be deduced, for $\nu = 0.2$, as;

$$2\pi r_c = 8.8\left\{\frac{K\Delta V}{E\gamma_T^2}\,\frac{(2.4+n)(2.4+n_c)}{(n_c-n)}\cos(\theta/2)\right\}^2 \qquad (28)$$

This prediction makes the implicit assumption that each particle experiences a sufficient shear stress that the transformation may nucleate when the thermodynamic conditions are satisfied. This assumption requires further investigation.

The toughening Γ_T associated with the transforming particles may now be determined, using[13];

$$\Gamma_T = 2\Delta\phi^* r_T V_f/(4/3)\pi a^3+\Gamma_0 \qquad (29)$$

where V_f is the volume fraction of particles, Γ_0 is the intrinsic toughness of the matrix, $\Delta\phi^*$ is the free energy change in the absence of an applied stress and r_T is the transformation zone width, given by[13],

$$r_T = \omega(V_f)\hat{r}_c \qquad (30)$$

where $\hat{r}_c$ is the zone dimension that coincides with the maximum zone width $(\theta \sim \pi/3)$[23]. The quantity ω is a proportionality constant that allows for the relaxation of the stress field by the prior transformation of particles closer to the crack tip and for a partial reverse transformation of particles near the periphery of the transformation zone. A much more extensive analysis than that conducted herein would be needed to evaluate ω. However, for present purposes, ω is estimated by comparing predicted with observed transformation zone dimensions[21]. The transformation zone size for a partially stabilized ZrO_2 with two complete transformation variants within each particle and a fracture toughness[3] of 4.9MPa$\sqrt{m}$ is predicted from Eqn. (28) to be 1.5μm. This compares with a measured zone size of ∿0.6 μm[21]: suggesting that the relaxation parameter ω is ∿0.4. This magnitude is assumed herein to pertain for all conditions. However, it is recognized that there could be a significant influence of the particle volume fraction on ω: an effect that is not included in the present analysis. Substituting r_T from Eqns. (28) and (30) (the maximum zone width) into Eqn. (29), the toughening becomes

$$\Gamma_T = \frac{6.6}{\pi} \frac{K^2(\Delta V/\gamma_T)^2}{E} V_f \left[\frac{(2.4+\eta)(2.4+\eta_c)}{(\eta_c-\eta)}\right] \langle\omega\rangle + \Gamma_0 \qquad (31)$$

Inserting the requirement that K at the criticality is, $\sqrt{E\Gamma_T}$, we obtain;

$$\frac{\Gamma_T}{\Gamma_0} = \frac{1}{1-\zeta} \qquad (32)$$

where

$$\zeta = 2V_f(\Delta V/\gamma_T)^2 \frac{(2.4+\eta)(2.4+\eta_c)}{(\eta_c-\eta)} \langle\omega\rangle$$

As noted in the previous section, $\Delta V/\gamma_T$ is 0.41. The toughening expected for ZrO_2 is thus expressed (with $\omega \sim 0.4$) by,

$$\zeta \approx 0.12\ V_f \frac{(2.4+\eta)\ (2.4+\eta_c)}{(\eta_c-\eta)}$$

For the Al_2O_3/ZrO_2 system, the modulus mismatch ($\beta=2.5$) causes ζ to increase, by a factor of $\sim$1.2.

The toughening anticipated by Eqn. (32) pertains when the particle sizes are uniform. Significant deviations can be expected when a size distribution of particles exists. If the particle size distribution is characterized by the frequency function, $\phi(a)da$, then the toughening given by Eqn. (30) becomes;

$$\Gamma_T = \frac{2K^2(\Delta V/\gamma_T)^2}{E} V_f \frac{(2.4+\eta_c)}{\langle a^3\rangle} \langle\omega\rangle \int_0^{a_c} \frac{a^3(2.4d+a)}{(a_c-a)} \phi(a)da + \Gamma_o \qquad (33)$$

Assuming an extreme value distribution for $\phi(a)da$ (since the larger particles are of principal interest[23]),

$$\phi(a)da = k \frac{a_o^k}{a^{k+1}} \exp\left[-\left(\frac{a_o}{a}\right)^k\right] da \qquad (34)$$

where a_o is the scale parameter and k is the shape parameter, the toughening becomes;

$$\Gamma_T = 2K^2 \frac{(\Delta V/\gamma_T)^2 V_f(2.4+n_c)}{E} \langle\omega\rangle \; I(a_o/a_c\; k) + \Gamma_o \qquad (35)$$

where $I(a_c/a_o,k)$ is a function obtained by integration. Similarly, the relative toughening is expressed through the parameter.

$$\zeta = 2\langle\omega\rangle(\Delta V/\gamma_T)^2 \; V_f(2.4+n_c) \; I(a_o/a_c,k) \qquad (36)$$

Inserting the known values for the transformation strains and the critical variant density for ZrO_2 particles in a ZrO_2 matrix into Eqn. (35), the predicted toughening is plotted as a function of particle size, in Fig. 6, for several values of the shape parameter k. It is observed that a peak toughening, $\hat{\Gamma}_T$, occurs for each k, coincident with a particular value of the ratio of the scale parameter of the distribution to the critical size $\hat{a}$.

5.2 Comparison With Experiment

The predictions of the above model can be compared with toughness data obtained for PSZ[1] and for Al_2O_3/ZrO_2[7]. For this purpose, the solutions pertinent to a size distribution of particles are used. Emphasis is placed on solutions in the range, $5 \leqslant k \leqslant 10$, as representative scale parameters for typical microstructural entities[24] (discreteness of the transformation that may occur in the presence of a small number of variants per particle is neglected). The comparisons with available data can only be superficial, because of the ancilliary information needed to insert into the models (particularly the particle sizes) is not available. More complete comparisons will be presented in a subsequent publication[5].

For the PS7 material of Porter and Heuer[1], the primary variable that influences the toughening is the particle size, which is consistenly varied by extending the annealing period. Changes in volume fraction are also occurring during the precipitation process, but these changes are assumed to be secondary, within the range of the optimum toughness. Particle coarsening following precipitation often occurs as a function of time, t, in accord with a $t^{1/3}$ dependence (the interface control result). If this behaviour is assumed to pertain in the Porter and Heuer experiments[1], a comparison between the toughening measurements and the predictions of the present model are shown in Fig. 7 for k = 6 (the Schoenlein result[3] is used for the optimum toughness, since this result excludes any contribution from surface compressive stresses). The relatively good correlation is encouraging.

The results of Lange[7] for the Al_2O_3/ZrO_2 system can also be examined in the context of the present model. The principal variable in Lange's experiments is the volume fraction. However, there may also be a systematic increase in particle size as the volume fraction is increased. If this latter effect is neglected, the experimental results can be compared with the model predictions for volume fractions, $V_f \lesssim 0.3$ (i.e., isolated ZrO_2 particles): another model would be required to establish the behaviour expected for a continuous ZrO_2 phase. Comparisons in this range, illustrated in Fig. 8, indicate that the observed trends are adequately predicted by the model. It is reemphasized, however that the comparison is superficial in the absence of size distribution information.

6. CONCLUSION

The energy changes that accompany the complete martensitic transformation of an isolated particle have been examined. It has been demonstrated that one of the dominant energy terms depends primarily upon the surface area of the particle, whereas the other principal terms depend upon the particle volume. A particle size dependence of the transformation thus naturally emerges from energy change considerations. The energy term that depends upon the particle surface area is the strain energy that derives from the twinned or variant structure of the martensite. The areal character of this dependence arises because the twinning stresses are localized near the particle interface.

Lower bound estimates of the critical particle size for stress free transformation have been obtained from the energy changes associated with complete transformation. The analysis predicts a specific number of twins or variants within particles at the critical size. Predictions performed for two modes of transformation in ZrO_2 particles provide a consistent description of the observed size effects.

The size effect has been incorporated into analyses of the toughening induced by crack tip transformations. The toughening that can be realized has been shown to depend on the particle size distribution, as well as the chemical free energy change and the pertinent transformation strains. The choice of a typical size distribution permits the observed toughening trends for partially stabilized ZrO_2 and for Al_2O_3/ ZrO_2 alloys to be correlated with the predictions of the model.

ACKNOWLEDGEMENTS

The authors express their appreciation for the financial support of this research provided by the Office of Naval Research (A.G.E.) under Contract No. N0014-79-C-0159.

REFERENCES

1. D. L. Porter and A. H. Heuer, Jour. Am. Ceram. Soc., 62, 298 (1979).
2. R. Hanninck, Jour. Mat. Sci., 13, 2487 (1978).
3. L. H. Schoenlein, M.S. Thesis, Case Western Reserve University (1979).
4. M. Ruhle and N. Claussen, to be published.
5. N. Burlingame, W. M. Kriven and A. G. Evans, to be published.
6. D. R. Clarke, Acta Metallurgica to be published.
7. F. F. Lange, Science Center Report SC 5117 7TR (October 1979).
8. G. Bansal and A. H. Heuer, Acta Metallurgica, 22, 490 (1974).
9. S. W. Kennedy, W. L. Fraser and W. M. Kriven, to be published.
10. M. Kato, R. Monzen and T. Mori, Acta Metallurgica, 26, 625 (1978).
11. W. M. Kriven, A. G. Evans and A. H. Heuer, to be published.
12. D. Porter, A. G. Evans and A. H. Heuer, Acta Metallurgica, 27, 1649 (1979).
13. A. G. Evans and A. H. Heuer, Jour. Amer. Ceram. Soc., (May/June 1980), in press.
14. J. D. Eshelby, Proc. Roy. Soc., A 252 561 (1959).
15. A. G. Evans, Acta Metallurgica, 26, 1845 (1978).
16. Y. Fu, W. M. Kriven and A. G. Evans, to be published.
17. S. Timoshenko and J. N. Goodier, Theory of Elasticity (McGraw Hill) 1951.
18. A. L. Roitburd and A. G. Khachaturyan, Problems in Physical Metallurgy and Metal Physics, 78 (1968).
19. M. Ruhle, private communication.
20. A. L. Roitburd and G. Kurdjumov, Mat. Sci. Eng., 39, 141 (1979).

21. D. L. Porter and A. H. Heuer, Jour. Amer. Ceram. Soc., 60, 183 (1977).

22. B. R. Lawn and T. R. Wilshaw, Fracture of Brittle Solids (Cambridge University Press) 1976.

23. A. G. Evans and K. T. Faber, Jour. Amer. Ceram. Soc., to be published.

24. A. G. Evans, B. R. Tittmann, L. Ahlberg, B. T. Khuri-Yakub and G. S. Kino, Jour. Appl. Phys., 49 2669 (1978).

FIGURE CAPTIONS

Fig. 1. A schematic indicating the constrained and unconstrained shapes of monoclinic ZrO_2 particles containing variants.

Fig. 2. A schematic indicating the Eshelby method of calculation applied to a twinned (or variant) martensite.

Fig. 3. The normalized shear stress plotted as a function of distance from the interface.

Fig. 4. A plot of the normalized strain energy as a function of the number of twins (Eqn. 7) compared with the discrete results of Kato et al[10].

Fig. 5. Transmission electron micrograph of transformed ZrO_2 particles in an Al_2O_3[11] matrix.

Fig. 6. The effects of a size distribution on the toughness of ZrO_2 predicted by the analysis.

Fig. 7. A comparison of the toughness data obtained by Porter and Heuer[1] and by Schoenlein[3] with the behavior predicted by the model.

Fig. 8. A comparison of the toughness data for Al_2O_3/ZrO_2 obtained by Lange[7], with the predictions of the model.

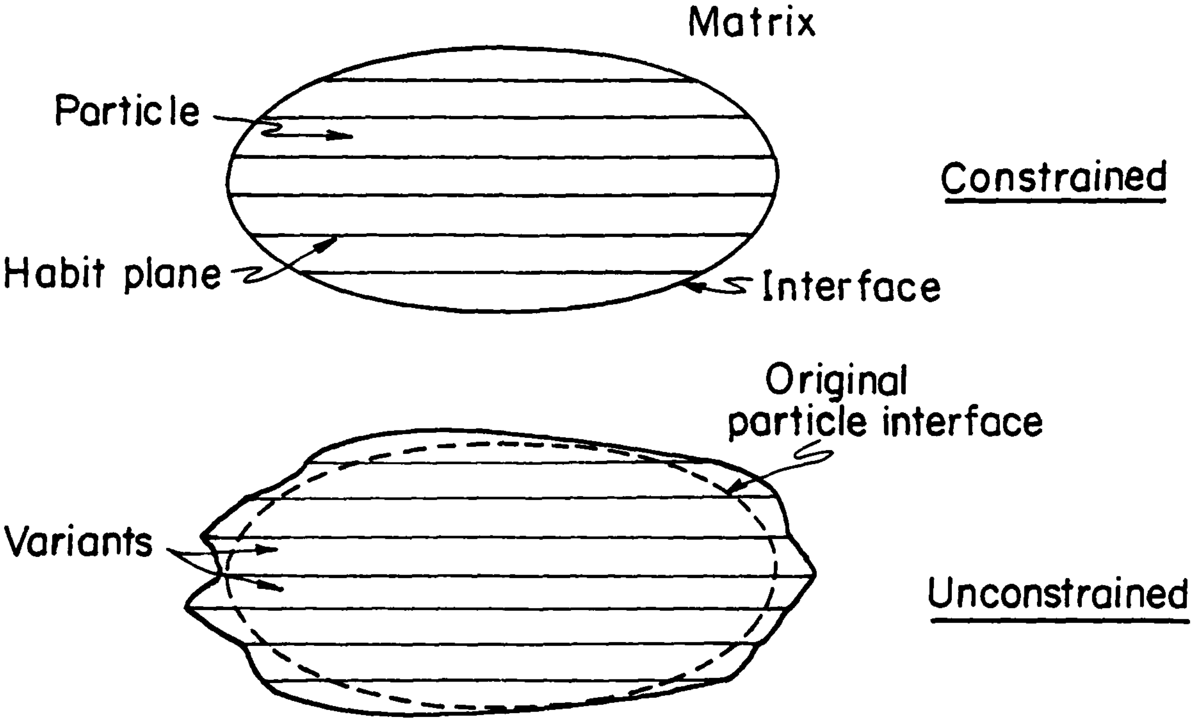
Matrix
Particle
Constrained
Habit plane
Interface
Original particle interface
Variants
Unconstrained

a) Slip mode transformation : particle contains variants

XBL 801-4537A

Fig. 1

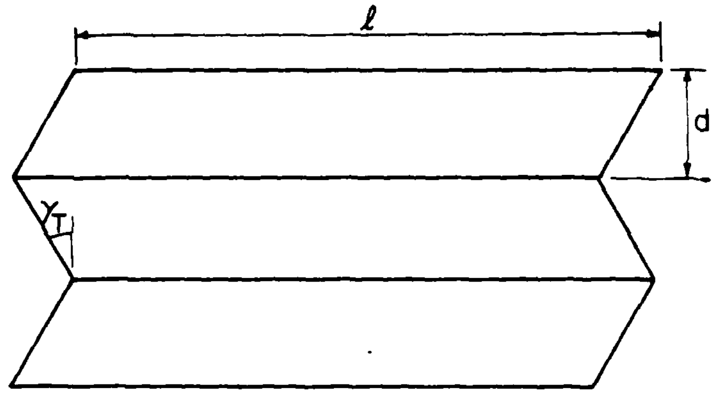

a) Unconstrained shape change

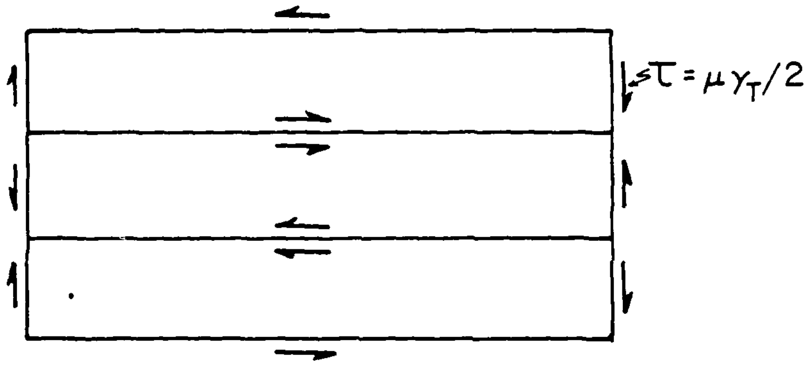

b) Restoration to original shape

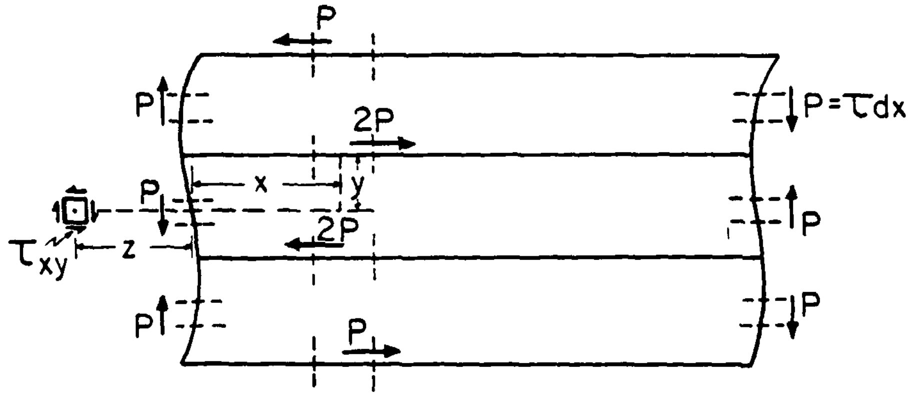
P
2P
P = τdx
x
y
z
τ_xy
P
2P
P
P
P
P
P

c) Relaxation

XBL 801-4536

Fig. 2

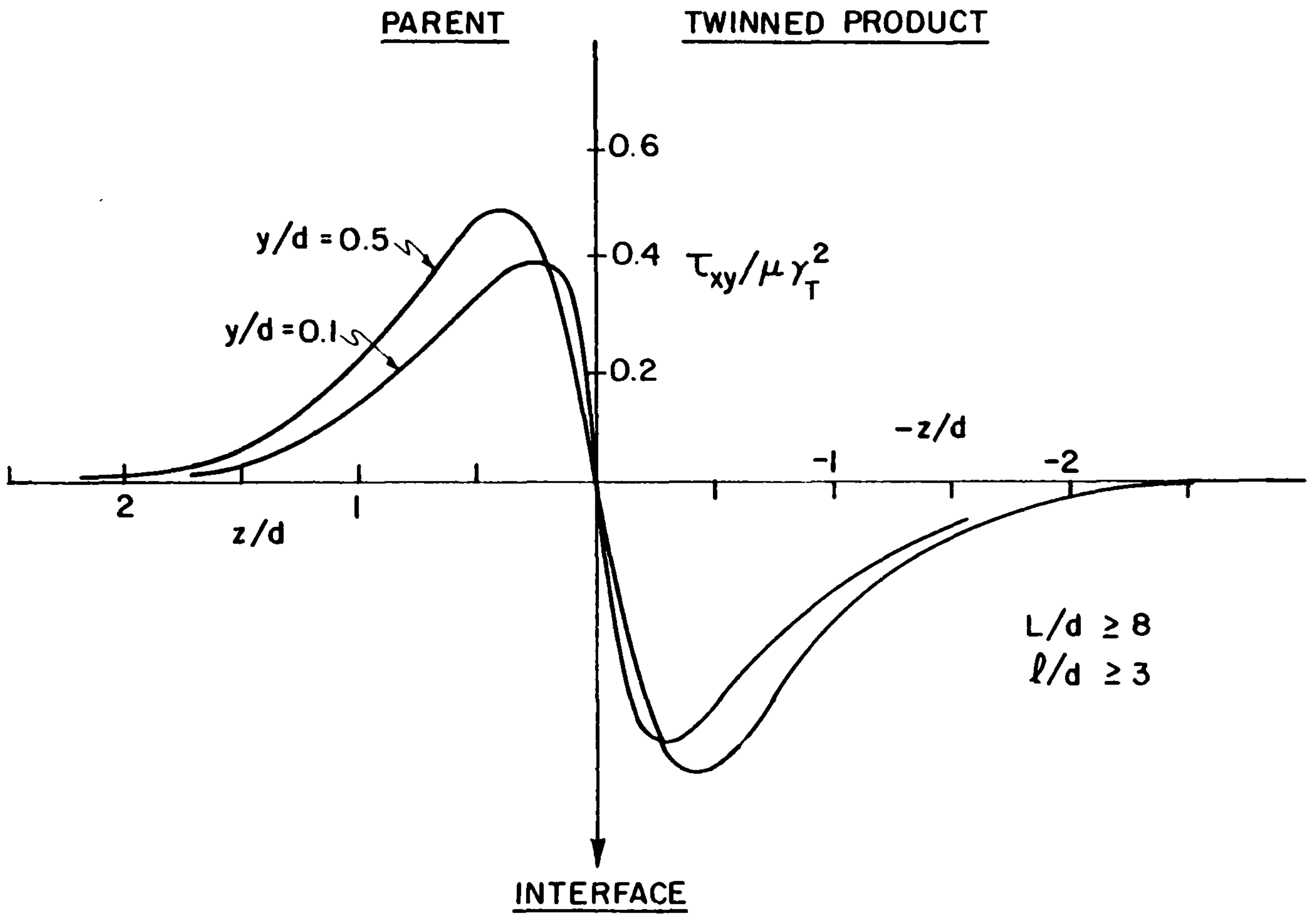

XBL 801-4538

Fig. 3

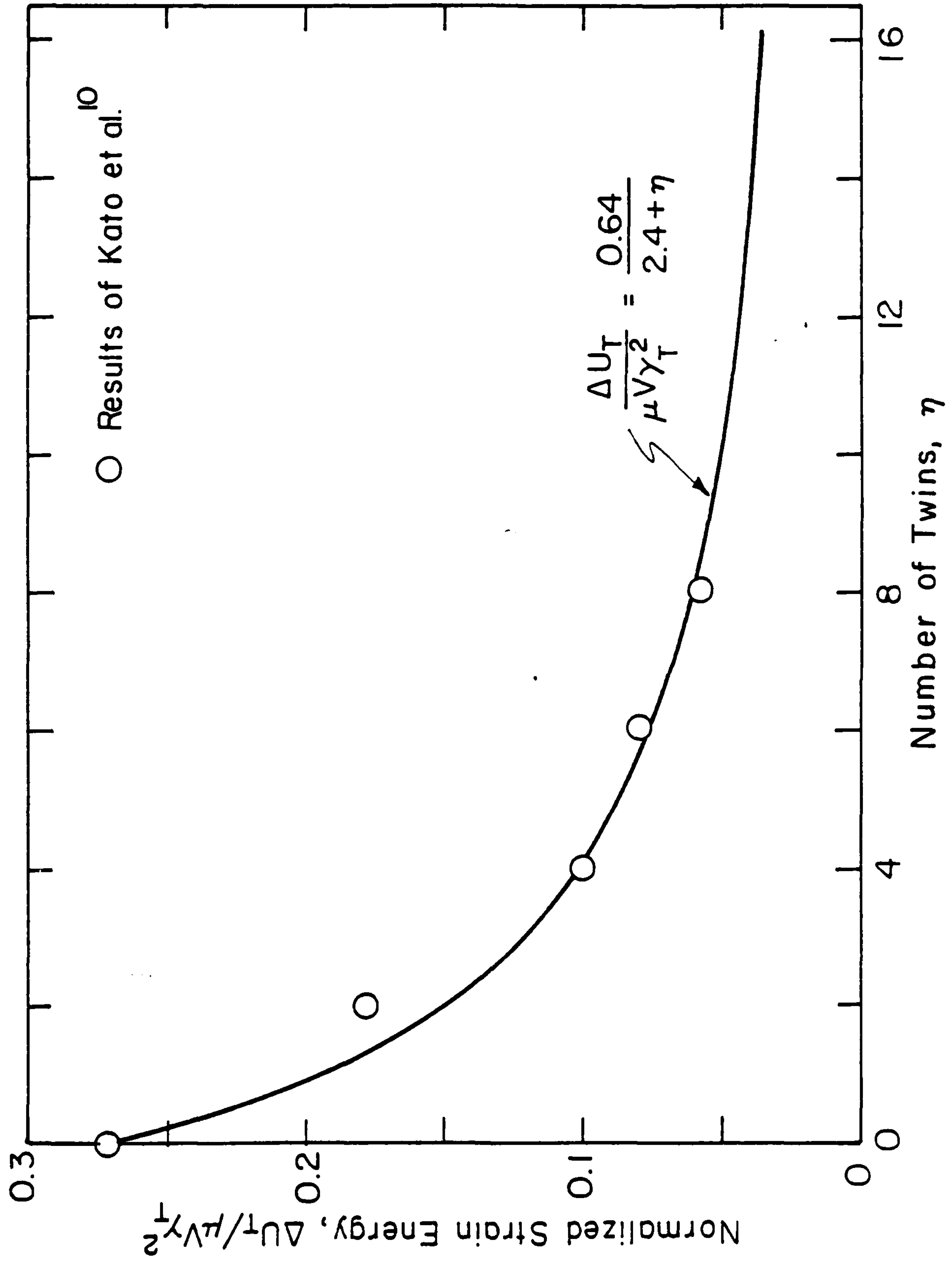

XBL 801-4542

Fig. 4

XBB 804-4296

Fig. 5

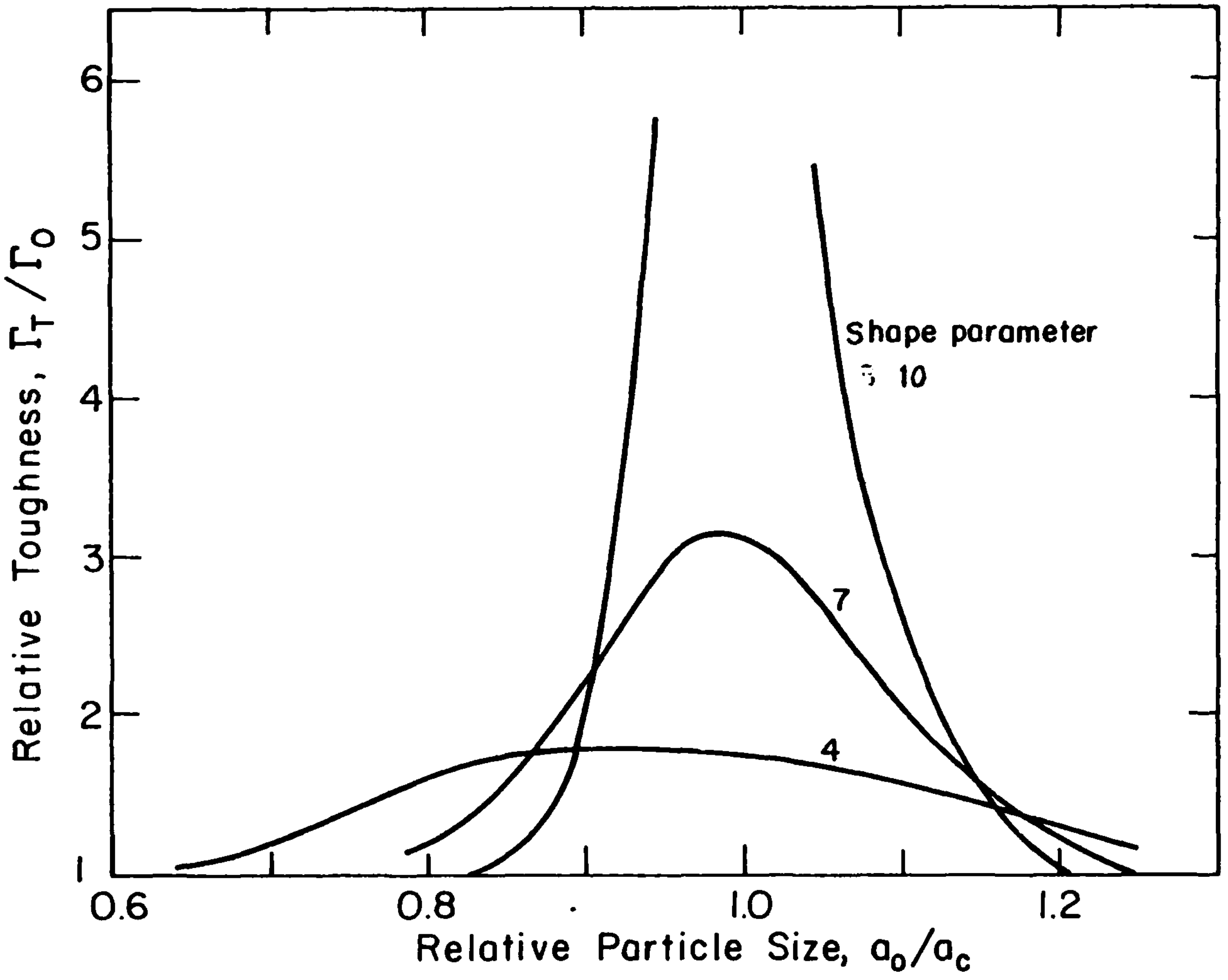

XBL 801-4539

Fig. 6

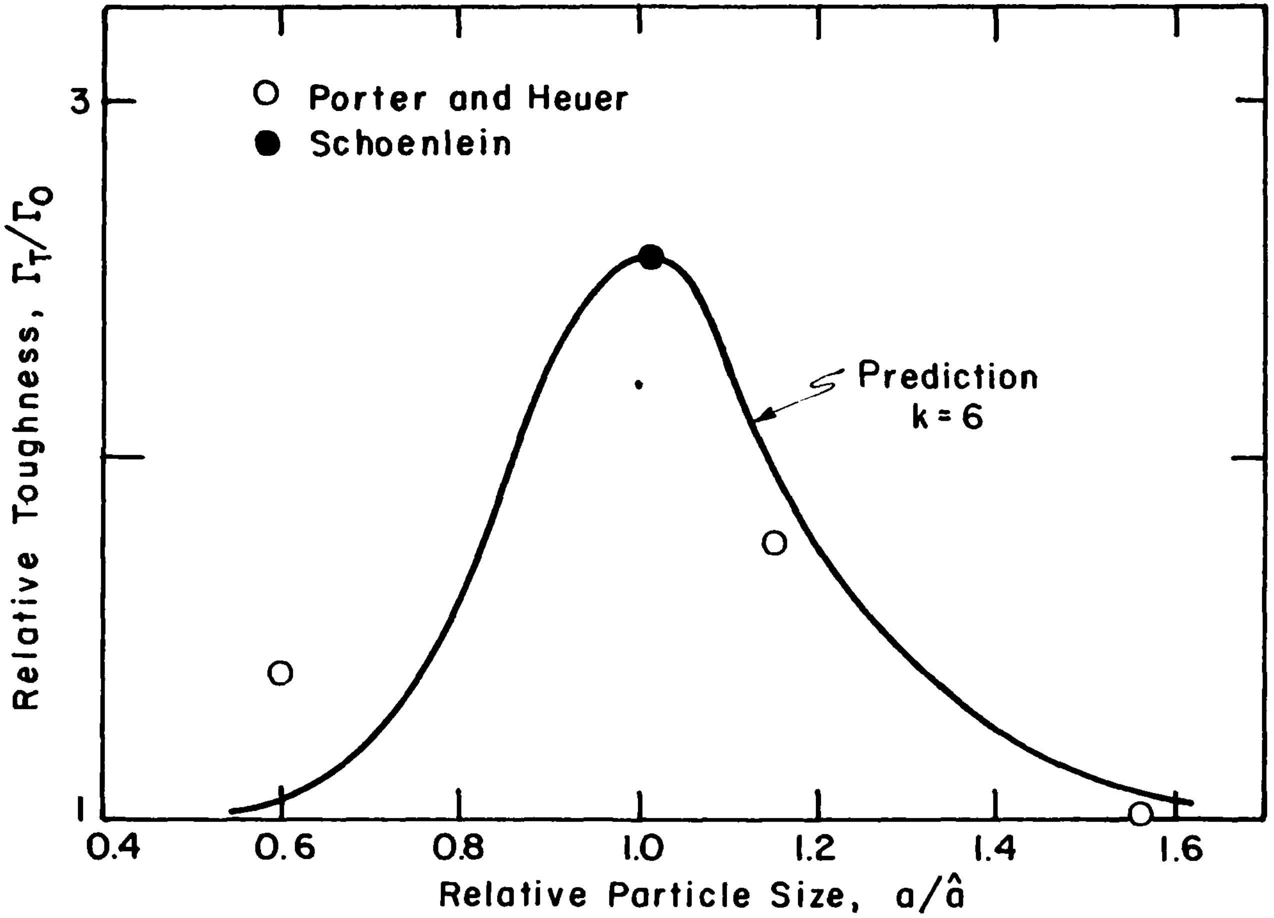

XBL 801-4541

Fig. 7

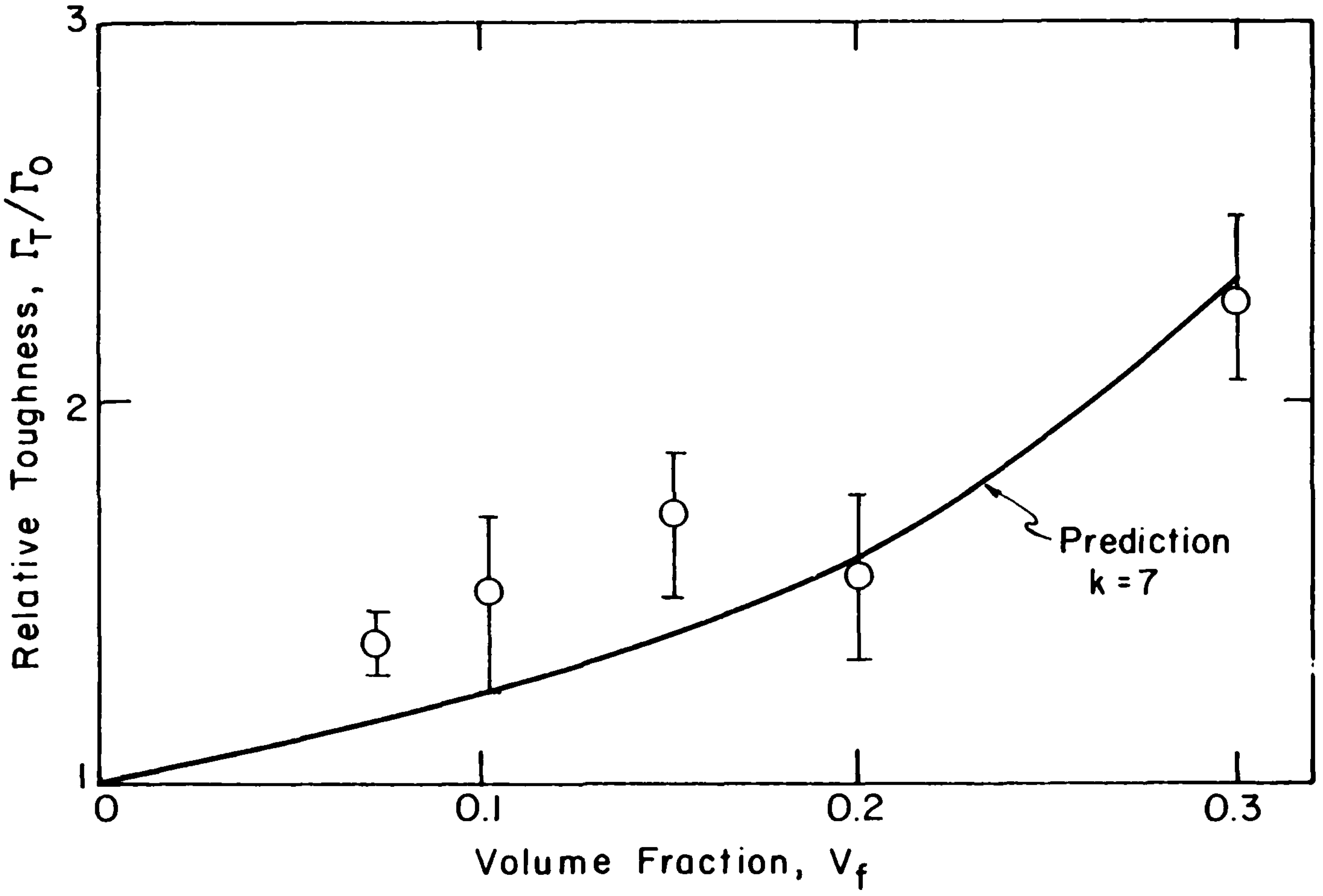

XBL801-4540

Fig. 8

CHAPTER III

QUANTITATIVE STUDIES OF THERMAL SHOCK IN CERAMICS BASED ON A NOVEL TEST TECHNIQUE

by

K. T. Faber, M. D. Huang, and A. G. Evans

Department of Materials Science and Mineral Engineering,
University of California,
Berkeley, CA 94720

ABSTRACT

A thermal shock test has been designed which permits the thermal fracture resistance and the mechanical strength of brittle materials to be quantitatively correlated. Thermal shock results for two materials, Al_2O_3 and SiC, have been accurately predicted from biaxial strength measurements and a transient thermal stress analysis (performed using a finite element method). General implications for the prediction of thermal shock resistance, with special reference to ceramic components, are discussed.

1. INTRODUCTION

Thermal transients are a ubiquitous source of fracture in ceramic components. A thorough comprehension of the variables that dictate thermal fracture are thus essential if the reliable performance of ceramics in fracture critical applications is to be achieved. A logical approach for evaluating the susceptibility of a ceramic component to failure during a thermal transient is based on a parity between thermal shock resistance and mechanical strength.* However, this approach has not been uniquely validated; in fact, certain observations on ceramics appear to be superficially inconsistent with the approach(1). Two comparative studies have been conducted(2,3) that afford some confidence in the pertinence of the mechanical strength for thermal shock prediction. Manson and Smith(2) presented statistical relations between mechanical strength (measured in flexure) and thermal shock resistance, and demonstrated that the statistical shape parameters deduced from both thermal shock and flexural strength tests (performed on steatite) were similar. However, they did not attempt a prediction of the absolute thermal failure condition from their mechanical strength data. More recently, the thermal failure of a precracked polymer(3) has been predicted from independent measurements of the crack dimensions and the critical stress intensity factor, by employing a numerical thermal stress analysis. In this study, an approximate choice of the heat transfer coefficient was used to provide reasonable predictions of the failure condition. The intent of the present paper is to provide a fully quantitative prediction of thermal failure. This is achieved by developing a suitable thermal shock test and by devising a method for the accurate calibration of the heat transfer coefficient; a method which involves the conduct of failure tests on a model brittle material (e.g. Al_2O_3). The thermal failure of another ceramic material (SiC) is then predicted from mechanical strength data by adopting the previously calibrated heat transfer coefficient.

---

*The mechanical strength refers to the stress level when the stress intensity factor at the fracture initiating flaw attains the critical value, K_{IC}.

A quantitative, but simple thermal shock test for evaluating and comparing ceramic materials (especially those suitable for advanced application such as gas turbine engines, heat exchangers and solar collectors) is not presently available. A procedure commonly adopted for thermal shock evaluation is based upon a water quench test(4); the results of which can be incorporated into established theories of fracture initiation and crack propagation(5). Under the high heat transfer conditions that prevail during a water quench, heat transfer and size effects have, in most previous studies, been assumed to be of negligible importance. The peak thermal stress, $\hat{\sigma}$, has then been calculated by applying the simple equation;

$$\hat{\sigma} = \frac{E\alpha\ \Delta T}{1 - \nu} \tag{1}$$

where E is Young's modulus, α is the coefficient of thermal expansion, ΔT is the temperature differential across the specimen and ν is Poisson's ratio. By setting the peak tension equal to the equivalent fracture stress of the material, an estimate of the maximum temperature differential, ΔT_c . that can be sustained by a material prior to severe strength degradation is then provided. However, the water quench test has several problems which limit its utility as a quantitative test for evaluating thermal shock resistance.

Firstly, it has recently been shown that the above relation is only independent of sample size when the samples are extremely large(6). Thus, ΔT_c shows a strong size dependence in many experiments, rendering material ranking somewhat questionable. Secondly, the heat transfer rates encountered in typical ceramic applications (cited above) are appreciably smaller than those enforced by a water quench. The magnitudes of the thermal stresses expected in these applications are thus smaller than anticipated by Eq.(1), and described by the general result:

$$\sigma = \left[\frac{E\alpha\ \Delta T}{1-\nu}\right] F\left(\frac{hr}{k}\right) G\left(\frac{kt}{c\rho r^2}\right) \tag{2}$$

where h is the heat transfer coefficient, k is the thermal conductivity, c is the specific heat, ρ is the density and r is a specimen dimension; the quantity hr/k is known as the Biot modulus, $kt/c\rho r^2$ is the Fourier number and F and G are functions(5). Hence, many more material parameters influence typical thermal shock failures than the elementary water quench test analysis admits. Thirdly, complex variations in the heat transfer coefficient with test conditions present appreciable interpretation difficulties. For example, in one study performed on a metal wire in water, h was found to vary by $>10^4$ between 20 and 400°C, due to boiling at the metal-water interface(8). Although the heat transfer variability can be essentially eliminated by quenching into oil, edge and corner effects cause futher difficulties.(9)

A thermal shock resistance testing and evaluation procedure which alleviates the difficulties associated with variable and very high heat transfer rates and edge effects is proposed in this paper. The rationale and the experimental procedure are firstly presented and discussed. A numerical stress analysis, essential to the detailed interpretation of the experimental results, is then described. Finally, some important implications for fracture prediction under thermal transients are discussed.

2. EXPERIMENTAL

2.1 Rationale

The mechanical fracture of a ceramic exhibits appreciable statistical variability. The statistical nature of the fracture also results in a fracture criticality that depends upon the stressed volume and the stress state. These statistically derived effects pose considerable limitations upon the direct comparison of mechanical fracture and thermal shock. This difficulty is alleviated if the comparisons are conducted on samples with controlled pre-cracks, which extend to failure with minimal statistical variability. The principal experimental results are those obtained on pre-cracked specimens. The pre-cracks are introduced at the locations of peak tension, to provide a basis for subsequent comparisons of normally prepared surfaces at the location of maximum fracture probability.

The experiments are designed to provide a comparison of the mechanical strength and the critical temperature for thermal fracture initiation, at a prescribed location and under equivalent stress states (equi-biaxial tension). This is achieved by employing disc samples, in which the edge stresses (and hence, undesirable edge initiated failure) can be essentially eliminated. The mechanical tests are conducted in a biaxial flexure mode; while the thermal tests utilize a disc at uniform initial temperature, cooled by a fluid jet impinging upon the disc center.

2.2 Procedures

Two materials were selected for the thermal shock study: a 99% dense sintered α-SiC (~ 7 μm grain size) and a fully dense slip cast Al_2O_3 (~ 15 μm grain size). The samples, 5 cm diameter discs, 0.25 cm thick, were ground and polished on one surface. Subsequently, the centers of the polished faces were precracked using a Knoop indenter with loads of 15 to 33N. Residual stresses caused by the indentation process were removed by fine grinding.(10)

Each sample (both precracked and non-precracked) was individually tested in the thermal stress apparatus shown in Fig. 1. The sample was mounted horizontally on fibrous insulation (with two thermocouples placed against the surface of the specimen) and heated in a $MoSi_2$ resistance tube furnace. The sample was allowed to equilibrate, at which time is was subjected to a rapid temperature change, through the use of high velocity air. The air was channeled onto the disc center, using a 0.32 cm diameter silica tube, at a velocity of ~ 100 ms^{-1}. After the quench, the sample was examined for crack extension. If the crack did not extend, the temperature differential between the sample and the air jet was incrementally enhanced until crack extension was detected. This critical temperature differential, ΔT_c, was recorded. Fractographic analysis was performed to insure that fracture originated at the precracks in the indented samples. Typical specimens failed by thermal shock are shown in Fig. 2.

Identical samples were tested in biaxial flexure at room temperature using the apparatus designed by Wachtman et al.(11). A 5 cm disc was supported on three equally spaced balls (concentric with the load) and loaded with a flat piston at the rate of $\sim 2\,\mathrm{MPa s^{-1}}$.

3. RESULTS

The variations in the critical imposed temperature differential with indent load obtained for Al_2O_3 are shown in Fig. 3. The results were obtained by employing successive 10°C temperature increments, prior to failure. Fracture in the precracked specimens occurred within a relatively narrow ΔT range for each precrack size. The critical temperature differential increased as the precrack size diminished, ranging between 480° and 580°C. The specimens with as-machined surfaces failed over a wider range of temperature: a phenomenon related to the flaw size distribution. The approximate failure times (obtained from the time when the temperature at the lower thermocouple registered a rapid decrease) were ~ 5 s.

Results for sintered α-SiC were more difficult to obtain, because this material is subject to time dependent strengthening (by oxidation or by surface diffusion) within the temperature range required to induce thermal fracture, $\gtrsim 1100°C$. It was elected, therefore, to obtain upper and lower bound values for ΔT_c by performing only a single thermal shock test on each precracked specimen (in contrast to the sequential testing employed with Al_2O_3). Firstly, a preliminary upper bound ΔT_c was established for each specific precrack size, by inducing thermal failure. Subsequent tests on specimens with the same precrack size were then performed at sequentially lower temperatures. The lowest temperature at which failure occurred was designated the upper bound, while the highest survival temperature was denoted the lower bound. The results obtained using this procedure are plotted in Fig. 3. It is noted that samples without precracks could not be thermally shocked within the temperature limitations of the present system (∿1500°C).

The biaxial flexure data for both materials are plotted as a function of the indentation load in Fig. 4. The theoretical slope(12) of -1/3 is superimposed to emphasize the trend. It is noted that SiC exhibits lower indentation strengths than Al_2O_3; a trend that probably reflects the fracture toughness characteristics of the two materials(12).

4. STRESS ANALYSIS

The thermal stresses that develop within the disc following impingement of the air jet were determined using axisymmetric finite element schemes. The temperature distributions were established by direct application of the program DOT(13). The temperatures were then used to ascertain the thermal stress, by an adaptation of the program SOLSAP.(14)

The calculations were conducted by allowing heat transfer through the upper surface of the disc, to the air stream. Radiation from the lower surface of the disc into the cooled regions was also permitted. The heat transfer coefficient was assumed to be uniform over the diameter of the air jet, with a magnitude proportional to that expected for a fluid stream flowing against a thin plate;(15)

$$h = \lambda \frac{k_f}{d} \left(\frac{v_\infty d}{\eta_f} \right)^{0.7} P^{1/3} \tag{3}$$

where k_f and η_f are the thermal conductivity and kinematic viscosity of the fluid at the film temperature, d is the jet diameter, v_∞ is the fluid velocity and P is the Prandtl number; λ is a proportionality constant, to be determined by a calibration procedure, described below.

Heat transfer was also considered to occur as a consequence of the jetting of the fluid over the surface. The heat transfer coefficient for boundary layer flow over a flat surface was selected,(15) and allowed to diminish inversely with distance from the jet, to account for flow attenuation. However, preliminary calculations indicated that reasonable choices for this heat flow exerted a relatively minor influence on the thermal stress developed at the disc center (the location of present interest).

Four axisymmetric element groups were employed in the study: an interior two dimensional element (group 1), a surface convection element with constant heat transfer (group 2), a surface convection element with h inversely proportional to radial distance (group 3) and a uniform radiation element (group 4). The assignment of these elements is illustrated in Fig. 5. Four different meshes were selected (Fig. 6) in order to ascertain the influence of the mesh definition and to establish convergence conditions. It was firstly established that consistent results emerged provided that the mesh distribution was relatively uniform both in the central region (of high heat transfer) and across the adjacent discontinuity in h. Thereafter, it was determined that a grid with 216 elements (grid (c) in Fig. 6) was the preferred choice for subsequent analysis. This grid yielded temperature distributions within 1% and stresses within 6% of those calculated with the finest grid (559 elements): an accuracy deemed sufficient for present purposes.

Temperature and stress calculations were conducted by admitting temperature dependent material properties: thermal conductivity, specific heat, thermal expansion coefficient (Fig. 7) and elastic modulus (~400 GPa for both materials). Typical temperature distributions within the test specimen, determined both across the surface and through the thickness, are plotted in Fig. 8. It is noted that there is an appreciable axial temperature gradient. Results for a thin disc can not, therefore, be expected to apply.

The time dependence of the maximum stress, at the center surface location, typically exhibits the form depicted in Fig. 9. It is observed that the peak stress develops at a time approximately coincident with the instant when the temperature at the disc periphery begins to diminish.

The procedure adopted for the calibration of the heat transfer coefficient involved calculations of the influence of h on the peak stress for Al_2O_3 at a specific temperature differential 575°C, pertinent to a 15N indentation precrack. The value of the heat transfer coefficient, h^*, that provided a peak tensile stress coincident with the biaxial fracture strength, for precracks of equivalent size (290 MPa), was then considered to be the correct value of h for that film temperature. A unique λ value for the test system was then deduced by inserting h^* into Eq. (3). The calibrated value of λ was employed for all subsequent stress calculations, yielding values of h that vary with temperature, through the temperature dependence of k_f and η_f (for the fluid medium).

Preliminary credence in the deduced value of h^* was established by comparing the measured failure times with estimates derived by analysis. For this purpose, it is noted that, since 10°C temperature increments were used to determine the incidence of fracture, the experimental estimate of ΔT_c could exceed the actual value by $< 10°C$. Stress levels developed at a 10°C temperature separation were thus calculated, and a lower bound on the failure time established from the time when the stress at the upper temperature attained the median failure stress (Fig. 9). The time of 12 s determined using this procedure is of the same order as the measured failure times.

A series of calculations were conducted for ΔT values within the vicinity of the values measured for each of the two materials. These calculations permitted relationships between ΔT and the peak stress $\hat{\sigma}$ to be deduced for each material within the pertinent ΔT range, as plotted in Fig. 10. Imposing the median biaxial failure stress for each precrack size (Fig. 4) then allowed the critical ΔT for each thermal shock test to be predicted.

The trends in thermal fracture predicted in this manner (Fig. 3) are remarkably consistent with the measured behavior. Of particular merit are the accurate predictions obtained for SiC, which fractures in a very different ΔT range than the calibration material (Al_2O_3), by virtue both of appreciable differences in k and α and of significant variations in K_c and h. It is also noted that superior predictions are obtained by excluding radiation from the lower surface of the specimen.

5. IMPLICATIONS

The close prediction of thermal shock failure from (surface crack dominated) biaxial strength measurements strongly supports the notion that thermal fracture can be uniquely related to the stress field produced by the temperature transient. Many thermal shock failures originate from surface cracks (because the thermal stress gradient encourages failure from near-surface located defects). The present validation of the thermal failure process for this important defect type should thus be of substantial merit for the prediction of thermal shock failure in ceramic components.

The calibration of the heat transfer conditions for the present test arrangement permits the apparatus to be used for the quantitative determination of thermal shock resistance for a range of ceramics. The comparison can be conducted on surfaces prepared in a manner analogous to that used for actual components, thereby averting the extraneous influence of specimen edges. (Also, the relative temperature invariance of the heat transfer coefficient permits a direct ranking of thermal shock resistance.) Such quantitative thermal shock tests would allow both the elucidation of the statistical character of fracture and would permit the magnitude of thermal (e.g., interrupted heat flow) sources of stress intensification pertinent to fracture from fabrication defects (voids, inclusions, etc.) to be evaluated.

For intrinsically thermal shock resistant materials (SiC, Si_3N_4), more severe heat transfer conditions than those presently employed would need to be devised, in order to induce fracture within the temperature capabilities of the test system. This might be achieved by increasing the specimen dimensions or, more expediently, by increasing the conductivity and decreasing the viscosity of the fluid (see Eq. (3)). An appropriate choice of fluid might be helium.

Finally, it is observed that the heat transfer calibration procedure adopted in the present study could provide an unequivocal method for heat transfer calibration in actual systems. Specifically, a small precrack could be placed at the location of maximum stress. Then, the time at which fracture initiates from the precrack could be measured, during a test run. Thereafter, a combination of the failure time with the magnitude of the failure stress at the crack would permit the heat transfer coefficient to be determined by comparison with a series of thermal stress calculations.

ACKNOWLEDGEMENT

The authors express their appreciation for the financial support of this research provided by the Carborundum Co. (K.T.F. and M.D.H.) and by the Office of Naval Research (A.G.E.) under contract no. N0014-79-C-0159.

FIGURE CAPTIONS

Fig. 1 A schematic of the thermal stress test apparatus.

Fig. 2 Thermally shocked discs

(a) a substantially supercritical thermal shock that activates many surface cracks

(b) a slightly supercritical thermal shock activating a central precrack.

To enhance the cracks the samples were immersed in a dye penetrant and illuminated under ultra-violet light.

Fig. 3 The influence of indentation load upon the critical temperature for thermal fracture of Al_2O_3 and SiC. Also shown are the critical temperatures predicted by the stress analysis from the biaxial strength results.

Fig. 4 The influence of indentation load on the biaxial flexure strength of Al_2O_3 and SiC.

Fig. 5 The assignment of the four types of element used in the finite element analysis.

Fig. 6 The four meshes employed in the finite element calculations. Mesh c was employed for the majority of calculations.

Fig. 7 Temperature dependent material properties of Al_2O_3 and SiC

(a) thermal conductivity

(b) specific heat

(c) thermal expansion

Fig. 8 The axial and radial temperature distributions in an Al_2O_3 sample subject to a temperature differential of 575°C, obtained at two times, 8s and 32s.

Fig. 9 The variation of the maximum tensile stress with time for Al_2O_3 subject to several values of ΔT. Also shown is the construction for estimating the lower bound failure time.

Fig. 10 The variation of the peak tensile stress with ΔT for (a) Al_2O_3, (b) SiC. Essentially identical results obtain for Al_2O_3 both with and without radiation; but a significant disparity exists for SiC, as illustrated.

REFERENCES

(1) T. K. Gupta, Jnl. Amer. Ceram. Soc., 55 (1972), 249.

(2) S. S. Manson and R. W. Smith, Jnl. Amer. Ceram. Soc., 38 [1] 18-27 (1955).

(3) Yagawa, G. and Masukazu, I., ASTM Eleventh National Symposium on Fracture Mechanics. Virginia Polytechnic Institute and State University, June 12-14, 1978.

(4) See for example, R. W. Davidge and G. Tappin, Proc. Brit. Ceram. Soc., 66 (1967), 405.

(5) Hasselman, D. P. H., "Unifed Theory of Thermal Shock Fracture Initiation and Crack Propagation in Brittle Ceramics," Jnl. Amer. Ceram. Soc. 52[11] 600-604 (1969).

(6) Becher, P. F. et al, "Thermal Shock Resistance of Ceramics: Size and Geometry Effects in Quench Tests," Amer. Ceram. Soc. Bull. 59 [5] 542-545 (1980).

(7) Jaeger, J. C., "Thermal Stress in Cylinders," Philos. Mag. 36 [257] 418 (1963).

(8) Ferber, E. A. and R. L. Scorah, "Heat Transfer to Water Boiling Under Pressure," Trans. ASME, 369-384 (1948).

(9) Emery, A. F. and A. S. Kobayashi, "Transient Stress Intensity Factors and Edge and Corner Cracks in Quench Test Specimens," Jnl. Amer. Ceram. Soc. 63 [7-8] 410-415 (1980).

(10) Petrovic, J. J. et al, "Controlled Surface Flaws in Hot-Pressed Si_3N_4," Jnl. Amer. Ceram. Soc. 58 [3-4] 113-116 (1975).

(11) Wachtman, Jr., J. B. et al, "Biaxial Flexure Tests of Ceramic Substrates," J. Mat. 7 [2] 188-194 (1972).

(12) B. R. Lawn, A. G. Evans, D. B. Marshall, Jnl. Amer. Ceram. Soc., in press.

(13) Polivka, R. M. and Wilson, E. L., "Finite Element Analysis of Nonlinear Heat Transfer Problems," University of California Structural Engineering Laboratory Report No. SESM 76-2, June 1976.

(14) Wilson, E. L., "SOLID SAP, A Static Analysis Program for Three Dimensional Structures," University of California Structural Engineering Laboratory Report No. UC SESM 71-19, Sept. 1971.

(15) Holman, J. P., Heat Transfer 3rd Edition; p. 186, McGraw-Hill, Inc., New York, 1972.

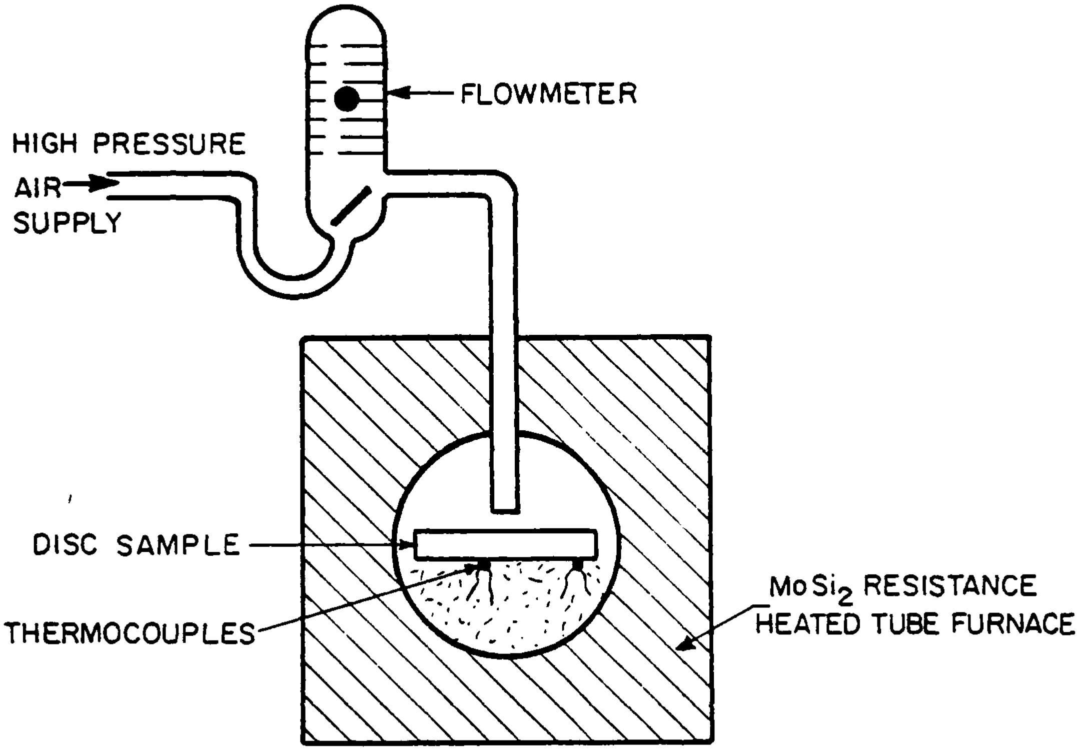
FLOWMETER
HIGH PRESSURE
AIR
SUPPLY
DISC SAMPLE
THERMOCOUPLES
$MoSi_2$ RESISTANCE
HEATED TUBE FURNACE

XBL 807-5569

Fig. 1

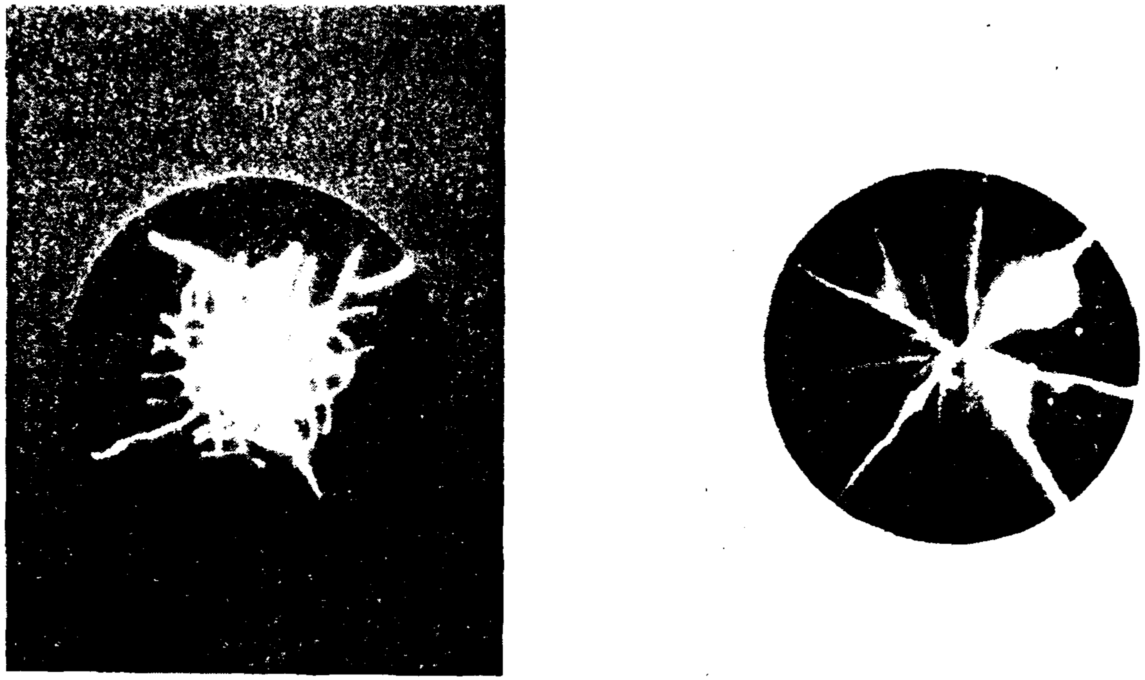

A

B

Fig. 2

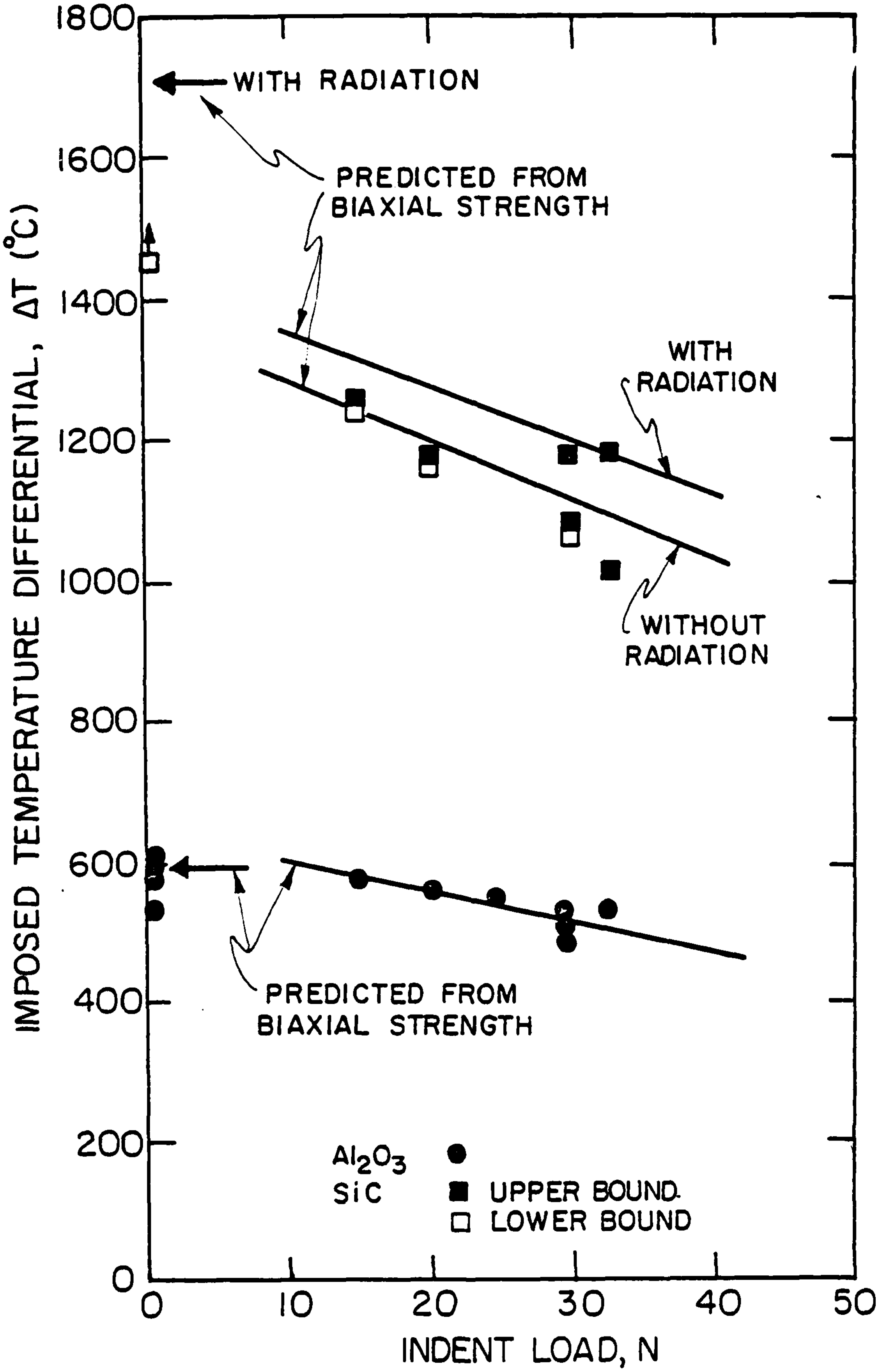

XBL 806-5291

Fig. 3

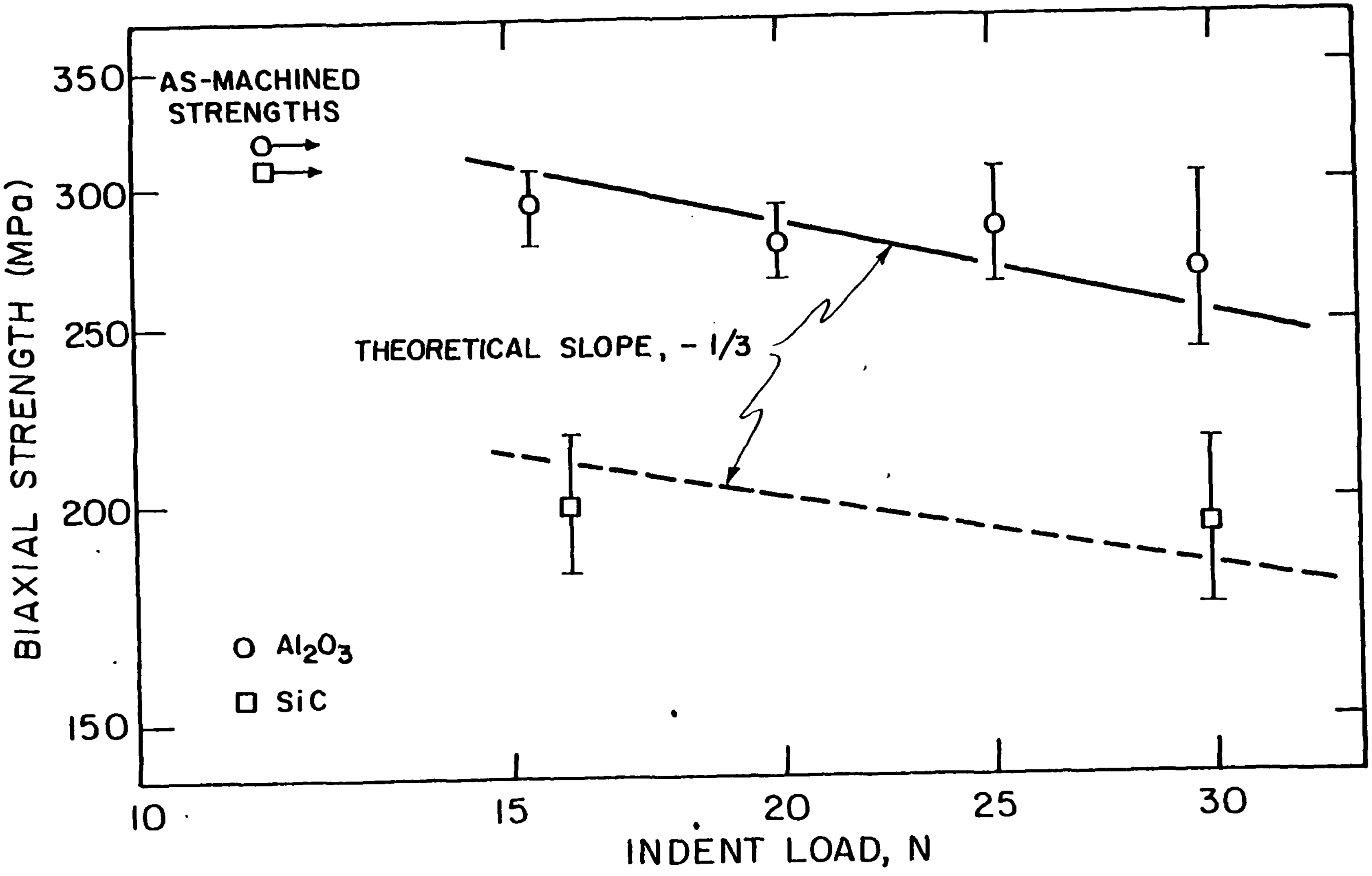

XBL 806-5293

Fig. 4

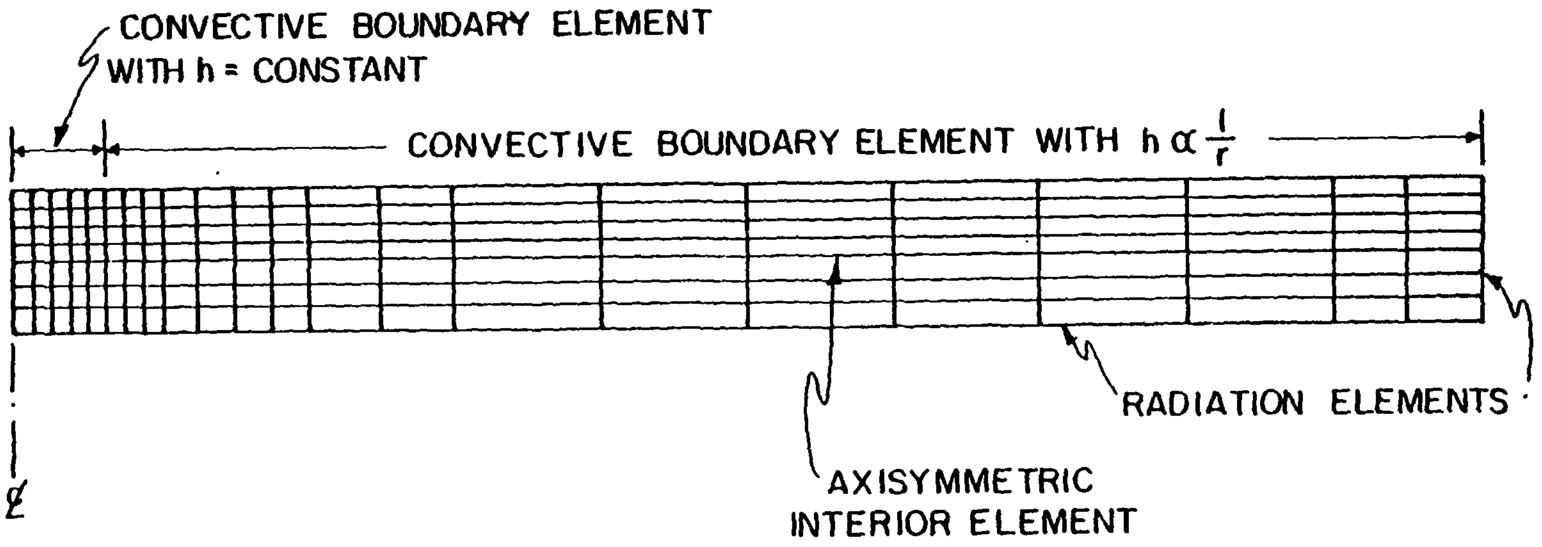
CONVECTIVE BOUNDARY ELEMENT
WITH h = CONSTANT
CONVECTIVE BOUNDARY ELEMENT WITH $h \propto \frac{1}{r}$
RADIATION ELEMENTS
AXISYMMETRIC
INTERIOR ELEMENT
$\mathcal{C}_L$

XBL 806-5292

Fig. 5

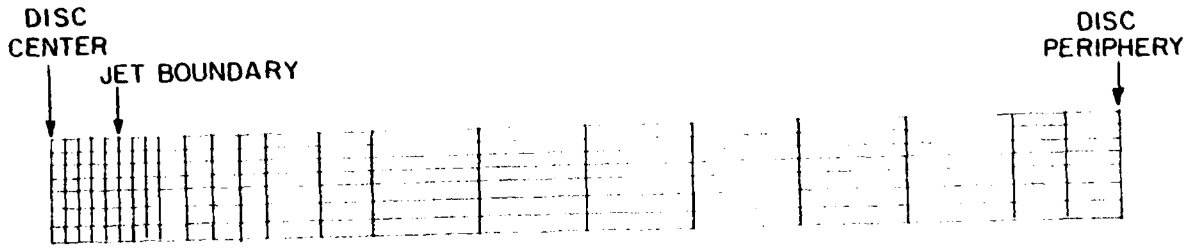
DISC CENTER
JET BOUNDARY
DISC PERIPHERY

(a) 154 ELEMENT MESH: UNIFORM CENTRAL DISTRIBUTION

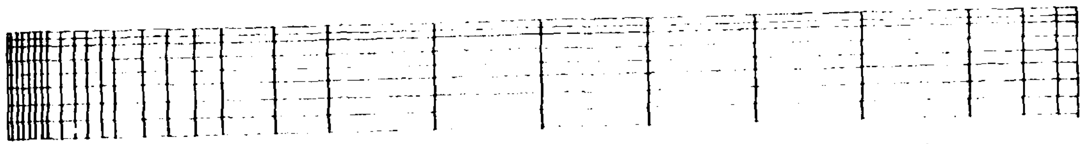

(b) 216 ELEMENT MESH: INHOMOGENEOUS CENTRAL DISTRIBUTION

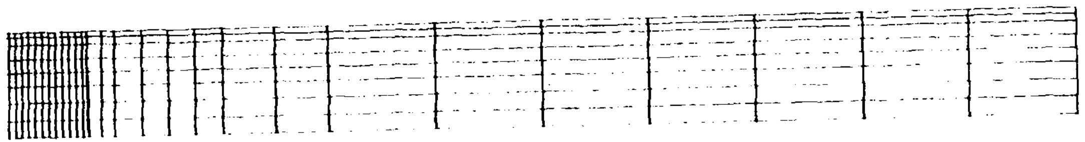

(c) 216 ELEMENT MESH: UNIFORM CENTRAL DISTRIBUTION

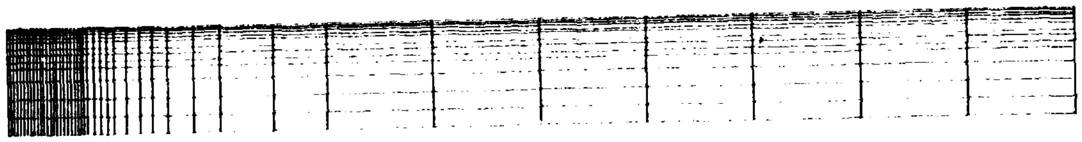

(d) 616 ELEMENT MESH

XBL 806-5297

Fig. 6

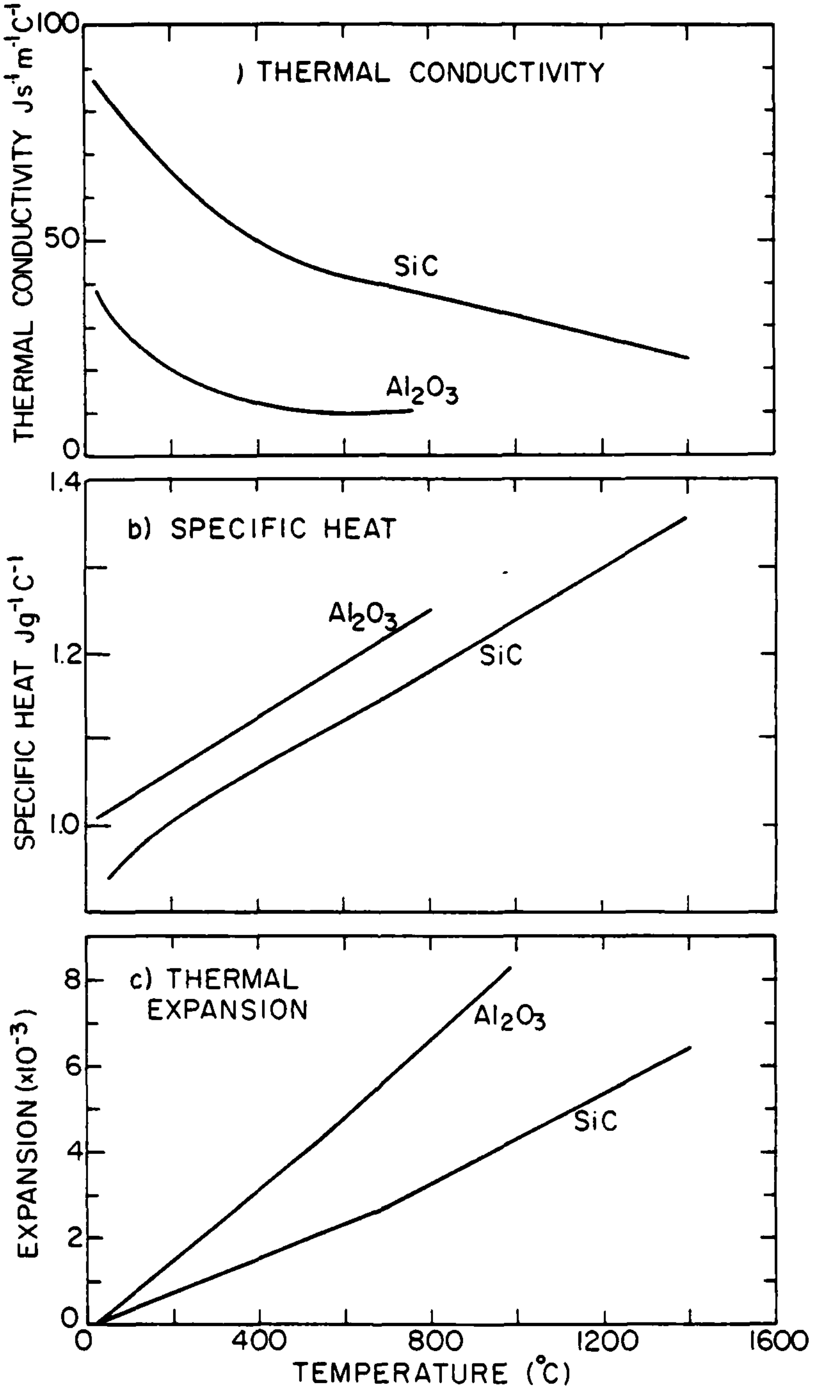

XBL 806-5298

Fig. 7

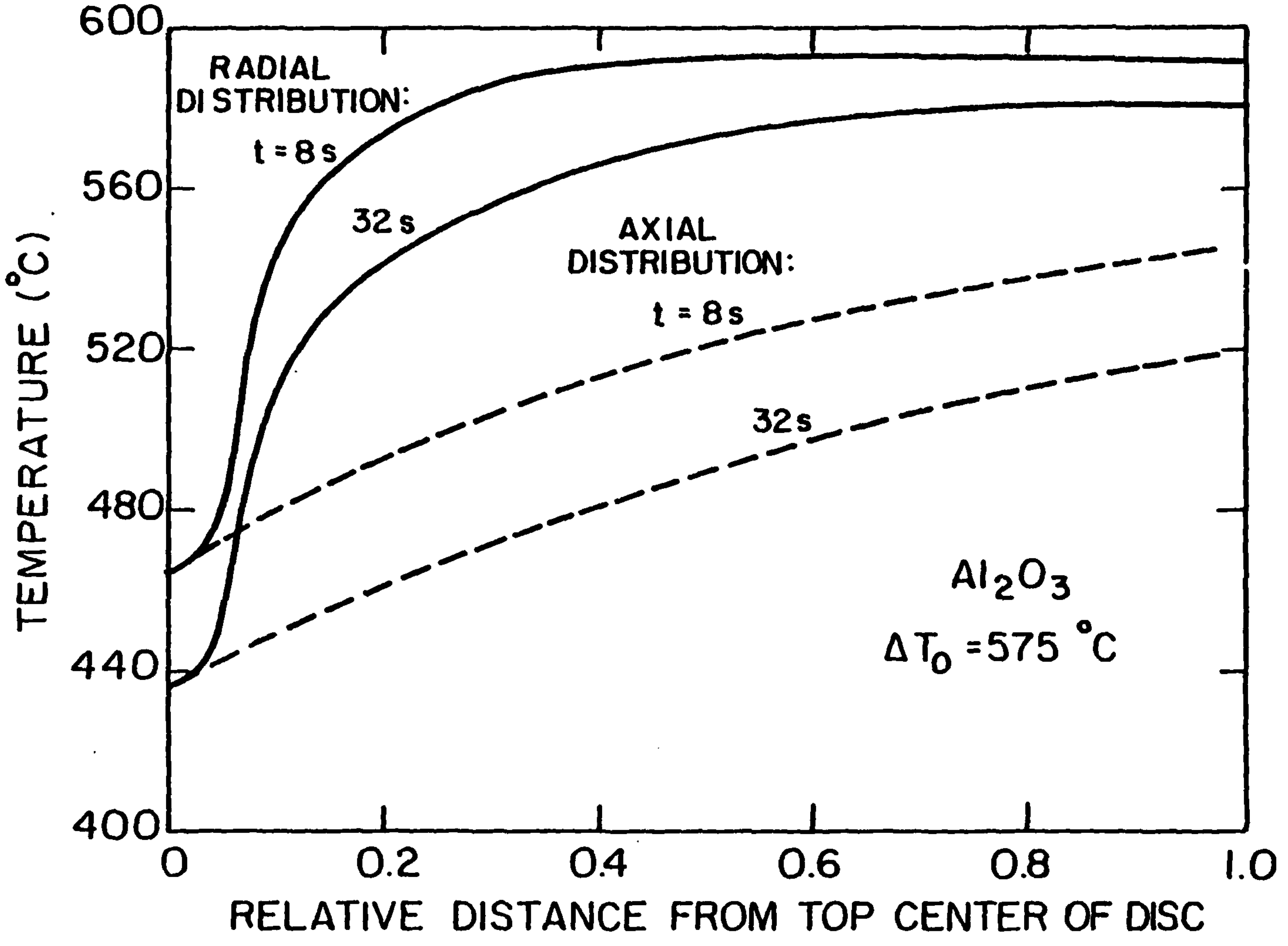

XBL 806-5296

Fig. 8

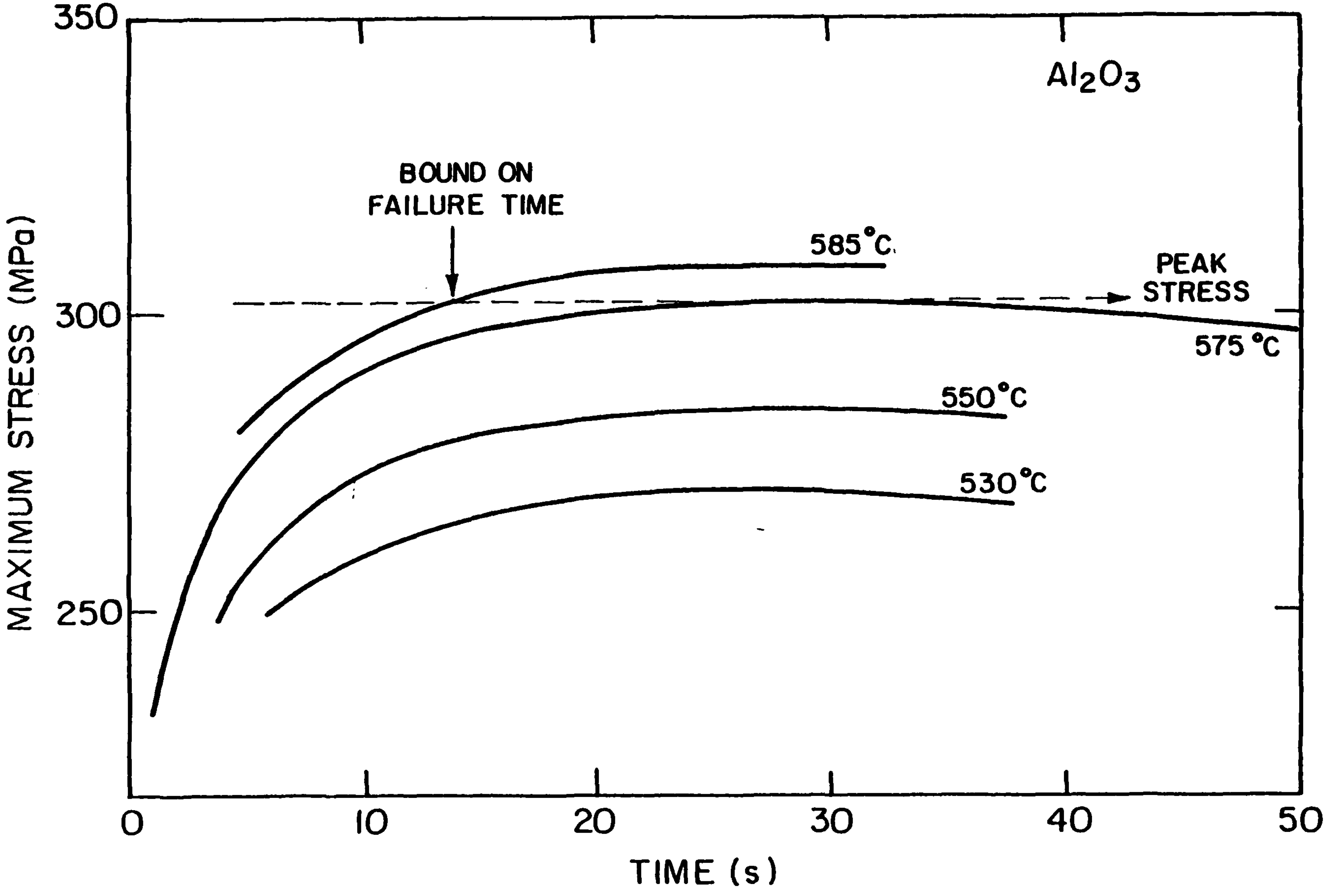

Fig. 9

XBL806-5295

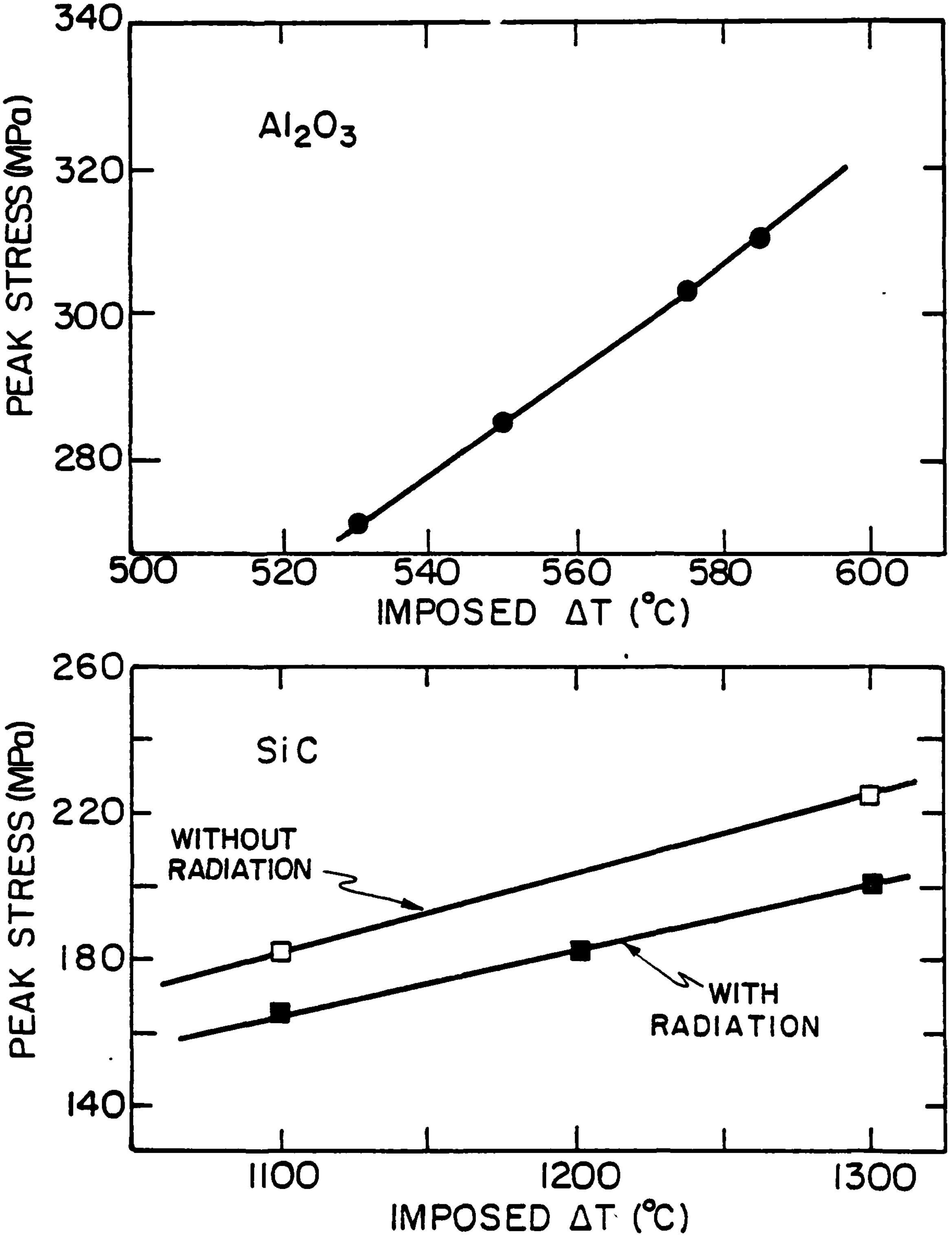

XBL 806-5294

Fig. 10

CHAPTER IV

TOUGHENING OF CERAMICS BY CIRCUMFERENTIAL MICROCRACKING

by

A. G. Evans and K. T. Faber

Department of Materials Science and Mineral Engineering,
University of California,
Berkeley, CA 94720

TOUGHENING OF CERAMICS BY CIRCUMFERENTIAL MICROCRACKING

by

A. G. Evans and K. T. Faber

Department of Materials Science and Mineral Engineering
Hearst Mining Building
University of California, Berkeley, CA 94720

ABSTRACT

An approximate analysis is presented of the toughening induced by the incorporation of second phase particles subject to microcracking. The toughening is demonstrated to become appreciable for a narrow size distribution of particles of appropriate size. The magnitude of the toughening is determined by the mismatch strain (due to thermal contraction incompatability) and the microfracture resistance of the particle/matrix interface. Implications for designing optimally tough ceramics are presented.

1. INTRODUCTION

The incidence of microcracking to form a process zone around macrocrack tips is now a well-substantiated phenomenon, for certain classes of brittle solids.[1,2,3] A comprehensive analysis of this problem has been elusive, however, because several complex, interactive effects accompany the microcracking process. Firstly, the microcracking increases the compliance of the process zone[4] and thereby, modifies the crack tip stress field from the initial linear elastic field (Fig. 1). Some simple approximations have been used,[5] but these are not fundamentally satisfying. Secondly, the microcrack density will tend to decrease with distance from the crack tip,[6] resulting in a diffuse process zone (Fig. 1), and a tendency for interaction with the boundaries of test samples. Thirdly, the criterion for coalescence of microcracks is uncertain. Coalescence with the primary crack is especially significant because this event determines the crack extension condition[6] and hence, dictates the toughness of the material.

A detailed study of the microcrack problem will inevitably involve a computer simulation. A first rational attempt at simulation has recently been reported by Hoagland and Embury,[7] using an image force (based on a Green's function derived by Hirth et al)[8] to account for compliance effects. Much additional study, based on this approach, will be needed to develop a comprehension of effects of microcracking on crack extension resistance curves and on toughness. This evaluation would be greatly facilitated by the availability of complementary approximate analytic solutions for specific microcrack problems. Such solutions would also provide invaluable guidance for research studies on the microstructural design of high toughness ceramics. One such solution is described in the present paper.

It must be recognized at the outset that stable microcracking in brittle materials generally results from large localized residual stresses that develop due either to thermal contraction anisotropy or to a phase transformation.[9,10] The tensile residual stresses superimpose on the applied crack tip stresses to initiate microcracking. A knowledge of the residual stresses is thus an important constituent of microcrack analyses.

A microcrack system of appreciable practical significance (that is also amenable to approximate analytic treatment) is a two-phase system containing second phase particles with a larger thermal contraction coefficient than the host.[11] Such particles tend to microcrack circumferentially[12] and thus, are intrinsically stable (the microcracks being confined to the immediate vicinity of the particles). This microcrack problem can be addressed using a simple thermodynamic approach, analogous to that recently described for martensitic toughening,[13] if appeal is made to two significant observations. Firstly, Davidge and Green[12] noted that, for this type of particle, the onset of microcracking can be adequately described by the condition that the total elastic energy exceeds the energy needed to create the crack surface. Some rationale for this result has recently been presented by Ito, et al.[14] Secondly, the computer simulations of Hoagland and Embury[7] have indicated that the extent of the microcrack zone is not appreciably different from that predicted by neglecting compliance effects. Hence, an approximate zone size can be estimated from the linear elastic field equations. These observations permit the zone size problem to be treated by evaluating the distance from the crack tip, r_c, at which a single particle satisfies the requirement that the change in thermodynamic potential of the system (before and after microcracking), becomes incrementally negative. The toughening can then be deduced from the process zone size.

The sequence of analysis in the present paper consists of a presentation of the governing thermodynamic relations, followed by an estimation of the process zone size. Thereafter, the toughening increment is evaluated and the implications for microstructural design are discussed.

2. THE GOVERNING THERMODYNAMIC RELATIONS

2.1. The Elastic Energy

The increase in strain energy $\Delta\phi_o$ of a system containing a single particle subject to a dilational transformation strain e^T is;[15]

$$\Delta\phi_o = -\left(\frac{e^T}{2}\right) p^I V_p \qquad (1)$$

where V_p is the particle volume and p^I is the stress within the particle. The transformation strain pertinent to the present problem is the thermal expansion mismatch strain; a strain that is essentially dissipated following separation of the particle from the matrix. Hence,

$$e^T = -3\Delta\alpha\Delta T$$

where $\Delta\alpha$ is the thermal expansion mismatch, assumed to be isotropic for both matrix and inclusion for this analysis, and ΔT is the cooling range. For an ellipsoidal inclusion, p^I is constant,[15] and eqn. (1) becomes:

$$\Delta\phi_o = -\frac{2\pi e^T p^I abc}{3} \tag{2}$$

where a, b and c are the semi-axes of the ellipsoid. The stress within the ellipsoid is;

$$p^I = -\frac{2E_m(e^T/3)}{(1+\nu_m)+2\beta(1-2\nu_p)} \tag{3}$$

where E_m is Young's modulus for the matrix and β is the ratio of moduli between the matrix and the particle (E_m/E_p). Combining eqns. (2) and (3) and simplifying for the case of a spherical inclusion, radius b, gives;

$$\Delta\phi_o = \frac{(4\pi/3)b^3(e^T)^2 E_m}{3\left[(1+\nu_m)+2\beta(1-2\nu_p)\right]} \tag{4}$$

which for $\nu_m \approx \nu_p \approx 0.2$ reduces to;

$$\Delta\phi_o \approx \frac{(4\pi/3)b^3(e^T)^2 E_m}{3.6(1+\beta)} \tag{5}$$

The increment in elastic energy (that derives from particle dilation) is modified in the presence of a uniform applied stress to,[15]

$$\Delta\phi_1 = \left(\frac{4\pi}{3}\right)b^3(e^T)^2\left[\frac{p^A}{(-e^T)} + \frac{0.3E_m}{(1+\beta)}\right] \tag{6}$$

where p^A is the dilational component of the applied stress. Note that an applied tension (as pertains to a crack tip field) augments the elastic energy in the presence of a particle with a larger expansion coefficient than the matrix, and thus encourages separation. However an additional elastic energy term is obtained in the presence of an applied stress; a term that derives from the interaction of the stress field with the elastic inhomogeneity, as reflected in the elastic modulus mismatch between the particle and matrix. The pertinent interaction energy is[15];

$$\Delta\phi_2 = \left(\frac{2\pi}{3}\right) b^3 \left\{ \frac{(\kappa_m-\kappa_p)}{9\kappa_m^2} \frac{(4\mu_m + 3\kappa_m)}{(4\mu_m + 3\kappa_p)} p^A p^A + \frac{15(\mu_m-\mu_p)(1-\nu)\, {}'p^A_{ij}\, {}'p^A_{ij}}{2\mu_m[2\mu_p(4-5\nu)+\mu_m(7-5\nu)]} \right\} \qquad (7)$$

where κ is the bulk modulus, μ the shear modulus and ${}'p^A_{ij}$ is the deviatoric component of the applied stress. For a Poisson's ratio of 0.2, eqn. (7) reduces to;

$$\Delta\phi_2 = \left(\frac{2\pi}{3}\right) b^3 \frac{(\beta-1)}{E_m(\beta+1)} \left[0.4\, p^A p^A + 2.4\, {}'p^A_{ij}\, {}'p^A_{ij}\right] \qquad (8)$$

When a particle separates from the matrix, the component of the elastic energy associated with the mismatch strain $\Delta\phi_1$ reduces to zero (Fig. 2). Whereas, the energy that derives from the elastic inhomogeneity changes to that for a void (obtained from eqn. (8) with $E_p = 0$) given by;

$$\Delta\phi_2^\circ = -\left(\frac{2\pi}{3}\right)\left(\frac{b^3}{E_m}\right) \left[0.4\, p^A p^A + 2.4\, {}'p^A_{ij}\, {}'p^A_{ij}\right] \qquad (9)$$

The change in elastic energy of a spherical particle following separation is thus;

$$\Delta\phi_{elastic} = -\frac{4\pi}{3} b^3 \left\{ (e^T)^2 \left[\frac{p^A}{(-e^T)} + \frac{0.3E_m}{(1+\beta)} \right] - \beta \frac{\left[0.4p^A p^A + 2.4\ {}'p^A_{ij}\ {}'p^A_{ij}\right]}{E_m(\beta+1)} \right\} \tag{10}$$

2.2 The Surface Energy

The increase in surface energy that accompanies circumferential fracture of an ellipsoidal particle is

$$\Delta\phi_s = 2\pi c^2 \gamma_{int} \left\{ 1 + \frac{b}{\sqrt{a^2-c^2}} \left[F(k,\phi) + \left[\left(\frac{a}{c}\right)^2 - 1 \right] E(k,\Psi) \right] \right\} \tag{13}$$

where

$$k = \left(\frac{a}{b}\right) \left[\frac{(b^2 - c^2)}{(a^2 - c^2)} \right]^{1/2}, \qquad \Psi = \cos^{-1}\left(\frac{c}{a}\right),$$

$F(k,\phi)$ and $E(k,\Psi)$ are elliptical integrals of the first and second kinds respectively, and γ_{int} is the pertinent fracture energy. Simplification of eqn.(13) can be achieved for a spherical particle, radius b,

$$\Delta\phi_s = 4\pi b^2 \gamma_{int} \tag{14}$$

2.3 The Change in Thermodynamic Potential of Separation

Neglecting compliance effects, in accord with our original premise, the change in the thermodynamic potential of the system following circumferential particle separation is;

$$\Delta\phi = \Delta\phi_{elastic} + \Delta\phi_s \qquad (15a)$$

and hence, for a spherical particle,

$$\Delta\phi = \frac{4\pi b^2}{3}\left\{3\gamma_{int} - b(e^T)^2\left[\frac{0.3E_m}{(1+\beta)} + \frac{p^A}{(-e^T)}\right] + \frac{0.4\beta b\left[p^A p^A + 6\,{}'p^A_{ij}\,{}'p^A_{ij}\right]}{E_m(1+\beta)}\right\} \qquad (15b)$$

A lower bound estimate of the applied stress needed to induce microfacture (obtained by setting $\Delta\phi \leqslant 0$) is thus embodied in the relation;

$$p^A - \left(\frac{0.4\beta}{(1+\beta)(-e^T)\,E_m}\right)\left[p^A p^A + 6\,{}'p^A_{ij}\,{}'p^A_{ij}\right] \geqslant E_m(-e^T)\left[\frac{3\gamma_{int}}{bE_m(e^T)^2} - \frac{0.3}{1+\beta}\right] \qquad (16)$$

The above result pertains to complete separation of the particle from the matrix. However, the change in thermodynamic potential for partial separation is expected to be closely similar to that given by eqn. (15). The relative invariance of $\Delta\phi$ with circumferential crack length $2a'$ can be deduced from the recent strain energy release calculations of Ito et al.$^{(16)}$, which yield a deviation in $\Delta\phi$, at $p^A = 0$ given by;

$$\delta\Delta\phi/\Delta\phi_{elastic} = -0.56\left[a'/b - \sin(a'/b)\cos(a'/b) - (1/3)\cos^3(a'/b)\right] - 1.06\cos(a'/b) + 0.88 \qquad (17)$$

which differs from zero by <4% for all a'/b. This small deviation may account for the success of the simple thermodynamic criterion for microcrack formation.

3. THE PROCESS ZONE SIZE

Prediction of the process zone size requires the introduction of a criterion for microcracking in the crack tip field. An upper bound estimate is presented in this section by simply invoking the requirement that particle separation occurs when $\Delta\Phi$ at the particle reduces to zero, by virtue of the influence of the crack tip stress field on the elastic energy of separation. The local stress used to assess the process zone dimension is assumed to be the linear elastic crack tip field and must, therefore, be regarded as an approximation.

The zone size r_c, for small zones relative to the crack length, can be estimated by inserting into eqn. (16) the crack tip stresses, given for plane stress conditions by$^{(16)}$;

$$p_{ij}^A = \frac{K}{\sqrt{2\pi r}} \left(\frac{\sin\theta}{2}\right)$$

$$p^A = \frac{K}{\sqrt{2\pi r}} \left(\cos\,(\theta/2)\right) \qquad (r \ll a) \qquad (18)$$

where K is the stress intensity factor, (r,θ) are the particle coordinates with respect to the crack tip and a is the crack length. The resultant quadratic equation for r_c is unwieldly and is thus not presented in detail. The zone width over the crack surface h (fig. 3) is of principal present interest. This dimension coincides with the angle of which a line parallel to the crack becomes tangent to the process zone, and occurs at $\theta \sim 0.42\pi$. For this angle and for $\beta = 1$, the zone width is given by $(h \ll a)$;

$$h = \frac{1}{\pi} \left(\frac{K}{E_m e^T}\right)^2 \Big/ \left[1 - \sqrt{1 - 3.7(3\Omega - 0.15)}\right]^2 \qquad (19)$$

where $\Omega = \gamma_{int}/E_m(e^T)^2 b$. This relation has two important limits.

Firstly, a solution does not exist for $b < 7\gamma_{int}/E_m(e^T)^2$, because the elastic energy increase from the inhomogeneity effect exceeds the elastic energy decrease associated with the mismatch strain, in regions close to the crack tip (where $e^A \rightarrow e^T$). A minimum particle size b_{min} is thus needed to induce a process zone;

$$b_{min} \approx \frac{7\,\gamma_{int}}{E_m(e^T)^2} \qquad (20)$$

Secondly, the zone size tends to infinity as the denominator in eqn. (19) tends to zero. This coincides with the condition for spontaneous (stress free) microcracking;

$$b_c \approx \frac{20\,\gamma_{int}}{E_m(e^T)^2} \qquad (21)$$

a result that has been frequently quoted in prior studies of microcracking(12,17,18,).

For most useful ranges of particle size, $b_c > b >> b_{min}$, eqn. (19) can be expressed by the simplified result ($h<<a$);

$$h \approx \frac{13}{\pi}\left(\frac{K}{E_m e^T}\right)^2 \frac{1}{[b_c/b - 1]^2} \qquad (22)$$

This relation allows $h \rightarrow \infty$ as $b \rightarrow b_c$; a limit that is not consistent with the requirement that the zone height be small with respect to the crack length. A convenient approach for establishing a limit on the zone height is to recognize that some microcracking will be induced at the level of the remotely applied stress, p_∞. These transformed particles cannot participate in the toughening, because they do not reflect a change in state during a crack increment. An approximate upper bound $\hat{h}$ for the process zone height that participates in the toughening is obtained from the zone dimension at which the stress given by eqn. (19) reduces to the level of the remote stress;

$$\hat{h} \approx \frac{0.8}{2\pi} \left(\frac{K}{p_\infty}\right)^2 \tag{23}$$

Equating eqn. (23) with eqn. (22) then permits the definition of an upper bound particle size $\hat{b}$ engaged in the toughening;

$$\hat{b}/b_c = [1 + 5\, e_\infty/e^T] \equiv 1 + \zeta \tag{24}$$

where e_∞ is the remotely applied strain.

4. THE TOUGHENING INCREMENT

The increment in toughening due to the formation of the microcrack process zone is governed by the detailed stress changes that occur in this zone and hence, the increase in the applied stress needed to induce crack extension. However, an approximate measure of the toughening can be deduced by examining the total change in energy of the system following a crack increment[13]. Neglecting the energy contained in stress waves, the toughening Γ_T is given by[13];

$$\Gamma_T \approx (\Delta\phi_s + \Delta\phi_0)\ h\ \frac{V_f}{(4/3)\pi b^3} + \Gamma_0 \tag{25}$$

where Γ_0 is the intrinsic resistance to crack extension, $\Delta\phi_0$ is the strain energy change after microcracking in the absence of an applied stress (the increment in process zone can be considered to be added at the essentially stress-free central portion of the crack),[13] and V_f is the volume fraction of particles. The most serious deficiency of eqn. (23) is the neglect of interaction effects between particles. The result should only be considered pertinent, therefore, for dilute particle concentrations. Estimation of the importance of interaction effects will require a numerical treatment. Relaxations that occur at the crack surface are also neglected; but this effect should be small for process zones $h \geqslant 3b$.

The microcrack toughening can be readily deduced from eqn. (25) for the ideal uniform particle size case; and this calculation is conducted first. Thereafter, an analysis of toughening in the presence of a size distribution of particles is attempted.

4.1 Uniform Particle Size Toughening

Combining eqns. (5), (14), (22) and (25), we obtain, for $\beta = 1$, $(b<\hat{b})$;

$$\Gamma_T \approx \frac{2V_f K^2}{\pi\, E_m[b_c/b-1]} + \Gamma_0 \tag{26}$$

However, K must be at the critical level K_c during a crack growth increment; hence, for linear behavior,

$$K^2 \equiv K_c{}^2 = E\,\Gamma_T \tag{27}$$

The toughening then becomes

$$\frac{\Gamma_T}{\Gamma_o} = \frac{1}{1-\eta}, \tag{28a}$$

where

$$\eta \approx \frac{2V_f}{\pi[b_c/b-1]} \tag{28b}$$

It should be noted that the dependence of the zone width on K has caused $\Gamma_T \to \infty$ as $\eta \to 1$. However, this condition will never be realised for fully confined process zones, characterised by the requirements (noted above) that the particles within the zone be smaller than $\hat{b}$. The implications of eqn. (28) in the range $\eta \to 1$ should thus be discounted. An approximate form of eqn. (28) suitable for subsequent analysis, that pertains over a useful range of η, is;

$$\frac{\Gamma_T}{\Gamma_o} \approx 1 + \left(\frac{2}{\pi}\right) \frac{V_f}{[b_c/b-1]} \tag{29}$$

The significance of the intrinsic toughness Γ_o in eqn. (28) requires amplification. The presence of detached or cracked particles adjacent to the crack tip will evidently reduce Γ_o from that for the dense matrix. The magnitude of the reduction will depend on the detailed distribution of the particles and the specific nature of the interactions between the microcracks and the primary crack. A first order estimate based on the reduction in load bearing area* would be:

---

*This estimate is probably pertinent to irregularly shaped particles larger than the matrix grain size. However, it should be noted that voids of regular shape in a homogeneous matrix can impede crack extension, even though the effective load bearing area is reduced. Alternate relations between Γ_o and Γ_m should thus be sought, if the microstructure suggests void impediment effects.

$$\Gamma_o \sim \Gamma_m(1-V_f) \tag{30}$$

where Γ_m is the matrix toughness. The trends with volume fraction predicted by this result are plotted in Fig. 4, for various particle radii ($b < b_c$) and for $\beta = 1$. It is evident from the figure that the appreciable increases in toughness occur for volume fractions up to ∿0.3. More significantly, however, it becomes apparent that the particle size must be relatively close to the critical value, in order to achieve appreciable toughening. This imposes a significant practical constraint upon the consistent attainment of high toughness.

Finally, it is noted that the toughening expressed by eqn. (28) is independent of particle shape (however the shape does have an appreciable influence on the critical particle size).

4.2 Particle Size Distribution Effects

The introduction of a distribution of particle sizes evidently results in a degradation of the maximum toughening anticipated by the uniform particle size analysis. The specific influence of a size distribution can be demonstrated to coincide with the replacement of V_f in eqn. (26) with the equivalent distribution function, yielding the relation

$$\frac{\Gamma_T - \Gamma_o}{\Gamma_T} = \left(\frac{2}{\pi}\right) \frac{V_f}{\langle b^3 \rangle} \int_{b_{min}}^{\hat{b}} \frac{b^4 \phi(b) db}{(b_c - b)} \tag{31}$$

where $\phi(b)db$ is the particle size distribution function and V_f is now the total volume fraction of particles. The major contribution to the toughening derives from particles in the size range just below the critical size $\hat{b}$. Hence, since high toughness requires an appreciable fraction of the population to be uncracked $(b < \hat{b})$ in the absence of an external stress, the large extreme of the particle size distribution is of primary interest. An extreme value function is thus selected for ascertaining size distribution effects,[19]

$$\begin{aligned}\Phi &= 1 - \exp[-(b_o/b)^k] \\ \phi(b)db &= \frac{k(b_o)^k}{b^{k+1}} \exp[-(b_o/b)^k]db\end{aligned} \tag{32}$$

where b_o and k are the scale and shape parameters respectively. Combining eqns. (31) and (32) gives

$$\begin{aligned}\frac{\Gamma_T - \Gamma_o}{\Gamma_T} &= \left(\frac{2}{\pi}\right) \frac{k(b_o)^k V_f}{[\Gamma(1-3/k)]\lambda^{3/k} b_c^3} \int_{b_{min}}^{\hat{b}} \frac{e^{-(b_o/b)^k} db}{b^{k-3}(b_c-b)} \\ &= \left(\frac{2}{\pi}\right) \frac{V_f \lambda^{(1-3/k)}}{[\Gamma(1-3/k)]} \int_{(1+\zeta)^k}^{3k} \frac{z^{-3/k}\, e^{-\lambda z} dz}{(z^{1/k} - 1)} \\ &= \left(\frac{2}{\pi}\right) V_f\, A(b_c/b_o, k, \zeta)\end{aligned} \tag{33}$$

where $\lambda = (b_o/b_c)^k$, $z = (b_c/b)^k$, $\Gamma(k)$ is the gamma function and $A(b_c/b_o, k)$ is obtained by numerical integration. The relative toughening given by eqn. (33) is plotted in Fig. 5 for two choices of ζ (1×10^{-1} and 1×10^{-2}). The peak value of the toughness Γ_T varies appreciably with the width of the particle size distribution (as reflected by the shape parameter k), such that $\hat{\Gamma}_T$ increases as the width decreases (i.e. as k increases). There are also important effects of the remote strain level (reflected in the ζ dependence) which imply an influence of crack length (and test method) on the fracture toughness. A characterization of the particle size distribution and a determination of geometry effects thus become essential prerequisites for the interpretation of experimental toughening results. More significantly, the results imply that a narrow particle size distribution is needed if appreciable toughening is to be realized, in accord with this mechanism.

The toughening anticipated by eqn. (33) can be related to the intrinsic toughness of the matrix, by recognizing that separation of essentially all particles with a size $b > b_{min}$ will have occurred as the crack tip is approached, i.e., as $r \to 0$ and hence, $e^A \to \infty$. The area of matrix exposed to crack extension is thus reduced by an amount related to the total volume fraction of particles V_f. The toughening thus becomes

$$\frac{\Gamma_T}{\Gamma_m} = \frac{\pi(1-\xi V_f)}{\pi - 2V_f A(b_c/b_o, k, \zeta)} \tag{34a}$$

where ξ is the fraction of particles with size $> b_{min}$

$$\xi = 1/\langle b^3 \rangle \int_{b_{min}}^{\infty} b^3 \phi(b)\,db \tag{34b}$$

Typical values of ξ are plotted in fig. 6.

5. IMPLICATIONS AND CONCLUSIONS

An analysis of toughening caused by the separation of second phase particles from the circumventing matrix, within a crack tip process zone, has been presented. The most critical variables that influence the toughness are the proximity of the median particle size distribution: narrow distributions close to the critical being preferred. The magnitude of the critical particle size is, in turn, dependent upon several material variables: notably the crack propagation resistance of the interface, the elastic moduli, the thermal contraction coefficient, and the particle shape. These variables offer extensive opportunities for designing microstructures that optimize the toughening available from this particular microcrack toughening mechanism.

The analysis also suggests that discrete microcrack process zones will only be observed for a limited range of particle size and applied strain levels, as characterised by a minimum size for particle separation and a maximum size for separation at the level of the applied strain. The toughening is thus anticipated to exhibit trends that depend sensitively upon the strain induced by microcracking relative to the applied strain.

ACKNOWLEDGEMENTS

The authors wish to thank the Office of Naval Research for financial support under contract N0014-79-C-0159 and one us (K.T.F.) thanks the Carborundum Company for financial assistance.

REFERENCES

1. R. G. Hoagland, G. T. Hahn and A. R. Rosenfield, Rock Mech. 5 (1973) 77.
2. C. C. Wu and R. W. Rice, to be published.
3. N. Claussen and J. Steeb, J. Amer. Ceram. Soc. 59 (1976), 49.
4. A. G. Evans, A. H. Heuer and D. L. Porter, Fracture 77 (Ed. D. M. R. Taplin), Univ. Waterloo Press, Vol. 1, p 529 (1977).
5. F. E. Buresch, Fracture 1977 (Ed. D. M. R. Taplin) Univ. Waterloo Press, Vol. 3, p 929 (1977).
6. A. G. Evans, Scripta Met. 19 (1976) 93.
7. R. G. Hoagland and J. D. Embury, J. Amer. Ceram. Soc., 63 (1980) 404.
8. J. P. Hirth, R. G. Hoagland, P. C. Gehlen, Int. J. Solids Structures 10 (1974) 977.
9. A. G. Evans, Acta Met. 26 (1978) 1845.
10. D. R. Clarke, to be published.
11. M. Borom, A. M. Turkalo and R. H. Doremus, J. Amer. Ceram. Soc. 58 (1975) 385.
12. R. W. Davidge and T. J. Green, Jnl. Mater. Sci. 3 (1968) 629.
13. A. G. Evans and A. H. Heuer, J. Amer. Ceram. Soc., 63 (1980) 241.
14. Y. M. Ito, M. Rosenblatt, F. F. Lange and A. G. Evans, Int. J. Frac. to be published.
15. J. D. Eshelby, Proc. Roy. Soc. A252 (1959) 561.
16. B. R. Lawn and T. R. Wilshaw, Fracture of Brittle Solids (Cambridge Univ. Press) 1976.
17. J. J. Cleveland and R. C. Bradt, J. Amer. Ceram. Soc., 61 (1978) 478.
18. R. W. Rice and R. C. Pohanka, J. Amer. Ceram. Soc. 62 (1979) 559.

19. A. G. Evans, B. R. Tittmann, L. Ahlberg, G. S. Kino and B. T. Khuri-Yakub, J. Appl. Phys. 49 (1978) 2669.

FIGURE CAPTIONS

Fig. 1. A microcrack process zone and a schematic of the stress modifications expected within the vicinity of the crack tip.

Fig. 2. A schematic indicating both the stresses that the particle is subject to in a crack tip field prior to separation, and the stress free state of the particle following separation.

Fig. 3. A predicted process zone contour, indicating the transformation zone width h_T.

Fig. 4. Trends in toughness with volume fraction for given values of particle size.

Fig. 5. The predicted toughening plotted for several shape parameters k as a function of the ratio of the scale parameter to the critical size (a) for an applied strain characterized by $\zeta = 10^{-1}$ (b) $\zeta = 10^{-2}$.

Fig. 6. The variation of the area fraction of particles separated as a function of the ratio of the scale parameter to the critical size.

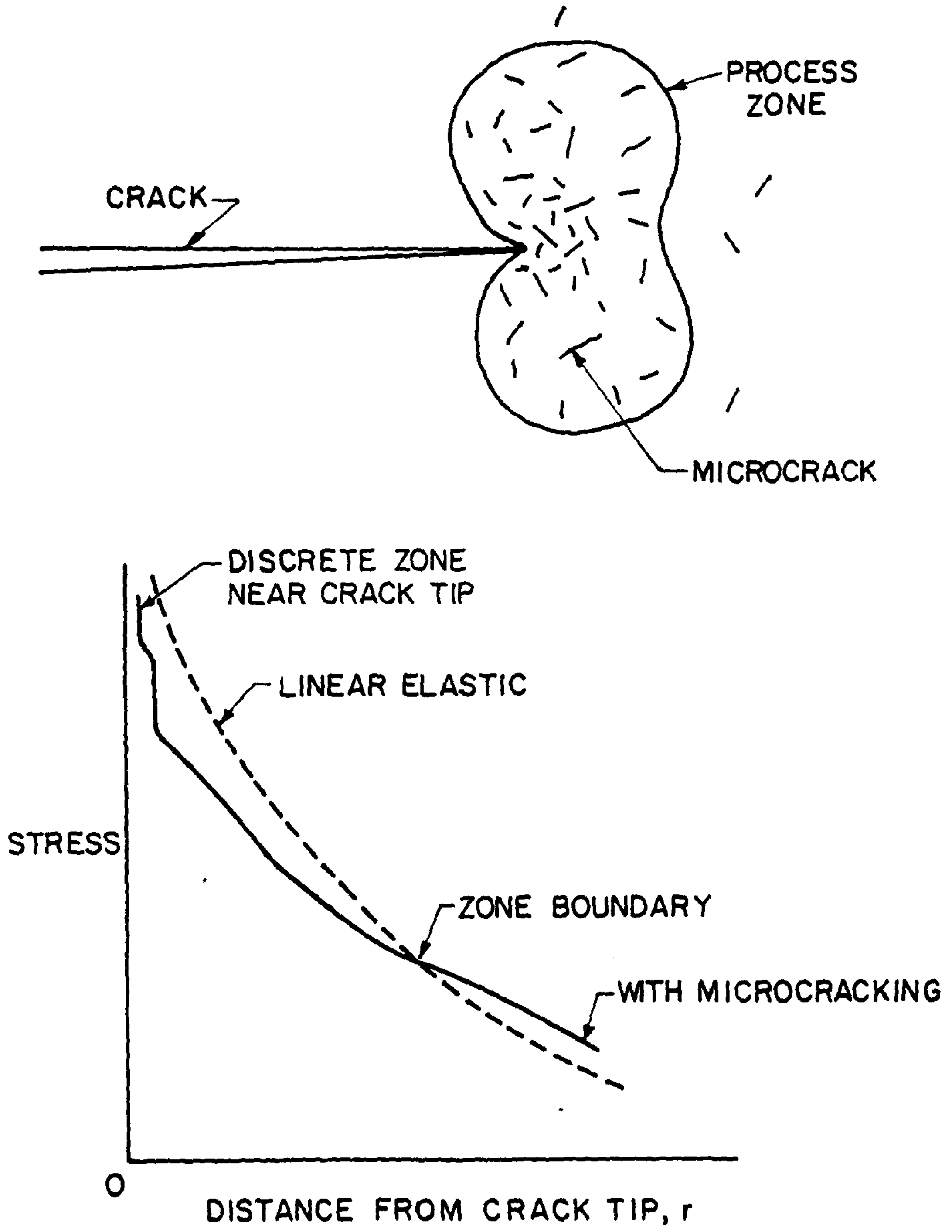
PROCESS ZONE
CRACK
MICROCRACK
DISCRETE ZONE NEAR CRACK TIP
LINEAR ELASTIC
STRESS
ZONE BOUNDARY
WITH MICROCRACKING
0
DISTANCE FROM CRACK TIP, r

XBL 798-6744

Fig. 1

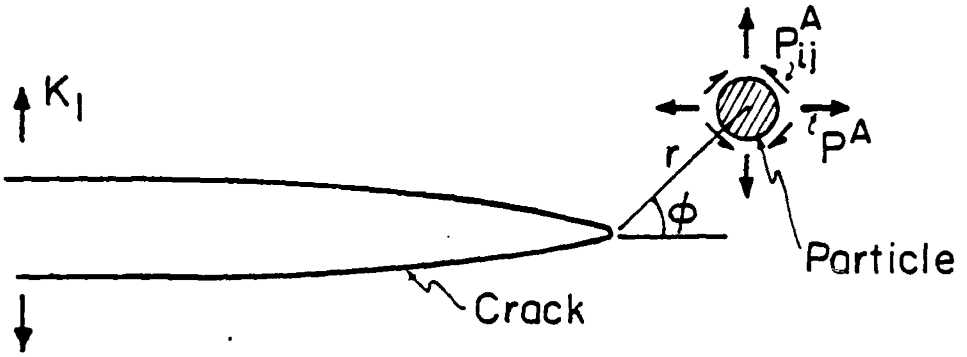
K_1
P_{ij}^A
${}^iP^A$
r
ϕ
Particle
Crack

a) Condition Prior to Separation

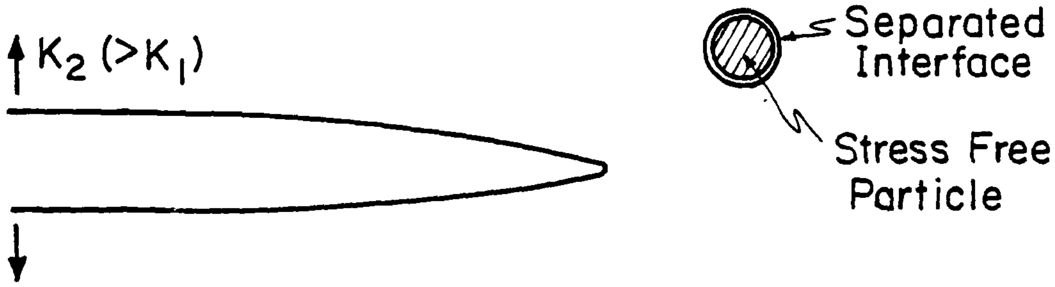
K_2 (>K_1)
Separated Interface
Stress Free Particle

b) Condition Following Separation

XBL 801-4543

Fig. 2

AD-A098 966 CALIFORNIA UNIV BERKELEY DEPT OF MATERIALS SCIENCE A--ETC F/G 11/2
IMPACT DAMAGE AND EROSION OF CERAMICS AND COMPOSITES.(U)
DEC 80 A G EVANS, N BURLINGAME, S S CHIANG N00014-79-C-0159

UNCLASSIFIED NL

2 OF 3
AD
AD [illegible]

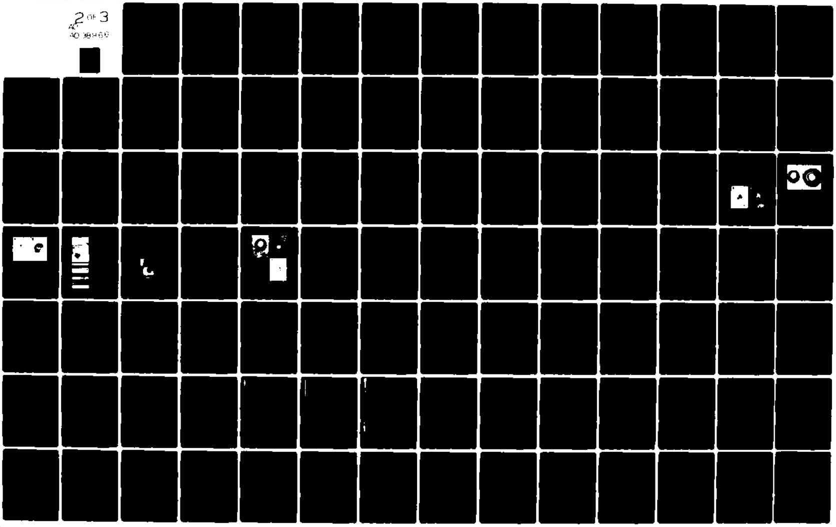

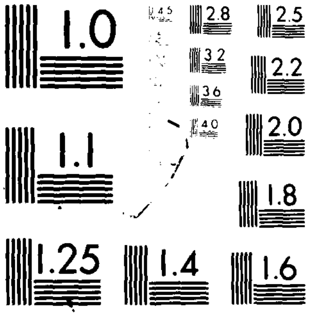
1.0
4.5
2.8
2.5
3.2
2.2
3.6
4.0
2.0
1.1
1.8
1.25
1.4
1.6

MICROCOPY RESOLUTION TEST CHART
NATIONAL BUREAU OF STANDARDS-1963-A

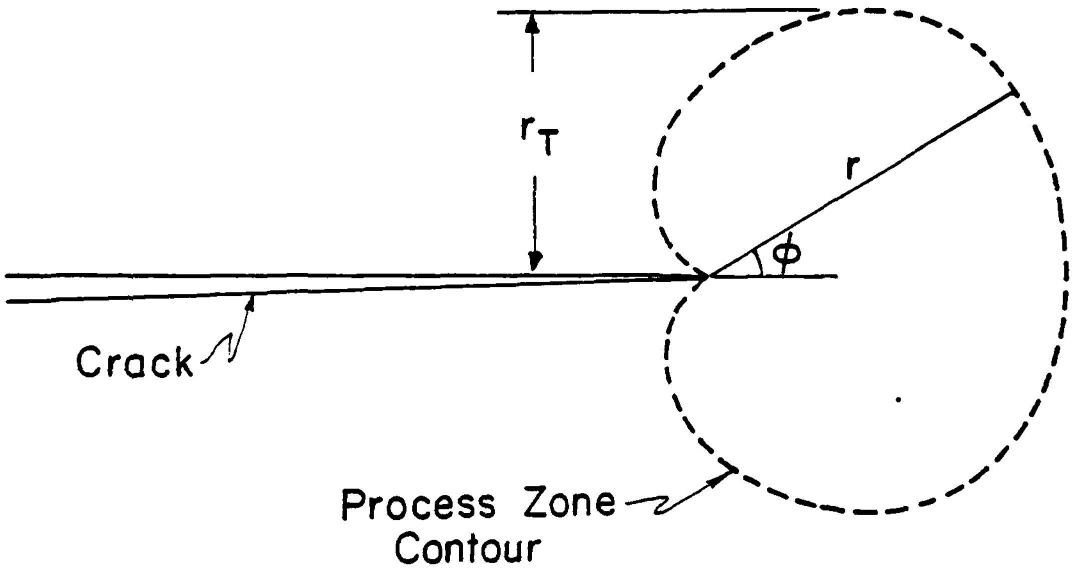
r_T
r
ϕ
Crack
Process Zone
Contour

XBL 801-4544

Fig. 3

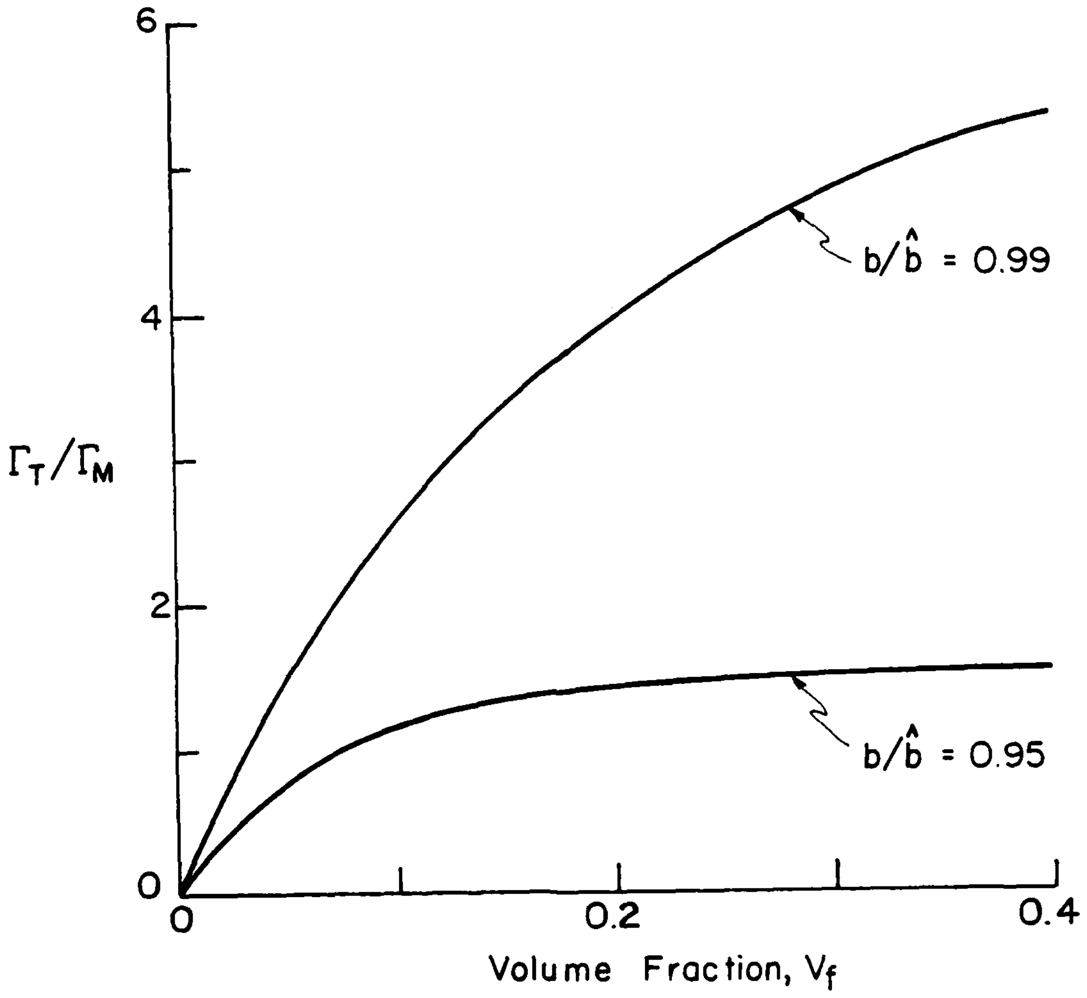

XBL 801-4546

Fig. 4

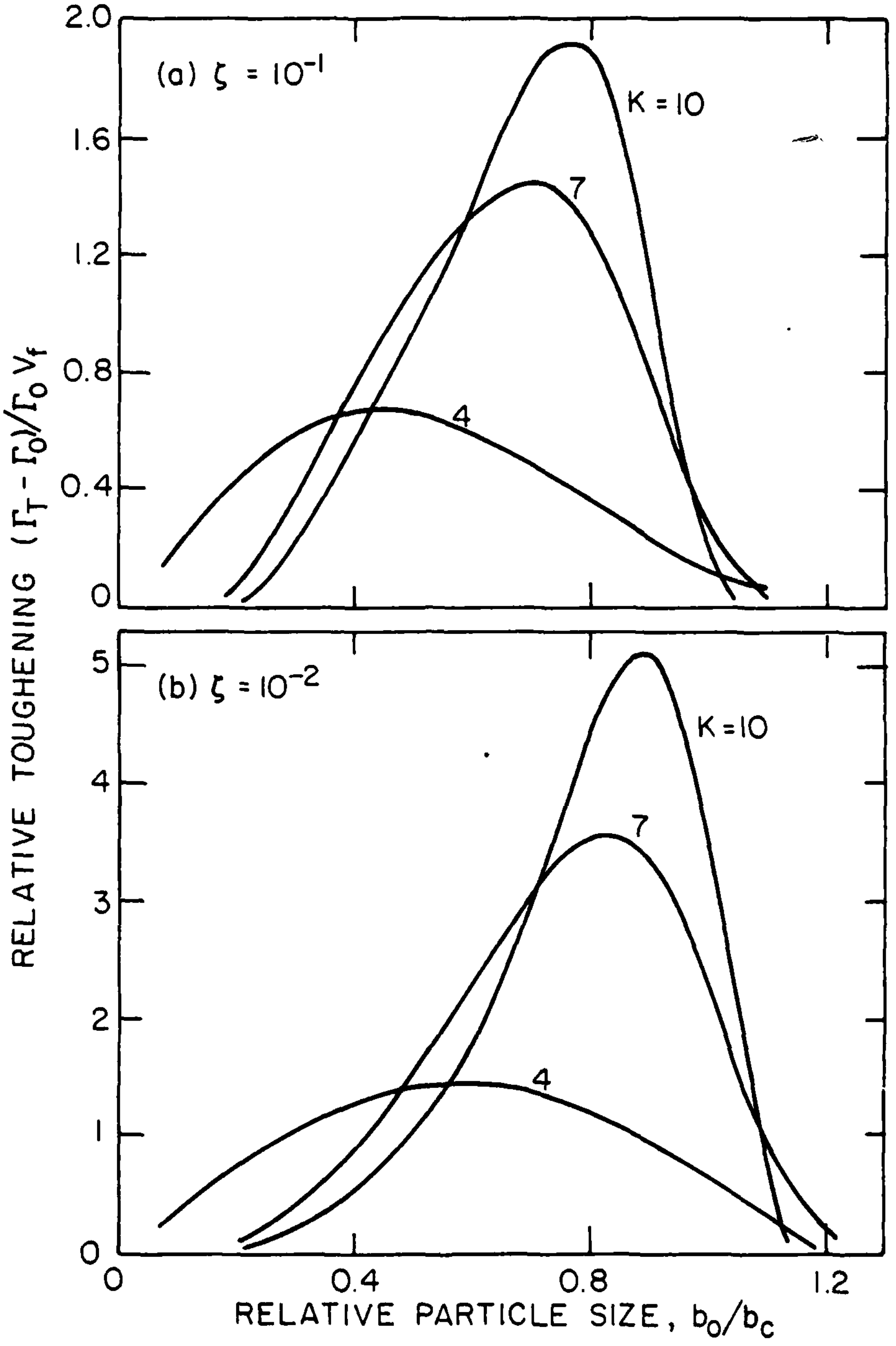

XBL 809-5893

Fig. 5

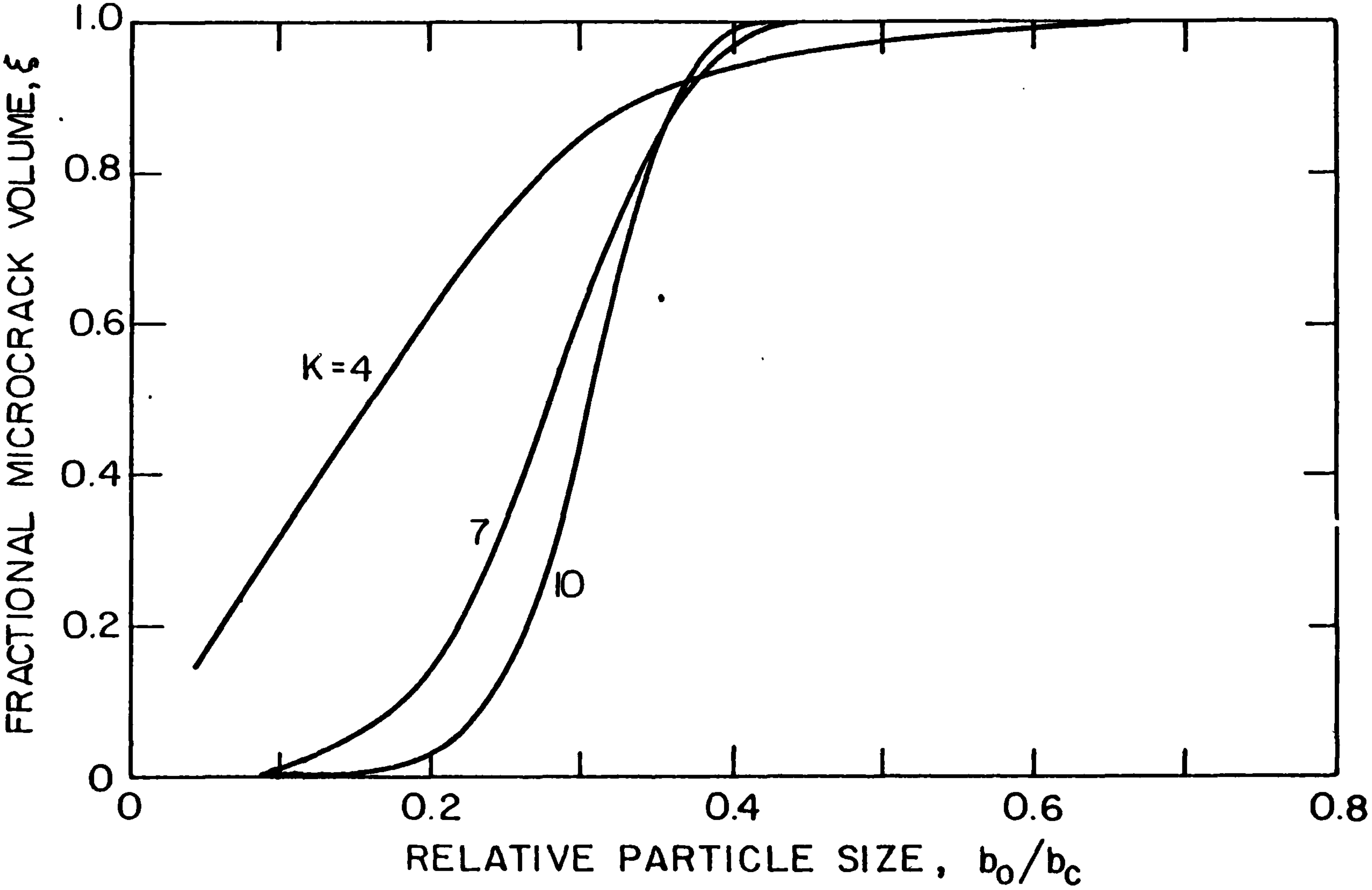

Fig. 6

XBL 809-5892

CHAPTER V

RESIDUAL STRESSES AND MICROCRACKING INDUCED BY THERMAL CONTRACTION INHOMOGENEITY

by

*A. G. Evans and **D. R. Clark

*Department of Materials Science and Mineral Engineering,
University of California,
Berkeley, CA 94720

**Structural Ceramics Group
Rockwell International Science Center
Thousand Oaks, CA 91360

RESIDUAL STRESSES AND MICROCRACKING INDUCED BY THERMAL CONTRACTION INHOMOGENEITY

A.G. Evans[*] and D. R. Clarke[†]

University of California, Berkeley[*] and
Rockwell International Science Center
Thousand Oaks, CA 91360[†]

ABSTRACT

Brittle materials are subject to microcrack formation at grain boundaries and at second phase particles. These cracks are induced by residual stress that results from incompatibilities in thermal contraction. The development of *residual stress and its partial relaxation by diffusion (at elevated* temperatures) are described. The evolution of microcracks within the residual stress fields are then examined. Particular attention is devoted to considerations of the critical microstructural dimension at the onset of microcracking.

INTRODUCTION

Many properties of ceramic materials depend on the incidence of microcracking. The most notable physical characteristics that exhibit a strong dependence on microcrack formation are certain mechanical (fracture toughness[1] and fracture strength[2]) and thermal (thermal diffusivity[3]) properties. The formation of stable microcracks is primarily related to localized residual stresses that develop because of thermal contraction mismatch or anisotropy (the former in multiphase materials[4] and the latter in single phase materials[5]). Significant progress has recently been achieved in the analysis of microcracking events by using a combination of stress analysis (based on the Eshelby concept) and fracture mechanics.[5,6,7] The intent of this paper is to examine the microcracking phenomenon in order to emphasize both the progress that has been achieved and the limitations of the available analyses.

One of the dominant characteristics of microcracking is its dependence on the scale of the microstructure. Typically, there is a "critical" microstructural dimension, ℓ_c, below which microcracking is not generally observed and above which a significant density of microcracks becomes evident.[4,8,9] The development of a capability for predicting ℓ_c is a primary objective of microcracking analyses. A critical comparison with measured values of ℓ_c is also a demanding test of the validity of such analyses.

The amplitude of residual stress fields produced by thermal contraction mismatch is independent of the scale of the microstructure. A criterion for microfracture based on the peak tension would not, therefore, yield a size dependence. This dilemma was first addressed by suggesting[8] that the onset of microfracture be dictated by an equality of the loss of strain energy and the increase in surface energy associated with the microfracture event. The former is a volume dependent term, and the latter is a surface area term; hence, a critical size emerges in a natural way. A reasonable correspondence with experimental observation was achieved by specifying the ratio of the final crack size to the dominant dimension of the microstructure. A conceptual difficulty with the approach arises because only the thermodynamics of the initial and final stages of the fracture event are considered; whereas, fracture is dictated by the rate of energy change at the critical condition for unstable crack extension.[5,9]

Subsequently, since size effects in brittle fracture often derive from statistical considerations,[10] a potential role of flaw statistics was suggested.[11] Notably, since fracture initiates from small inhomogeneities (pores, inclusions, etc.), the spatial and size distribution of these fracture initiating sites can influence the incidence of fracture. However, if the size distribution of these inhomogeneities is independent of the scale of the microstructure, the fracture probability for a constant volume fraction of the responsible microstructural phase would either be independent of size (volume distributed inhomogeneities)[12] or decrease with increase in size (interface distributed inhomogeneities).[13] A statistically based argument must, therefore, invoke inhomogeneities that increase in size as the microstructure enlarges. This effect is a plausible possibility, because inhomogeneities (such as pores) tend to increase in size during sintering, in direct proportion to the size of the grains[14] (or other microstructural entities). However, in the absence of well-substantiated distribution functions to describe the inhomogeneity size, the quantitative utility of the statistical approach is limited.

More recently, it has been recognized that a size effect can stem directly from considerations related either to the gradient of the residual stress field[5,6] or to stress relaxation.[7] For example, if the fracture initiating inhomogeneity is of sufficient size that it experiences an appreciable gradient of stress, then dimensional considerations demand that the fracture be size dependent. Specifically, the stress intensity factor, K, is given by[5]

$$K \sim \sqrt{a} \int_0^1 \sigma(x/\ell)\, F(x/a)\, d(x/a) \tag{1}$$

where a is the inhomogeneity size, σ is the stress and F(x/a) is the appropriate Green's function. Since the stress can always be expressed in the form

$$\sigma(x/\ell) = \hat{\sigma}\, \Omega(x/a,\ a/\ell) \tag{2}$$

where $\hat{\sigma}$ is the peak residual tension, the stress intensity factor can be written

$$\frac{K}{\hat{\sigma}\sqrt{\ell}} = \sqrt{\frac{a}{\ell}} \int_0^1 \Omega(x/a,\ a/\ell)\, F(x/a)\, d(x/a) \equiv \kappa(a/\ell) \tag{3}$$

where $\kappa(a/\ell)$ is the function determined by integration. Now, if the stress intensity factor is equated to its critical value for crack extension, K_c, Eq. (3) yields a "critical size" given by

$$\ell_c = \left(\frac{K_c}{\hat{\sigma}\, \kappa(a/\ell)}\right)^2 \tag{4}$$

An additional size influence derives from the diffusive stress relaxation that can occur at elevated temperatures.[15] The rate of relaxation will be more rapid in fine-grained materials, because of the enhanced diffusive fluxes. Smaller residual stresses will thus obtain and the tendency for microcrack formation will be reduced.

The considerations of microcracking developed in this paper relate primarily to the size effect that derives from residual stress gradients and relaxation phenomena. Beyond the scope of this review are the residual stresses[6,17] produced by phase transformations during cooling (as in the ZrO_2 based alloys) and the effect of externally applied stress fields on the residual stresses and the onset of microcracking.

RESIDUAL STRESSES

Residual stresses typically encountered in ceramic materials derive from differences in thermal contraction (anisotropy of the thermal expansion coefficient, α, for a single phase material, and contraction mismatch for multiphase systems). Thermal contraction differences are important because ceramics are fabricated at elevated temperatures (by hot pressing or sintering) and, during cooling, stress relaxation (by diffusion or viscous flow) becomes sufficiently inoperative below a temperature T_g that appreciable local stresses must develop from the contraction mismatch. The elastic stresses that evolve below T_g can be computed by using adaptations of the Eshelby approach.[16]

Several such calculations will be presented below. A more difficult problem to address is the definition of T_g; this is also examined in the following section.

Elastic Stresses

The stresses that develop below T_g, calculated by using the Eshelby approach, are illustrated for the anisotropic contraction of a hexagonal grain in Fig. 1. This method of calculation first extracts the microstructural entity (or entities) subject to shape deformation and its shape is then allowed to change (as characterized by the unconstrained transformation strain ε_{ij}^{T}). Subsequently, its shape is restored to the shape of the matrix cavity (by exerting a uniform stress) and it is then reinserted into the cavity. Finally, interface forces are applied (of equal magnitude, but opposite sign, to the restoring stress) to achieve continuity of stress. For isolated particles of ellipsoidal geometry this process yields a uniform stress within the particle; hence, stress analysis is relatively straightforward. More complex behavior is expected for other geometries, such as individual grains within a polycrystalline aggregate.

Multiphase Materials

The stresses within a spherical particle subject to transformation strains ε^T (hydrostatic) and $'\varepsilon^T{}_{ij}$ (deviatoric) are[16,17]

$$\sigma^I = - \frac{\varepsilon^T}{(1 + \nu_m)/2E_m + (1 - 2\nu_p)/E_p} \qquad (5a)$$

$${}'\sigma^I_{ij} = - \frac{{}'\varepsilon^T_{ij}}{(1 + \nu_p)/E_p + 2(1 + \nu_m)(4 - 5\nu_m)/E_m(7 - 5\nu_m)} \qquad (5b)$$

where σ^I is the hydrostatic stress and ${}'\sigma^I_{ij}$ is the deviatoric stress. The same hydrostatic stress level pertains for ellipsoidal particles, irrespective of their shape; but, the deviatoric stress is sensitive to the particle shape.[16] Two extremes are of interest. First, if the particles and matrix have isotropic thermal contraction coefficients, the resultant stress is exclusively hydrostatic; hence,

$$\sigma^I = - \frac{(\alpha_m - \alpha_p)\,(T_g - T)}{(1 + \nu_m)/2E_m + (1 - 2\nu_p)/E_p} \qquad (6)$$

where $\alpha_m - \alpha_p$ is the thermal contraction mismatch between matrix and particle, and T is the temperature. For a particle and matrix with similar elastic constants, Eq. (6) becomes

$$\sigma^I = - \frac{(\alpha_m - \alpha_p)\,(T_g - T)\,E}{3(1 - \nu)} \qquad (7)$$

Second, if the particle exhibits anisotropy of thermal expansion (e.g., α_1 and α_2), such that the average expansion matches that of the matrix, then the stress within the particle is purely deviatoric and is given by

$${}'\sigma^I_{ij} = - \frac{(\alpha_m - \alpha_2)\,(T_g - T)}{(1 + \nu_p)/E_p + 2(1 + \nu_m)(4 - 5\nu_m)/E_m(7 - 5\nu_m)} \qquad (8)$$

which for uniform elastic properties reduces to

$$\sigma_{ij}^{I} = - \frac{(7 - 5\nu)(\alpha_m - \alpha_2)(T_g - T)\,E}{15(1 - \nu^2)} \tag{9}$$

In general, therefore, the resultant stress, σ_{ij}, for uniform elastic constants is

$$\frac{\sigma_{ij}}{E(T_g - T)} = - \frac{(7 - 5\nu)(\alpha_m - \alpha_2)}{15(1 - \nu^2)} - \frac{(\alpha_m - \alpha_p)}{9(1 - \nu)}\,\delta_{ij} \tag{10}$$

The equivalent result for ellipsoidal geometry is

$$\frac{\sigma_{ij}}{E(T_g - T)} = - \frac{(\alpha_m - \alpha_p)}{9(1 - \nu)}\,\delta_{ij} - \frac{\gamma}{(1 + \nu)}\,(\alpha_m - \alpha_2) \tag{11}$$

where γ is a function of the particle shape.[16] For a needle, $\gamma = 1/2$; for a sphere, $\gamma = (7 - 5\nu)/15(1 - \nu)$; and for a disc, $\gamma = \pi(c/b)\ (2 - \nu)/4(1 - \nu)$, where c is the disc thickness and b is the disc radius.

The stresses within the matrix are more difficult to analyze and, with the exception of spherical[18] and cylindrical particles,[19-21] have not been computed exactly. Eshelby shows that if the harmonic and biharmonic potentials of the particle (however arbitrary its shape) are known, then the displacements in the matrix are related to the transformation strain $\varepsilon_{ij}{}^{T}$ in the particle by

$$u_i = \frac{\sigma_{jk}^{T}\ \Psi_{,ijk}}{16\pi\mu(1 - \nu)} - \frac{\sigma_{ik}^{T}\ \sigma_{,jk}}{4\pi\mu} \tag{12}$$

where σ_{jk}^T is the stress derived by Hooke's law from the strain ϵ_{ij}^T. The matrix stresses can then be obtained from the displacement derivatives. In the case of a spherical particle subject to hydrostatic strain, the matrix stresses are particularly simple,

$$\sigma_{rr} = \sigma(r_o/r)^3, \qquad \sigma_{\theta\theta} = -(\sigma/2)(r_o/r)^3 \tag{13}$$

where r_o is the particle radius and r is the distance from the particle center.

The harmonic and biharmonic potentials for a very long cylindrical particle (fiber) have recently been calculated[20] and may be used to compute the matrix stresses from Eq. (12):

$$\phi = 2\pi r_o^2 \ \ell n\ (r/r_o) \tag{14a}$$

$$\psi = \pi r_o^2(r^2 - r_o^2) - \pi r_o^2\ r^2 + r_o^2/2\ \ell n\ (r/r_o) \tag{14b}$$

For the case of thermal contraction mismatch between the fiber and matrix, described by a hydrostatic strain ϵ^T, the matrix stresses are

$$\begin{aligned} \sigma_{11}^c &= E\ \epsilon^T \frac{(3 - 2\nu)}{2(1 - \nu)}\ \frac{r_o^2(x^2 - y^2)}{r^4} \\ \sigma_{22}^c &= -\sigma_{11}^c \\ \sigma_{12}^c &= E\ \epsilon^T \frac{(3 - 2\nu)}{2(1 - \nu)}\ \frac{r_o^2\ xy}{r^4} \end{aligned} \tag{15}$$

A case of particular interest is that of the cylindrical particle exhibiting an anisotropy of thermal contraction in the plane perpendicular to the long axis of the cylinder such that the average contraction matches that of the matrix. The stresses generated within the matrix are of the form[21]

$$\sigma_{11}^{c} = \frac{E\,\epsilon_{11}^{T}}{(1+\nu)(1-2\nu)}\left[\frac{r_o^{2}\,(x^{2}-y^{2})}{r^{4}} + \frac{\nu}{1-\nu}\,\frac{(x^{4}-y^{4})}{r^{2}}\right]$$

$$+ \frac{E\,\epsilon_{11}^{T}}{4(1-\nu^{2})}\left[\frac{4r_o^{2}\,y^{2}(3x^{2}-y^{2})}{r^{6}} + \frac{3r_o^{2}\,(x^{4}+y^{4}-6x^{2}y^{2})}{r^{2}}\right] \qquad (16)$$

where

$$\epsilon_{11}^{T} = (\alpha_1 - \alpha_m)(T_g - T)$$

However, since the stresses immediately adjacent to the interface are of greatest interest for microfracture problems, some pertinent information can be obtained by deriving the stresses in the matrix just outside the inclusion. For an ellipsoidal inclusion subject to dilatation, the stresses in the matrix can be written quite generally as:[16]

$$\sigma_{ij}^{I} = \sigma^{I}(n_i n_j - 1/3\delta_{ij}) \qquad (17)$$

where n_{ij} are the normals to the ellipsoid surface. Particular values for the stresses at the particle matrix interface have been calculated for disc and needle shaped particles.[22] The stresses are a maximum near the termination of the major axis of the ellipsoid. However, as described earlier, the gradient in stress (in addition to the stress level at the particle interface) is of importance in dictating the size effect. As far as the authors are aware, the stress gradients around ellipsoidal particles subject to a transformation strain have not been calculated and remain a subject for further work.

Single Phase Materials

Grains in single phase materials exhibit relatively complex geometric configurations, and stress analysis is more complex than for the isolated ellipsoidal particle. However, some useful approximations can be obtained quite straightforwardly. The general level of residual stress within the grains can be obtained by simply requiring a grain to be contained within an isotropic matrix, with the average properties of the polycrystalline aggregate, and inserting the anisotropic contraction coefficients into Eq. (10). However, this simplification neglects the stress enhancing influence of grain junctions, an effect which has important consequences for microfracture.

Estimates of the stresses that develop in the vicinity of grain junctions can be obtained by adopting two-dimensional analogues, such as an array of hexagonal grains. The stresses that develop in such an array can be determined by firstly establishing the resultant body forces at each grain boundary facet (see Fig. 1). These body forces, p, generate non-uniform stresses that superimpose upon the uniform stresses developed during shape restoration. Of principal interest are the stresses at the grain boundaries, because these are the dominant sites for microfracture. The stresses at a site (x,z) inclined at an angle β to the boundary, (Fig. 2) are of the form[5]

$$\frac{4\pi\sigma_{xx}}{p\cos\beta} = \int_0^1 \frac{(z + \alpha\sin\beta)}{[\alpha^2 - 2\alpha(z\sin\beta - x\cos\beta) + (x^2 + z^2)]} \cdot \left\{(1 - \nu) - \frac{2(1 + \nu)(\alpha\cos\beta - x)^2}{[\alpha^2 + 2\alpha(z\sin\beta - x\cos\beta) + (x^2 + z^2)]}\right\} d\alpha \qquad (18)$$

Equation (18) should be used to obtain the stresses on boundary AB (Fig. 3) from the body forces of the four adjacent boundaries (AA', AA", BB', BB"). For more remote boundaries sufficient accuracy can be achieved by placing a single force at the grain facet center,[23] which represents the total body force on that boundary (Fig. 3). These stresses superimpose on a uniform stress (equal in magnitude to half the initial stress) which derives from the body forces on AB coupled with the initial stress.

The component of the stress from the four adjacent boundaries dominates the behavior in the vicinity of the grain junction. This stress component is of the form[5]

$$\frac{4\pi\sigma}{p\cos\beta} = A_1(\beta,\nu)\,\ell n\left[\frac{\ell^2 + x^2 + z^2 + 2\ell(z\sin\beta - x\cos\beta)}{x^2 + z^2}\right]$$
$$+ A_2(\beta,\nu,x,z)\cdot\tan^{-1}\left[\frac{2\ell + z\sin\beta - x\cos\beta}{2(z\cos\beta + x\sin\beta)}\right]$$
$$- \tan^{-1}\left[\frac{z\tan\beta - x}{2(z + x\tan\beta)}\right] + A_3(\ell,\beta,\nu,x,z) \qquad (19)$$

where A_1, A_2, and A_3 are relatively complex functions in the range ± 2π. The logarithmic term is singular at the grain junction and is thus the most influencial with regard to microcrack formation.[5]

The specific stress magnitudes that develop depend on the relative orientations of the grains circumventing the boundary of interest. Preliminary calculations have been conducted for the orientation that has been assumed to yield the maximum stress; this depicted in Fig. 4a, and the results are shown in Fig. 4b. Calculations for more general grain orientation relations are now in progress.[23] These results will provide a full perspective of residual stress distributions in polycrystalline aggregates in which there is a random distribution of contraction anisotropy orientations.

STRESS RELAXATION EFFECTS

Stress relaxation in ceramics occurs primarily by diffusion (or by viscous flow in the presence of an amorphous phase). These relaxation processes are usually motivated by local gradients in hydrostatic stress, and thus occur in response to localized thermal contraction stresses, while the material is at elevated temperatures.

Multiphase Materials

For isotropic multiphase materials, there is no gradient of hydrostatic stress within the isolated phase (Eq. 5). However, large shear stresses exist within the surrounding matrix (note that the hydrostatic stress is zero). The shear stresses within the matrix cause grain boundary sliding, and diffusive deformation will occur in response to local normal stresses induced by sliding.[24] The deformation field will be similar to that of a cavity subject to internal pressure. Initially, radial flow in the matrix will redistribute the residual stress. Reduction of the stresses will begin when the redistribution extends across the sample, following the onset of interaction between the stress fields around adjacent particles. The authors are not aware of solutions for this problem, although the analysis is relatively straightforward.

Polycrystalline Single Phase Aggregates

It has already been demonstrated that anisotropic thermal contraction in polycrystalline aggregates develops tensile or compressive stresses on grain boundaries. A gradient of chemical potential suitable for diffusive relaxation (Fig. 5) is thus established. The "initial" stress involves singularities near grain junctions (Fig. 4). But the singularities are weak (logarithmic) and should be rapidly dispersed by localized diffusive fluxes. The rate controlling relaxation process involves diffusion between adjacent grain facets (Fig. 5), such that atoms are removed from the boundaries subject to compression and are deposited on boundaries under tension. If it is assumed that the relaxation times are sufficiently rapid that atom deposition and removal occurs uniformly along the respective grain boundaries, a parabolic "steady-state" stress distribution must develop along the boundaries during the relaxation process. The extent of strain relaxation can then be deduced by using well-established mathematical procedures for diffusive flow. This mode of analysis is only permissable when the diffusivities are large, notably at the highest temperatures. The stress evolution at intermediate temperatures requires "transient" solutions involving more complex formulations. Such analyses have not yet been performed. Currently, therefore, it is only possible to obtain approximate solutions by permitting "steady-state" relaxation above a "freezing" temperature T_s and invoking fully elastic stress development below T_g.

The stress relaxation problem can be posed by first establishing the normal elastic displacement δ_1 of the boundaries during cooling (the driving force for the diffusive flow, Fig. 5) and the displacement relaxation δ_2 due to diffusion.

Then, the resultant displacement δ (= $\delta_1 - \delta_2$), which determines the level of the relaxed stress, can be derived. The solution for a constant cooling rate T will be presented.[25]

The elastic stress level on a grain boundary normal to the direction of maximum contraction is

$$\sigma_{xx} = \frac{\beta\, E(T_o - \dot{T}t)\Delta\alpha}{(1 + \nu)} \tag{20}$$

where T_o is the initial temperature, $\Delta\alpha$ is the deviation of the contraction coefficient from the average, and β is a coefficient that depends on the orientations of the adjacent grains. The corresponding elastic displacement is

$$\delta_1 = \frac{\sqrt{3}\ \ell\ \beta\ \dot{T}\ t\ \Delta\alpha}{2\ (1 + \nu)} \tag{21}$$

The relaxations of these displacements by diffusion are governed by the relation[26]

$$\frac{d^2\sigma(x,t)}{dx^2} = -\frac{kT\dot{\delta}_2(t)}{\Omega\ D_b\delta_b} \tag{22}$$

where $D_b\delta_b$ is the diffusion parameter, Ω the atomic volume and $\dot{\delta}$ is assumed to be uniform (as noted above). Integration of Eq. (22) gives the stress distribution

$$\sigma(x,t) = \frac{-\xi x^2}{2} + C_1x + C_2 \tag{23}$$

where $\xi = kT\dot{\delta}_2(t)/\Omega\ D_b\delta_b$ and C_1 and C_2 are the integration constants. The positions of zero flux ($d\sigma/dx = 0$) in the system are at the grain facet center 0 and at the grain junction J (Fig. 5). Hence, since the flux must be continuous at the grain corner A, the constant C_1 must be equal to $\xi\ell/2$. If σ_o is the stress at A, the stress distribution becomes

$$\sigma(x,t) = -\frac{\xi x^2}{2} + \frac{\xi x\ell}{2} + \sigma_o \tag{24}$$

The equivalent average stress is

$$\langle\sigma\rangle(t) = \frac{\xi \ell^2}{12} + \sigma_0 \qquad (25)$$

Volume conservation requires that the volume of material deposited on the tensile boundary must equal the volume removed from the compressed boundary. The stress at the grain corner thus becomes

$$\sigma_0 = \xi \ell^2/12 \qquad (26)$$

and the average stress reduces to

$$\langle\sigma\rangle(t) = \frac{kT\ell^2 \, \dot{\delta}_2}{6\Omega D_b \delta_b} \qquad (27)$$

The average stress on each boundary must also be related to the resultant displacement of the grain:

$$\frac{\sqrt{3}\,\ell}{2E} \frac{d\langle\sigma\rangle}{dt} = \dot{\delta}_1 - \dot{\delta}_2 \qquad (28)$$

Substituting $\dot{\delta}_1$ from Eq. (21) and $\dot{\delta}_2$ from Eq. (27), and noting that D_b is temperature dependent

$$D_b = D_o \, e^{-Q/kT} \qquad (29)$$

where Q is the activation energy for boundary diffusion, the following differential equation obtains

$$\frac{d\langle\sigma\rangle}{dT} - \frac{12\Omega\delta_b D_o E}{\sqrt{3}k\ell^3 \, \dot{T}} \, \frac{e^{-Q/kT}}{T} \langle\sigma\rangle = - \frac{\beta E \Delta\alpha}{(1 + \nu)} \qquad (30)$$

The solution to this equation must be conducted numerically. However, an approximate series expansion may be derived[25] for comparison with the elastic result expressed in terms of a "freezing" temperature T_g:

$$\frac{\langle\sigma\rangle(1 + \nu)}{\beta \; E \; \Delta\alpha} = T_g - T$$

From this, T_g is given approximately by

$$T_g \sim \frac{Q/k}{\ell n[12\Omega \; D_o \delta_b E/\sqrt{3} n k \ell^3 \; \dot{T}]} \tag{31}$$

The trends in T_g with the influential variables are immediately apparent. In particular, T_g increases as the grain size and cooling rate increase and as the diffusivity and modulus decrease. This behavior is exemplified for Al_2O_3 ($D_o\delta_b$ = 10^{-9} m^3 s^{-1}, Q = 100 kcal/mole, $\Omega \sim 10^{-29}$ m^3, n = 30, E = 420 GN m^2), for which:

$$T_g = \frac{50{,}000}{29.5 - \ell n \; \ell^3 \; \dot{T}}$$

where ℓ is in microns, T in K s^{-1} and T_g is in K. Specifically, for ℓ = 1 μm and T = 1K s^{-1}, T_g = 1695K; whereas for ℓ = 10 μm and T = 1K s^{-1}, T_g = 2210K.

MICROCRACK FORMATION

The formation of microcracks at grain boundaries or at second phase particles has been considered to depend on the existence of a distribution of small inhomogeneities that pre-exist at the boundaries (especially at three grain junctions) or interfaces.[5,6,7] These inhomogeneities have been proposed because the stress intensification levels associated with the residual stress fields do not appear to be of sufficient magnitude to induce fracture in defect free material (although further study is needed to establish whether this possibility can be discounted). The role of the proposed inhomogeneities is to further enhance the stress intensification to a level suitable for microcrack evolution. It is certainly reasonable to presume that inhomogeneities do exist at boundaries or interfaces in ceramics, e.g., small pores remaining at grain triple points. However, little effort has yet been devoted to the elucidation of the inhomogeneities that induce microfracture in specific miocrostructural situations. It is thus generally assumed that the inhomogeneities exhibit the stress concentrating properties of small microcracks: a presumption that is evidently an over-simplification. Thereafter, stress intensity factors can be calculated (from the residual stress levels) and compared with the critical values for grain boundary separation. Approximate stress intensity factors are conveniently calculated with a superposition method, based on the prior stress field.[5,6] A typical example, illustrated in Fig. 6, is where a microcrack develops along two symmetrically stressed grain facets, initiating at the common triple junction. The stress intensity factor for such a crack is given by

$$\frac{K(1 + \nu)}{E\Delta\alpha\Delta T\sqrt{\ell}} = \kappa(a/\ell) \qquad (32)$$

where $\kappa(a/\ell)$ is the function plotted in Fig. 6. It is noted that the stress intensity factor exhibits a maximum, $\hat{K}$. This is typical of crack extension in residual or spatially varying stress fields. The principal maximum in the present analysis essentially coincides with a crack front located at the first triple junction, where the residual stress changes sign (i.e., the residual stress becomes compressive along the impinging boundaries). Equating K to the boundary separation resistance, K_c^b, yields an absolute minimum condition for the formation of microcracks. This corresponds to an upper bound for the critical grain facet size;

$$\hat{\ell}_c = \left[\frac{K_c^b\,(1 + \nu)}{\hat{\kappa}\,E\Delta\alpha\Delta T}\right]^2 \qquad (33)$$

where $\hat{\kappa}$ is the magnitude of the normalized stress intensity factor at the maximum. Estimates of specific values of the grain facet sizes that induce microcracking involve statistical considerations based on flaw distributions.

More exact calculations of the stress intensity factor can be obtained by using numerical (finite element or finite difference) methods. A recent example[7] is the use of a finite difference scheme for calculating the stress intensity factor for a crack at the interface of a spherical second phase particle. A convenient use of the finite difference method involves the calculation of the strain energy, U, as a function of crack length, a. The stress intensity factor is then deduced from the crack length derivative of the strain energy. A maximum value, $\hat{K}$, is obtained. The corresponding absolute minimum requirement for microcrack initiation is

$$\hat{R}_c = \frac{1.2(K_c^I/\langle\sigma\rangle)^2}{(1 - \nu)} \tag{34}$$

where K_c^I is the resistance of the interface to fracture and $\langle\sigma\rangle$ is the stress in the uncracked particle.

Further progress in the elucidation of microfracture is achieved by incorporating defects that reduce the critical size below the upper bound values. Little progress has yet been achieved in selecting appropriate defects and defect size distributions; although results could clearly be obtained by selecting arbitrary distributions (such as one of the extreme value distributions). Careful obsevations coupled with pertinent stress intensity factor calculations are needed to establish a more fundamental appreciation of microcracking. Comparison of the available calculations of K with experimental observations of microcracking suggest[5,6,7] that triple point defects in the size range, $0.1 < 2a/\ell < 0.3$, are typically involved in the microcrack initiation process. However, more direct observations and further calculations are needed to substantiate and refine this result.

CONCLUSION

This paper has described methods for calculating the residual stresses that develop at the microstructural level because of thermal contraction inhomogeneity. The stresses are typified by locally large amplitudes (with some singularities) and rapid gradients. These characteristics are central to the onset of microcracking, both microcrack initiation and arrest.

The stress level is also shown to depend on the rate of stress relaxation at elevated temperatures, by diffusion or viscous flow. The relaxation rate is a strong function of microstructure: rapid relaxation rates obtain in fine grained materials or in materials containing an amorphous boundary phase. These relaxation effects have been demonstrated to be manifest in an effective freezing temperature, a temperature at which elastic residual stresses begin to develop.

The onset of microcracking within the residual stress field has been considered to depend on the presence of small microstructural inhomogeneities (such as voids) at the susceptible interfaces. These features certainly exist, but have not yet been uniquely correlated with the onset of microcracking. By treating these pre-existent inhomogeneities as crack-like entities, stress intensity factors have been calculated. The level and variation in stress intensity factors indicate the potential for microcrack initiation and arrest at grain boundaries and interfaces.

In particular, a lower bound for the critical microstructural size needed to initiate microcracks has been identified (no microcracks can be observed at size levels below this bound). The actual formation of microcracks above the lower bound depends on the statistical characteristics (size and spatial) of the pre-existent inhomogeneities. This issue has not been addressed.

ACKNOWLEDGEMENT

The authors wish to thank the Office of Naval Research under Contract N-0014-79-C-0159. (AGE) and the Rockwell International Independent Research and Development Program (DRC) for their financial support, and the U.S. Department of Energy under Contract W-7405-ENG-48.

REFERENCES

1. R.G. Hoagland, G.T. Hahn and A.R. Rosenfield, Rock Mechanics 5, 77 (1973).

2. F.A. McClintock and H.J. Mayson, ASME Applied Mechanics Conf. (June 1976).

3. H.J. Siebenbeck, D.P.H. Hasselman, J.J. Cleveland and R.C.Bradt, Jnl. Amer. Ceram. Soc. 59, 241 (1976).

4. F.F. Lange, Fracture Mechanics of Ceramics (Ed. R.C. Bradt, D.P.H. Hasselman and F.F. Lange) Plenum, N.Y. Vol. 4 (1977).

5. A.G. Evans, Acta Met. 26, 1845 (1978).

6. D.R. Clarke, Acta Met., in Press.

7. Y.M. Ito, M. Rosenblatt, L.Y. Cheng, F.F. Lange and A.G. Evans, Int. J. Fract. (In Press).

8. R.W. Davidge and G. Tappin, Jnl. Mater. Sci 3, 297 (1968).

9. J.A. Kuszyk and R.C. Bradt, Jnl. Amer. Ceram. Soc. 56, 420 (1973).

10. W. Weibull, Ingenioers Vetenskaps Akad., 151, (1939).

11. A.G. Evans, Jnl. Mater. Sci., 9, 210 (1974).

12. O. Vardar, I. Finnie, D.S. Biswas and R.M. Fulrath, Intl. Jnl. Frac. 13, 215 (1977).

13. A.G. Evans, D.S. Biswas and R.M. Fulrath, Jnl. Amer. Ceram. Soc. 62, 95 (1979)

14. W.D. Kingery and B. Francois, in "Sintering and Related Phenomena," edited

G.C. Kuczynski, Gordon and Breach, 1967.

15. J.E. Blendell, R.L. Coble and R.J. Charles, in "Ceramic Microstructure '76," edited R.M. Fulrath and J.A. Pask, Westview Press, Boulder, 1977.

16. J.D. Eshelby, Proc. Roy. Soc., A241, 376 (1957).

17. A.G. Evans and A.H. Heuer, Jnl. Amer. Ceram. Soc. 63, (May/June 1980), to be published.

18. J. Selsing, Jnl. Amer. Ceram. Soc., 44, 419 (1961).

19. L.M. Brown and D.R. Clarke, Acta. Met. 25, 563 (1977).

20. D.R. Clarke, PhD Thesis, University of Cambridge (1974)

21. D.R. Clarke to be published.

22. G.C. Weatherly, Phil. Mag. 17, 791 (1968).

23. Y. Fu and A.G. Evans, to be published.

24. R. Raj and M.F. Ashby, Acta Met. 23, 653 (1975).

25. D.R. Clarke and A.G. Evans, to be published.

26. A.G. Evans and A.S. Rana, Acta Met., 28, 129 (1980).

27. R.M. Cannon and R.L. Coble, Deformation of Ceramics (Ed., R.E. Tressler and R.C. Bradt), Plenum, N.Y. (1975) p. 61.

FIGURE CAPTIONS

Fig. 1 A schematic indicating the Eshelby method for calculating the residual stresses and strains generated by anisotropic thermal expansion of an hexagonal grain.

Fig. 2 The linear boundary segment used to compute the relaxation stresses, showing the coordinate system (x, z).

Fig. 3 An hexagonal grain array showing the body forces used to calculate the stress at the central facet AB.

Fig. 4 The grain configuration that yields large values of the residual stress at facet AA' and the stresses calculated to exist along that facet.

Fig. 5 The elastic and diffusion displacement that occurs during cooling, indicating the direction of the diffusive flux. Also shown are the stresses that develop during steady-state diffusive flow.

Fig. 6 The variation of the normalized stress intensity factor with crack length for the grain, crack configuration indicated on the inset.

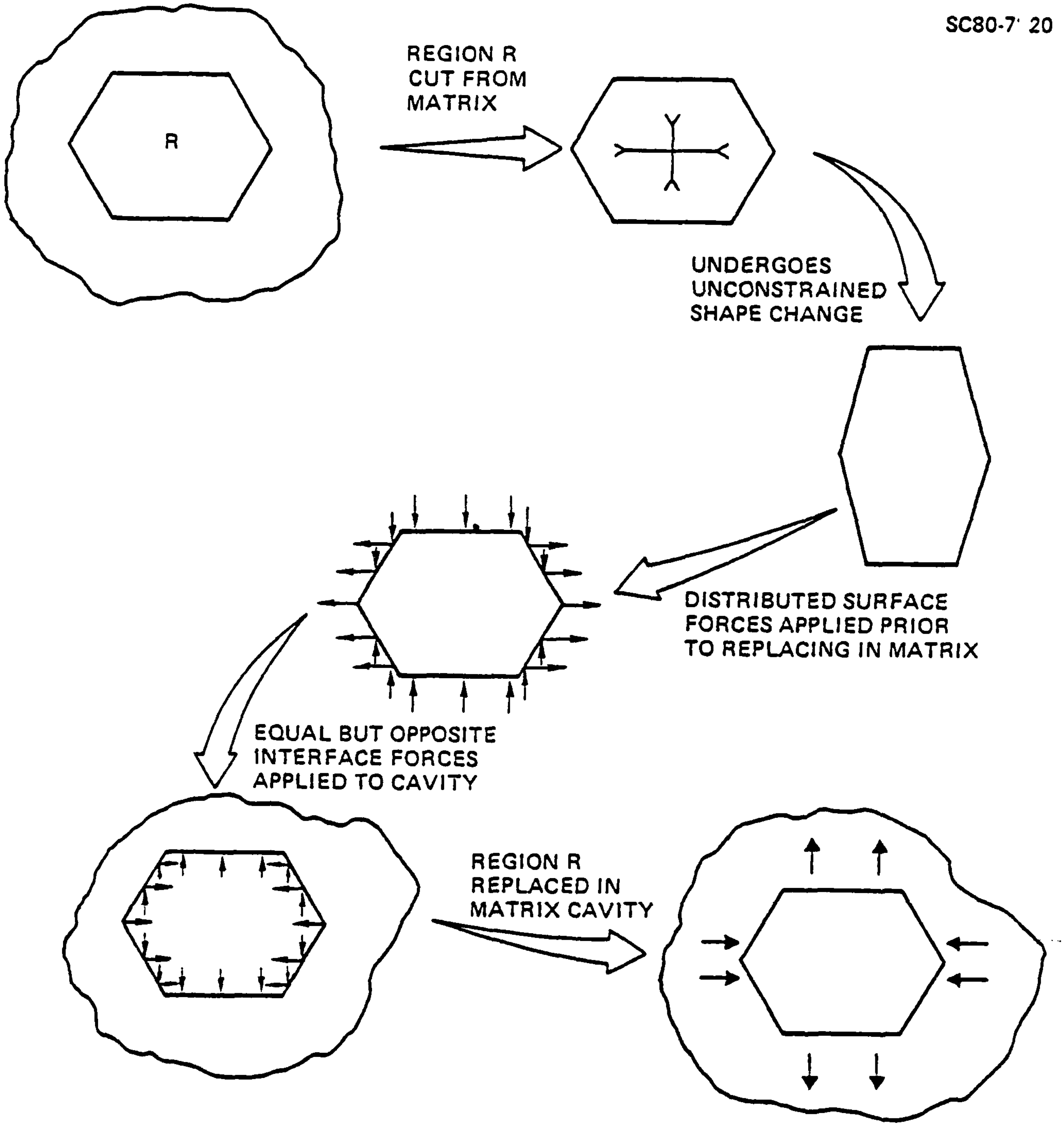
SC80-7120
R
REGION R
CUT FROM
MATRIX
UNDERGOES
UNCONSTRAINED
SHAPE CHANGE
DISTRIBUTED SURFACE
FORCES APPLIED PRIOR
TO REPLACING IN MATRIX
EQUAL BUT OPPOSITE
INTERFACE FORCES
APPLIED TO CAVITY
REGION R
REPLACED IN
MATRIX CAVITY

Fig. 1

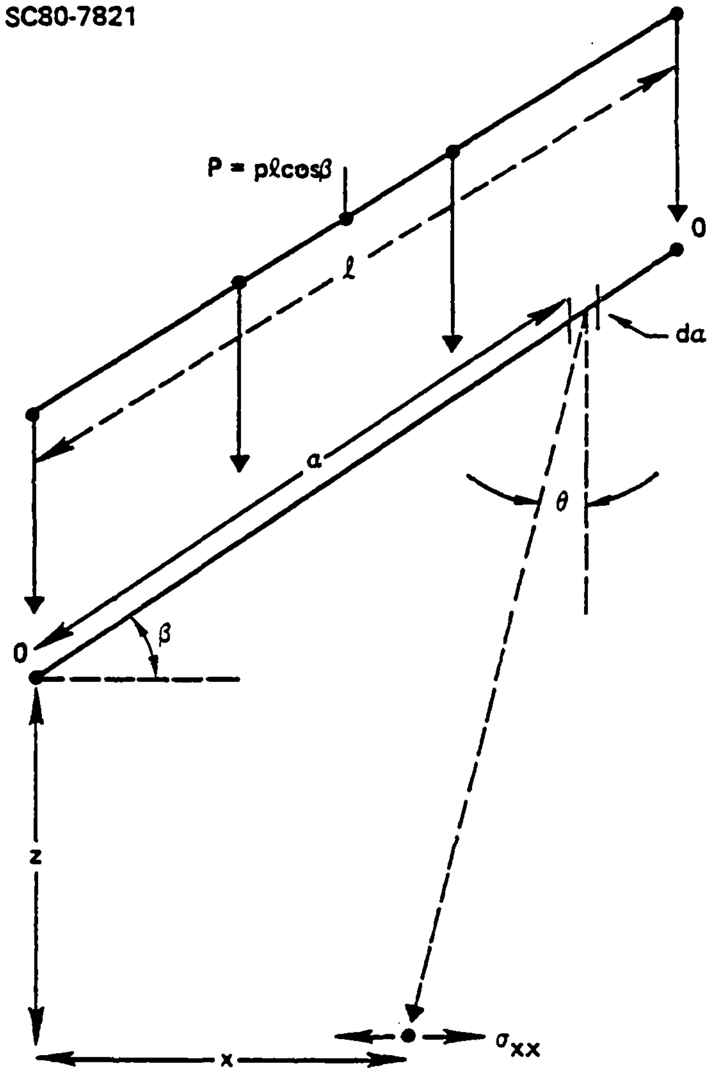
SC80-7821
P = pℓcosβ
0
ℓ
dα
α
θ
β
0
z
x
σxx

Fig. 2

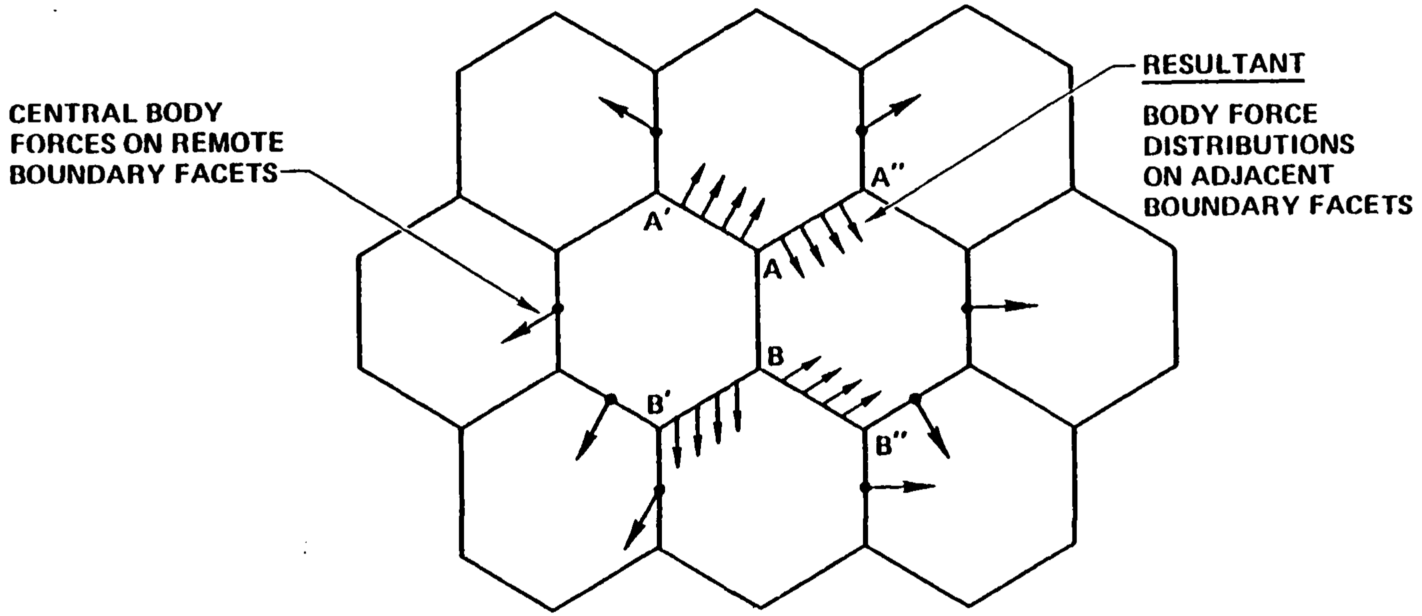
CENTRAL BODY
FORCES ON REMOTE
BOUNDARY FACETS
RESULTANT
BODY FORCE
DISTRIBUTIONS
ON ADJACENT
BOUNDARY FACETS
A'
A
A''
B'
B
B''

Fig. 3

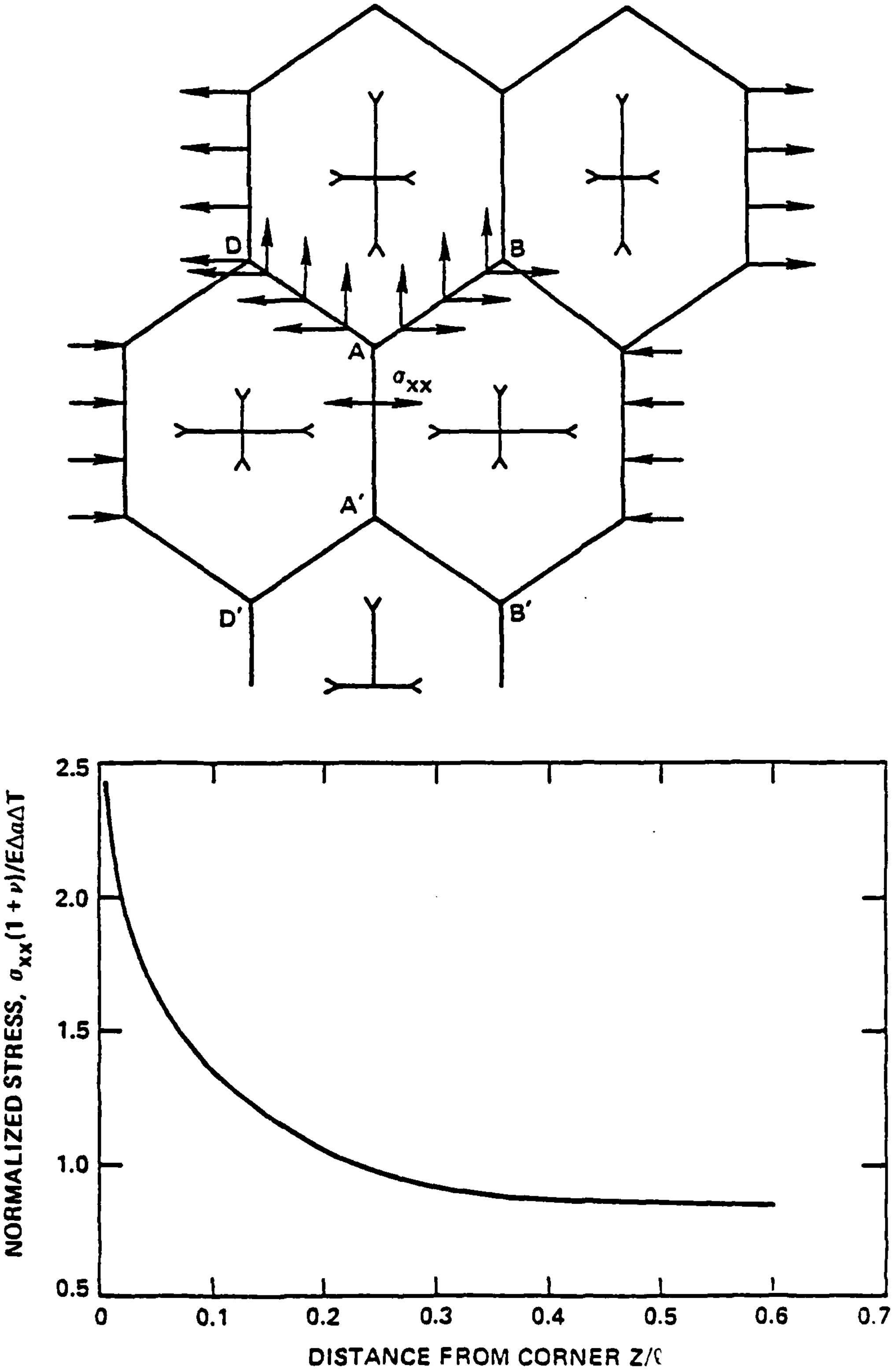
D
B
A
σ_{xx}
A'
D'
B'
NORMALIZED STRESS, $\sigma_{xx}(1+\nu)/E\Delta\alpha\Delta T$
2.5
2.0
1.5
1.0
0.5
0
0.1
0.2
0.3
0.4
0.5
0.6
0.7
DISTANCE FROM CORNER Z/ℓ

Fig. 4

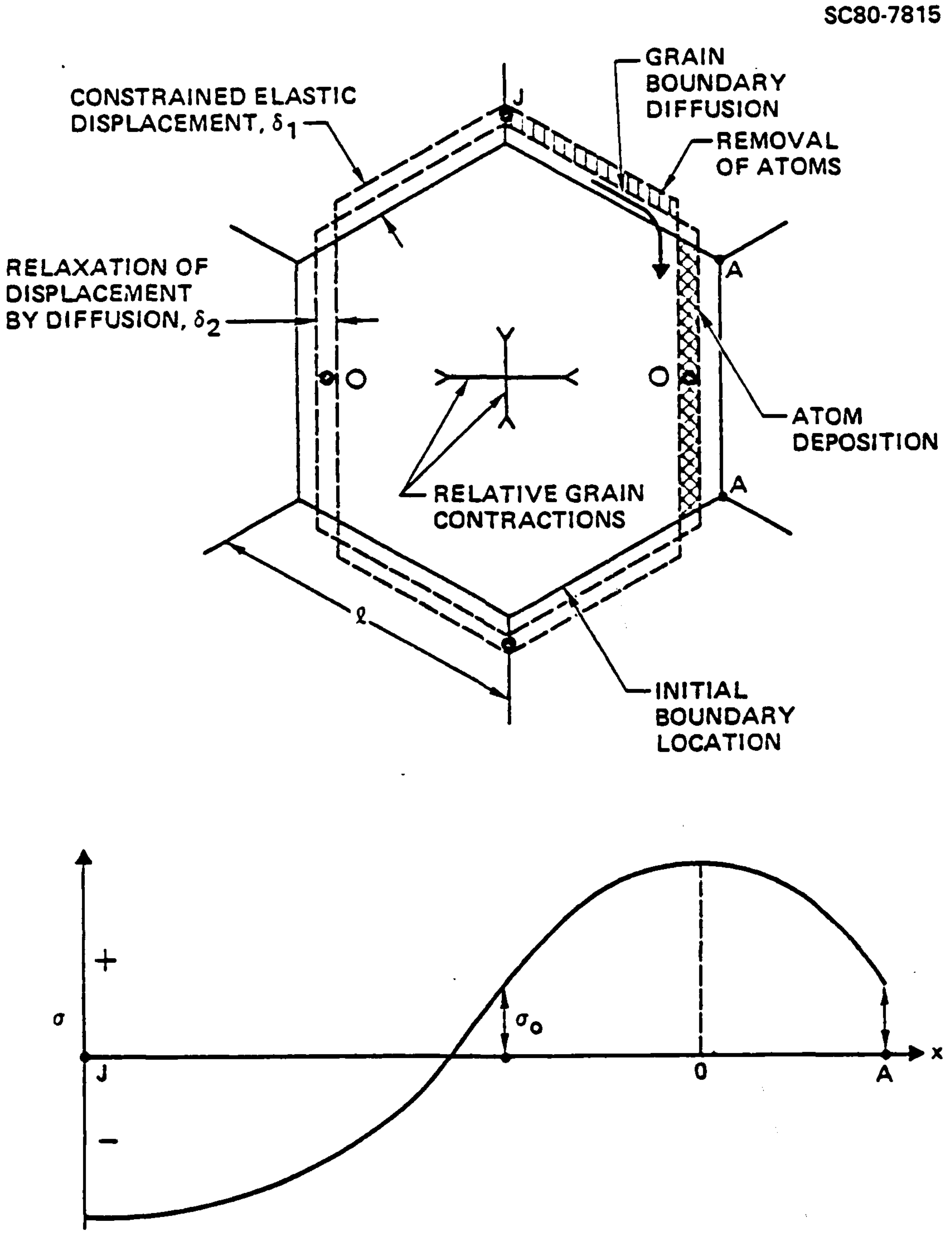
SC80-7815
GRAIN BOUNDARY DIFFUSION
CONSTRAINED ELASTIC DISPLACEMENT, δ_1
REMOVAL OF ATOMS
J
A
RELAXATION OF DISPLACEMENT BY DIFFUSION, δ_2
O
O
ATOM DEPOSITION
A
RELATIVE GRAIN CONTRACTIONS
ℓ
INITIAL BOUNDARY LOCATION
+
σ
σ_o
−
J
0
A
x

Fig. 5

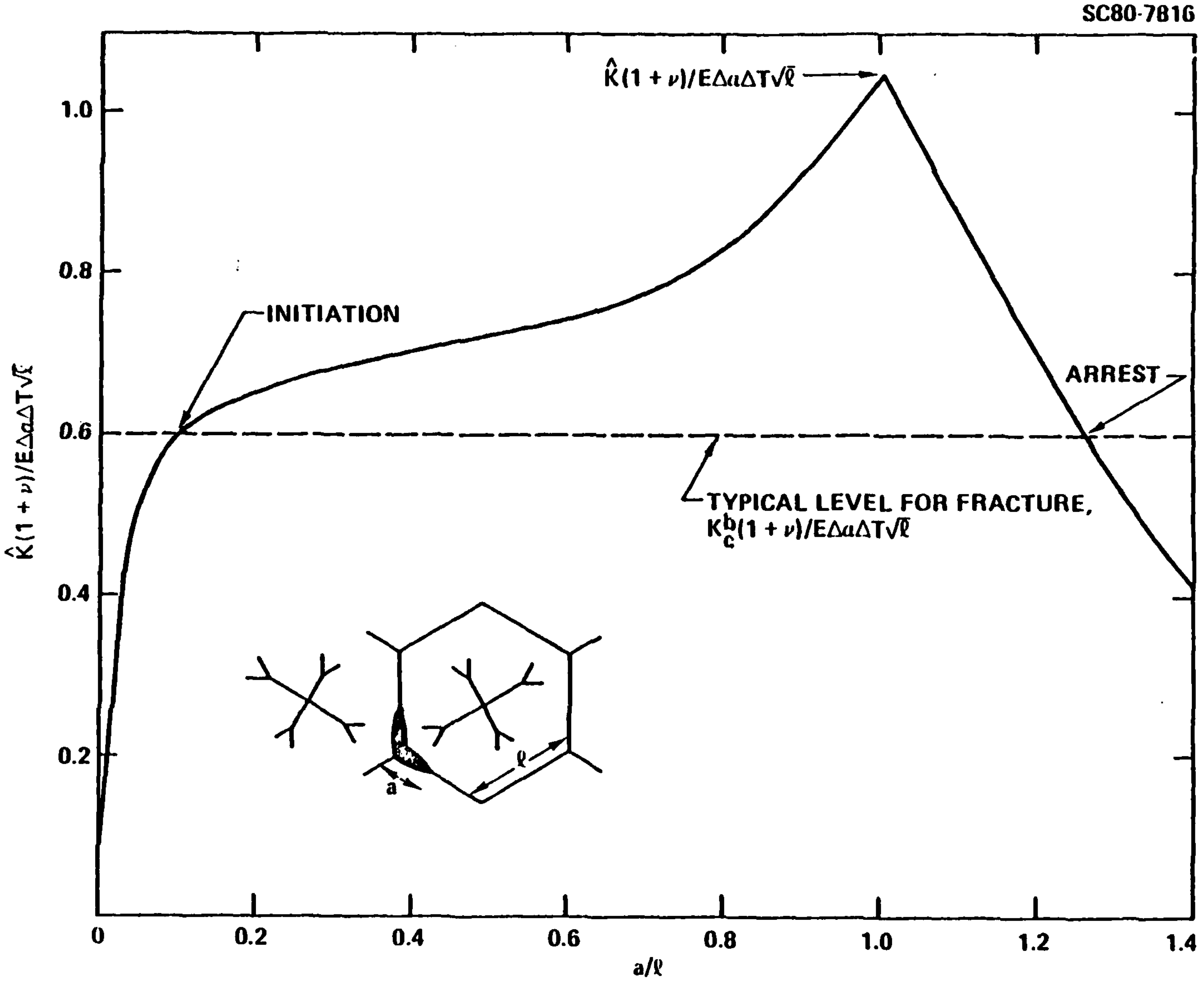
SC80-7816
$\hat{K}(1+\nu)/E\Delta\alpha\Delta T\sqrt{\ell}$
INITIATION
ARREST
TYPICAL LEVEL FOR FRACTURE,
$K_c^b(1+\nu)/E\Delta\alpha\Delta T\sqrt{\ell}$
$\hat{K}(1+\nu)/E\Delta\alpha\Delta T\sqrt{\ell}$
1.0
0.8
0.6
0.4
0.2
0
0.2
0.4
0.6
0.8
1.0
1.2
1.4
a/ℓ
ℓ
a

Fig. 6

CHAPTER VI

A SIMPLE METHOD FOR ADHESION MEASUREMENTS

by

S. S. Chiang, D. B. Marshall and A. G. Evans

Department of Materials Science and Mineral Engineering,
University of California
Berkeley, CA 94720

A SIMPLE METHOD FOR ADHESION MEASUREMENTS

S. S. Chiang, D. B. Marshall and A. G. Evans

Materials and Molecular Research Division,
Lawrence Berkeley Laboratory and Department of
Materials Science and Mineral Engineering,
University of California, Berkeley, CA 94720

ABSTRACT

An indentation method for determining the adhesion of interfaces between thin films and substrates has been developed. The method provides a quantitative measure of the interface fracture resistance and has the advantage of simplicity and reproducibility. The method has been demonstrated for a range of ZnO/Si systems and the adherence has been correlated with acoustic properties.

INTRODUCTION

The quantification of adhesion between films (or coatings) and substrates is an important but inadequately resolved problem. A meaningful method for measuring adhesion is needed both for quality control and for the development of improved film properties (e.g. monitoring variations of adhesion with different treatments and fabrication methods). This need has become increasingly important with the recent expansion in the use of thin film substrates in the electronics industry.

Ideally, the requirements of an adhesion test are: quantitative interpretation, applicability to a wide range of film thickness and film/substrate combinations, economy (minimal material use and machining requirements), reliability, sensitivity, and adaptability to routine testing. Despite many attempts to develop techniques for adhesion measurement[1-8], an entirely adequate quantitative test has not yet emerged. The objective of the present study is to develop an adhesion test, based on indentation fracture procedures, tha' satisfy these criteria.

Adhesion tests based on fracture mechanics principles are the most likely source o: quantitative procedures. Fracture mechanics methods exhibit several attractions. Firstly, an ahesion parameter, such as the interface fracture resistance (or toughness) K_c^{inter} can be defined. Secondly, the potential exists for developing sound, theoretically based, measurements of interface toughness. Finally, fracture mechanics provides a mathematical framework for using the fracture toughness as a design parameter. However, currently available tests[9,10] are of restricted application and are too complex for most purposes.

The test method proposed in this paper involves the introduction of a mechanically stable crack into the interface, by employing conventional indentation procedures. The resistance to propogation of the crack along the interface is then used as a measure of adhesion. Analysis of the results is based on recently developed indentation fracture mechanics[11,12]. The test is demonstrated to yield a sensitive measure of interface toughness. Also, by virtue of its inherent simplicity, and small scale, it appears to meet most of the requirements for a widely applicable adhesion measurement technique.

INDENTATION FRACTURE

The "well developed" deformation/fracture pattern which results from indentation of the surface of a homogeneous brittle solid with a Vickers pyramid is shown schematically in figure 1. The elastic/plastic nature of the deformation response is characterised by the plastically deformed zone (with a residual hardness impression) surrounded by cracks. Two distinct crack systems are apparent; the "median/radial" system comprising two orthogonal, semi-circular cracks parallel to both the load axis and an indentation diagonal, and the penny-shaped "lateral" crack parallel to the surface and centered near the base of the plastic deformation zone. Both crack systems develop mainly during the unloading half cycle and are driven primarily by the residual elastic/plastic stress field.

Recent analysis of these crack systems has provided understanding of the behavior of flaws in brittle surfaces, and enabled development of predictive models for material degradation processes. The radial/median crack system is pertinent to strength degradation (static contact[13,14], particle impact[15,16], machining damage[17]) and the lateral crack system to material removal processes (erosion and wear[18,19]). In addition, the derivation of the functional dependence of the radial crack dimension or the pertinent parameters (contact load P , material hardness H , elastic

8½ x 9⅞

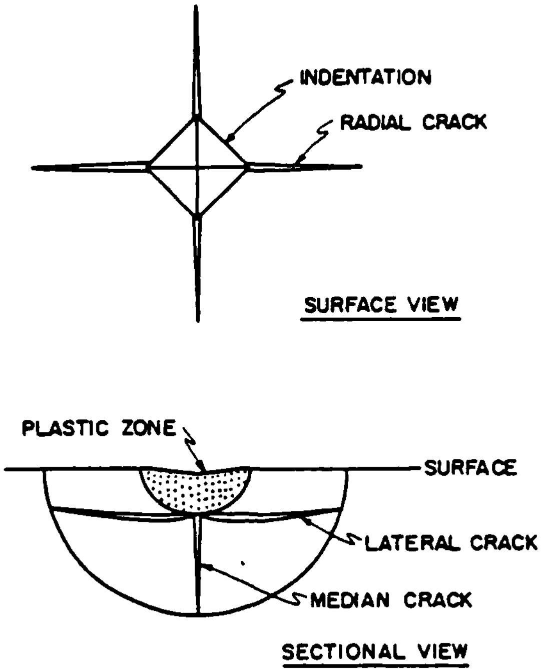

XBL8010-6085

Fig. 1. A schematic showing crack patterns generated by Vickers indentation in a homogenous material. a) Four radial cracks propagating along the indentation diagonal direction. b) Sectional view of the indentation; the dotted region represents the plastic zone created by indentation. The median crack coalesces with the radial crack to form a half-penny shaped crack. Lateral cracks propagate parallel to the surface.

modulus E , and toughness K_c) has led to a simple and efficient technique of toughness measurement[20,21]. The method has been extended to measure the interface toughness of very thick coatings by sectioning normal to the interface and aligning the indentation such that one radial crack propagates along the interface[22]. However the method cannot be applied to thin coatings (less than $\sim$1 mm) because of free surface effects on the crack propagation.

A more suitable basis for the present film adhesion measurements is provided by the lateral crack system. The film surface parallel to the interface is indented, and the lateral crack is induced to propagate along the interface (figure 2). Then measurements of the crack radius c , the indentation load P , the indentational angle 2a , and the film thickness h , will be demonstrated to provide a measure of the toughness K_c^{inter} . Lateral

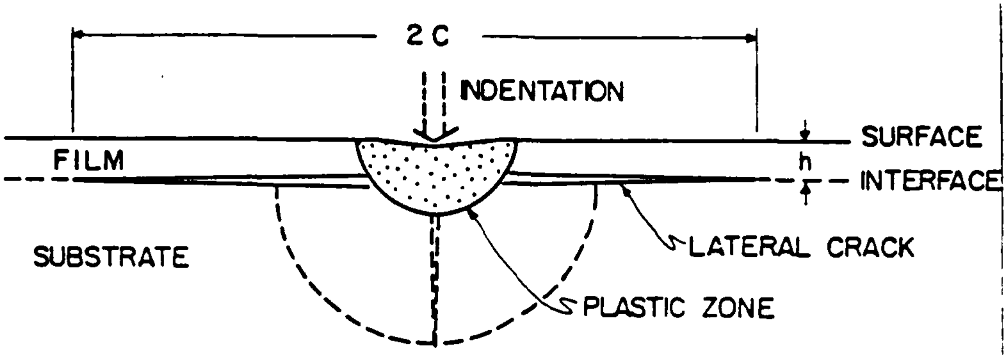

Fig. 2. A schematic of an Indentation made on a film/substrate sample. The lateral crack propagates preferentially along the interface.

cracks in a homogeneous material usually, but not always, form near the base of the plastic zone. However, the driving force for lateral crack propagation exists over a range of depths and the actual depth at which a crack propagates is influenced by the availability of crack nucleation sites[23]. The proposed test is based on the rationale that an interface (in the vicinity of the plastic zone) with a lower toughness than that of either the film material or the substrate material will be the preferred site for lateral crack formation. When fracture cannot be induced at the interface (but occurs in the film or substrate) it can be immediately concluded that the interface toughness is at least as large as that of the weaker material constituent.

The present study is confined to combinations of ZnO on Si and Si on Si because the materials have similar values of both hardness and elastic modulus (the parameters that dictate the magnitude of the residual stress which provides the crack driving force). This choice simplifies the theoretical analysis and permits direct correlation between theory and experiment. The effects of a mismatch in hardness and/or elastic modulus will be addressed in a subsequent analysis.

EXPERIMENTAL OBSERVATIONS

The viability of the indentation technique for measuring adhesion was firstly established by examining the influence of a subsurface interface on the development of lateral fractures. This was achieved by comparing lateral cracks obtained in a Si single crystal with those that develop at the interface between a 2 μm polycrystalline Si film deposited onto single crystal Si (fig. 3). A circular sub-surface lateral crack, located at the interface, was clearly evident in the latter, while a smaller, less distinct lateral crack developed in the single crystal. These observations indicate that interfaces are preferred sites for the lateral fracture process, thereby satisfying the basic prerequisite for applying the indentation technique to the adhesion problem. All subsequent experiments were conducted on ZnO/Si systems.

It can be anticipated from previous work[12,18,23] in indentation fracture that the radius of the lateral crack will depend on the indentation load and the film thickness (i.e. the crack location) in addition to the interface toughness (the parameter of interest). A typical influence of the load on the crack length is illustrated for ZnO/Si in fig. 4. Quantitative application of the indentation method will require determination of the functional dependence of the crack length on each of these variables. This issue will be addressed in section 4. At this jucture, some important trends in adhesion are established. This is achieved by comparing crack lengths for the same load and film thickness

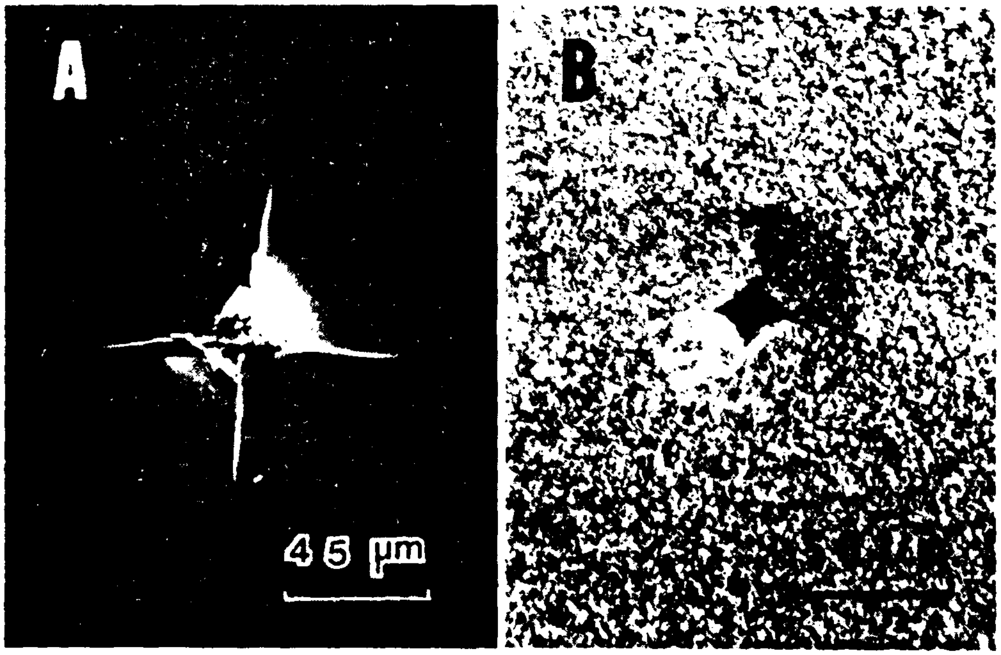

Fig. 3. Optical micrographs of indentation on Si. A) An Indentation made on single crystal (111) Si surface, indicating four radial cracks, and B) an Indentation made on thin film specimen, 2μm poly Si/500A SiO$_2$/(111)Si. A circular sub-surface lateral crack, located at the interface, can be seen using an interference contrast method.

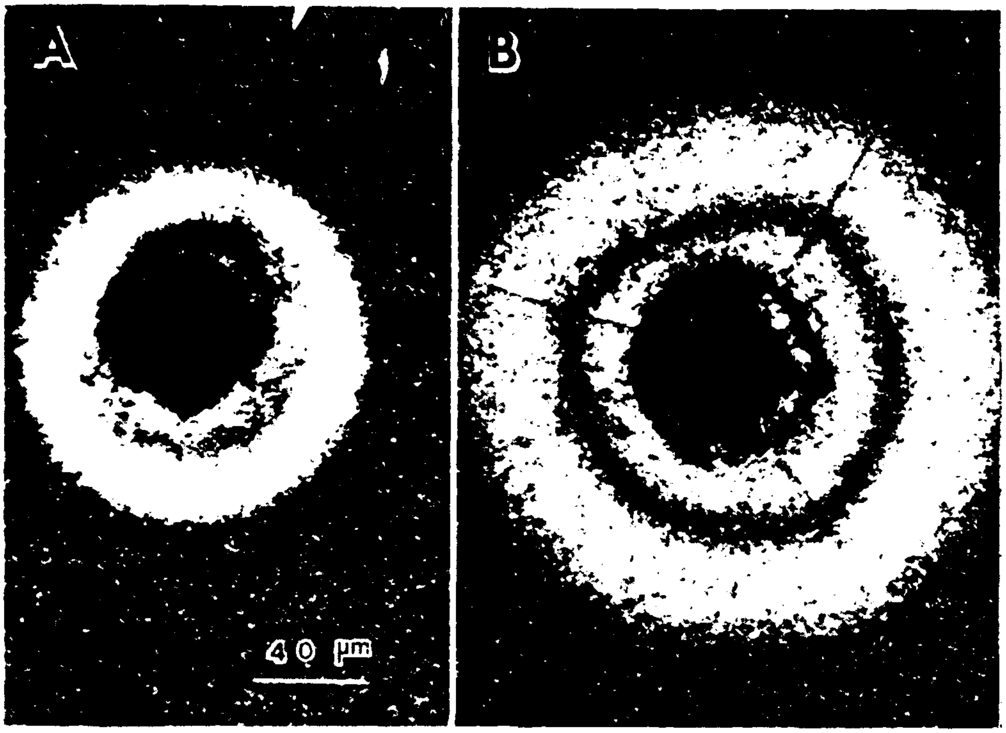

Fig. 4. Optical micrographs illustrating the effect of the indentation load on the lateral crack length for a ZnO/Si system. A) 5 N and B) 10 N.

obtained on indented samples of ZnO/Si, prepared under different conditions. In some instances, the adhesion trends are correlated with other property measurements, in order to demonstrate the general utility of indentation as a reproducible, comparitive method for determining adhesion.

The indentation results obtained at 300 g. for the following two systems, 6 μm ZnO/1000Å SiO_2/(111)Si-N type and 6 μm ZnO/1500Å Pt/500Å Ti/(111) Si-N type, are illustrated in fig. 5. It is noted that faceted lateral cracks develop in latter, indicating the existence of preferred paths of fracture resistance (typical of lattice orientation effects in single crystals), and that the average crack radius for this system is smaller. Superior adhesion thus obtains for the system with the Pt/Ti interlayer†.

† It should not be concluded that the Pt/Ti interlayer invariably provides superior adhesion. Other film formation parameters are of substantial importance with regard to adhesion.

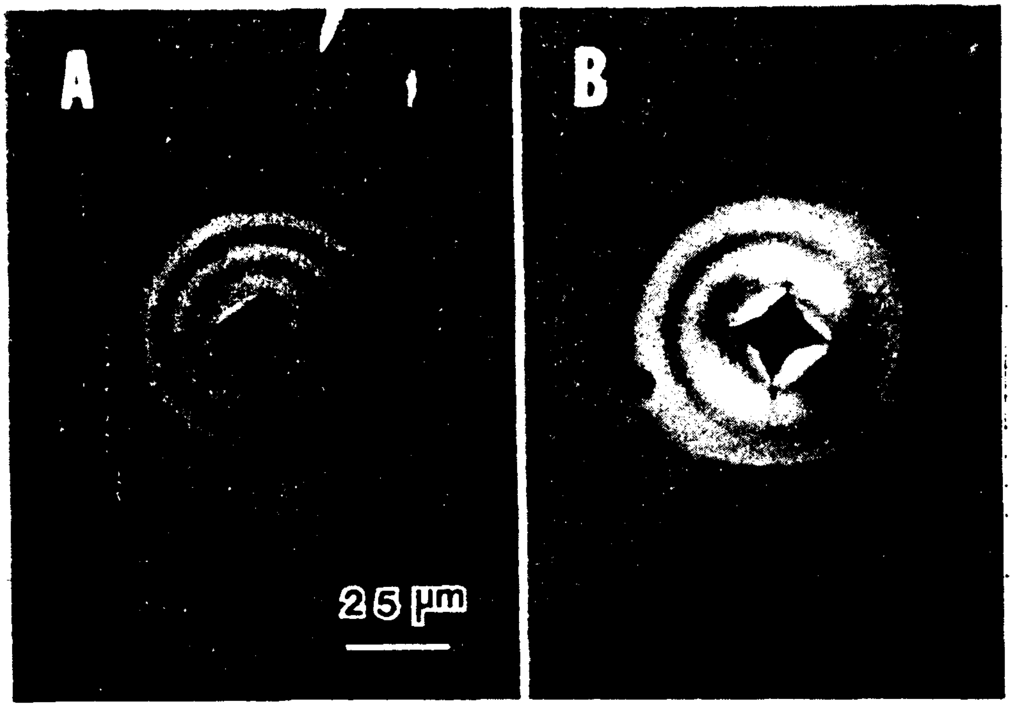

Fig. 5. Optical micrographs of 300 g Indentations made on A) 6 μm ZnO/1000Å SiO_2/(111)Si-N type, B) 6 μm ZnO/1500Å Pt - 500A Ti/(111)Si-N type. The average crack radius is smaller in the latter, indicating a superior adhesion.

Independent measurements of the acoustic properties[24] indicate appreciably larger acoustic signals for the latter. A correlation between adhesion and acoustic properties is thus established. The origin of the correlation is not evident at this juncture, but it is presumed that deposition conditions that develop a good quality interface also lead to films of high quality which, in turn, provide good acoustic properties.

Another series of tests on 10 μm ZnO/1000Å SiO_2/(111) Si samples are summarised in fig. 6. One sample exhibits superior adhesion to the other two, as manifest in a faceted lateral crack configuration, with a smaller average crack radius. Sectional views of these samples (fig. 7) indicates that the sample with the superior adhesion consists of a ZnO film with columnar grains, oriented with (0001) normal to the substrate surface. This film also exhibits greater optical transparency. Additionally, x-ray rocking curve experiments show that the full width at half maximum of the (0001) diffraction peak is smaller for the sample with superior adhesion than for the other samples, (1.9° compared to 2.8°).

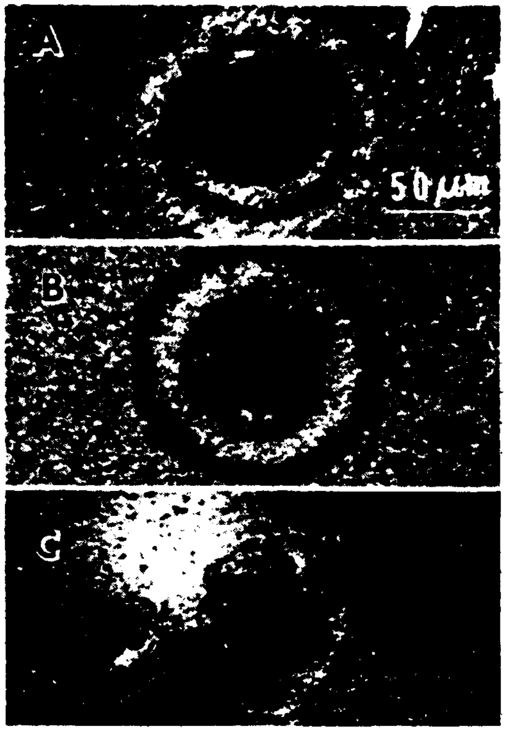

Fig. 6. Optical micrographs of 1000 g indentations on three 10 μm ZnO/1000A SiO_2/(111)Si samples deposited under different conditions. (C) shows better adhesion than (A) or (B), as manifest in a faceted lateral crack configuration, with a smaller average crack radius.

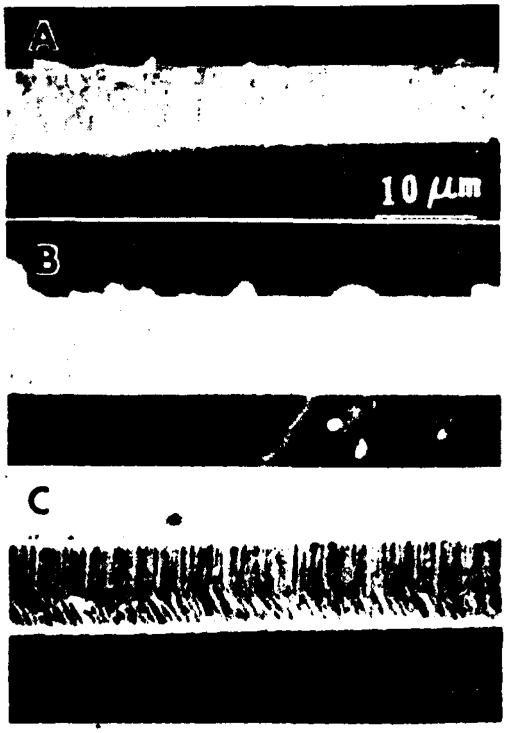

Fig. 7. Scanning electron micrographs of fracture surfaces through the three samples shown in Fig. 6. Sample (C), which exhibits superior adhesion, shows a columnar grain structure in the ZnO film.

ther studies have indicated that films with a highly oriented structure, good optical quality, and columnar grain structures typically provide optimum acoustic properties$^{25-28}$. Again, therefore, the measure of adhesion obtained by indentation seems to reflect trends in other important physical properties.

The sensitivity of the indentation test to inferior adhesion is demonstrated in fig. 8. Very large lateral cracks develop on poor quality films; in some instances causing sections of the film to be removed (fig. 8B). The variability in the extent of lateral fracture obtained at various locations over the surface indicates that adhesion in such films exhibits substantial spatial variation (good quality films show very little scatter in the lateral crack dimension).

Finally, the application of indentation tests, as a simple means for monitoring trends in adhesion is emphasized. For this purpose, 10 µm ZnO/Si samples have been annealed in air and in vacuum and then the lateral fracture extension determined in each

FIRST LINE OF TEXT (FIRST PAGE)

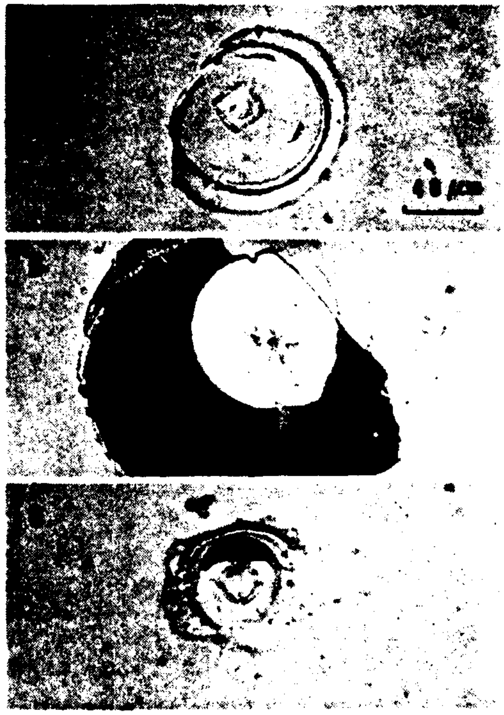

Fig. 8. Optical micrographs indicating variations in the lateral crack size for a sample indented at different locations. This film exhibits poor and variable adhesion.

case (fig. 9). It is immediately evident that vacuum annealing substantially enhances the adhesion, while annealing in air causes a corresponding degradation.

THE INTERFACE TOUGHNESS

A quantitative measure of the interface toughness can be provided by developing an adequate model of lateral crack extension. The extension of well developed indentation fractures has recently been subject to successful analysis by treating the indentation plastic zone as a precompressed spring that provides the driving force for crack extension, and relaxes as the crack extends[11,12]. This same approach can be used to anticipate the crack extension c along an interface, located at depth, h, beneath the surface (fig. 10). The analysis in this case differs from that in a homogeneous material[12] only in the treatment of depth h (for interface cracks h is constant and equal to the film thickness, whereas cracks in a homogeneous material are located at the base of the deformation zone and h varies with indentation load). The result obtained for the interface lateral cracks is;

$$c = \alpha[1 - P_o/\hat{p}]^{1/2}\,\hat{p}^{1/4} \qquad (1)$$

where $\hat{p}$ is the peak indentation load, P_o is a threshold load for crack formation and α is given by;

$$\alpha^2 = \alpha_1\, h^{3/2}\, H^{1/2}/K_{IC} \qquad (2)$$

where α_1 is a material independent coefficient that can be determined by calibration, on a homogeneous material with known H and K_{IC}. Such calibration experiments have been performed on glass[12]; experiments which yield a value for $\alpha_1 = 6.4 \times 10^{-8}$. Hence, an experimental determination of α, obtained by fitting crack lengths at several load levels to eqn. (1), permits K_{IC}^{inter} to be obtained from eqn. (2); provided the film thickness h is also measured (H is determined directly from $\hat{p}$ and the indentation diagonal).

Experimental results obtained for a $ZnO/SiO_2/Si$ system are shown in fig. 11. A fit of data to eqn. (1) indicates that the threshold load is $P_o = 3N$ and that $\alpha = 4.5 \times 10^{-5}\,m\,N^{-1/4}$. Inserting $h = 10\ \mu m$ and $H = 8.5GPa$ into eqn. (2), the interface toughness is determined to be $0.1\ MPa\sqrt{m}$. This compares with material toughness of, $0.6\ MPa\sqrt{m}$ for Si, $\sim 0.7\ MPa\sqrt{m}$ for SiO_2 and $\sim 1 MPa\sqrt{m}$ for ZnO. The interface thus exhibits a lower fracture toughness than the constituent materials, as required for the observation of interface fracture. Preliminary credence in the model is thus provided. Much additional experimentation is needed, however, to determine if the analysis correctly predicts trends in film thickness, load and interface toughness.

6 1/2 x 9 7/8

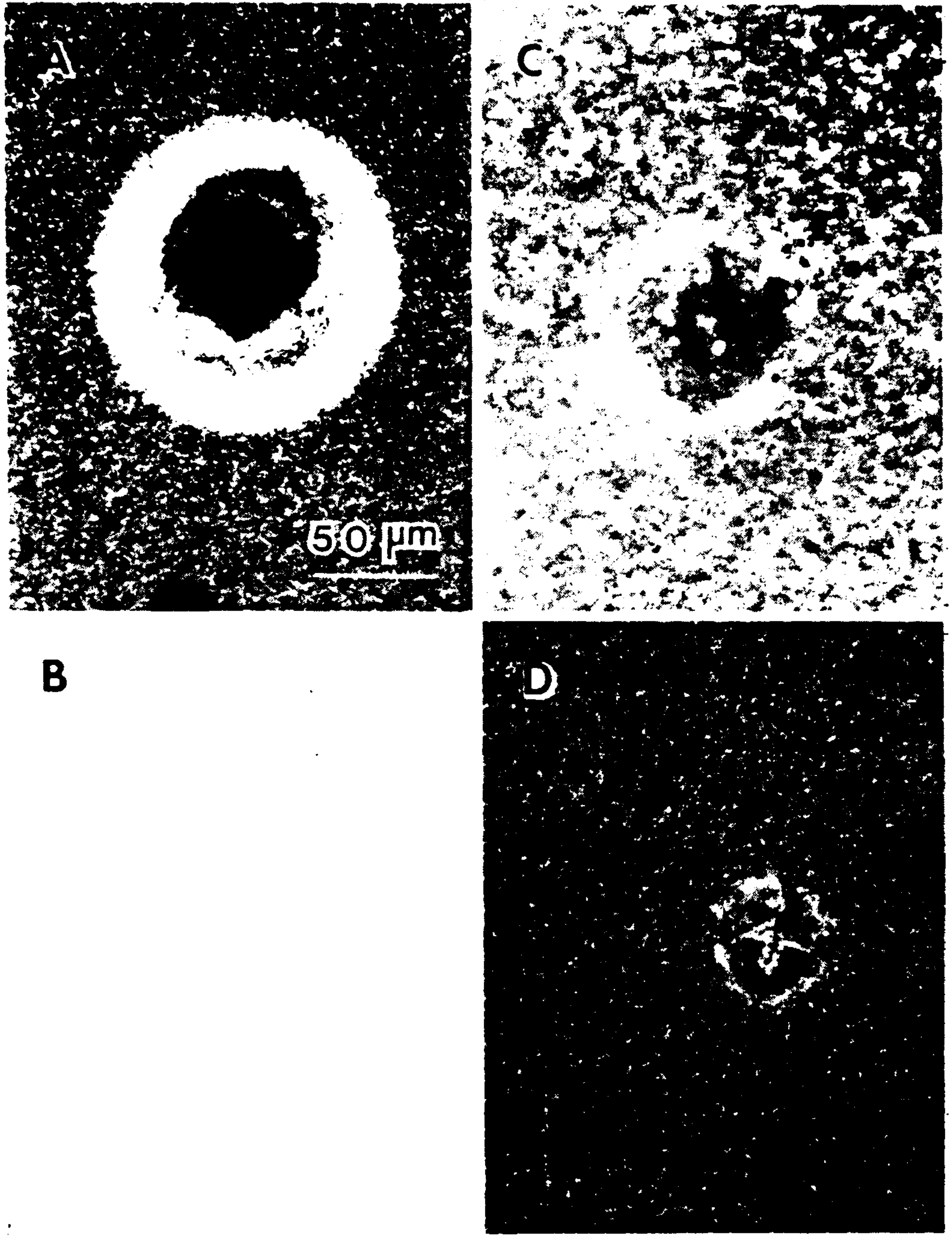

Fig. 9. Optical micrographs of 1000 g indentations on 10 µm ZnO/(111)Si samples annealed at 1000°C for 1 hr in different atmospheres. (A) as deposited sample (B) annealed in air. Film peeled off dramatically after indentation indicating adhesion is very poor. (C) annealed in vacuum at low oxygen partial pressure, adhesion is imporved as compared to (A). (D) annealed in vacuum at extra low oxygen partial pressure. Both the hardness and the adhesion of the film exhibited the greatest improvement.

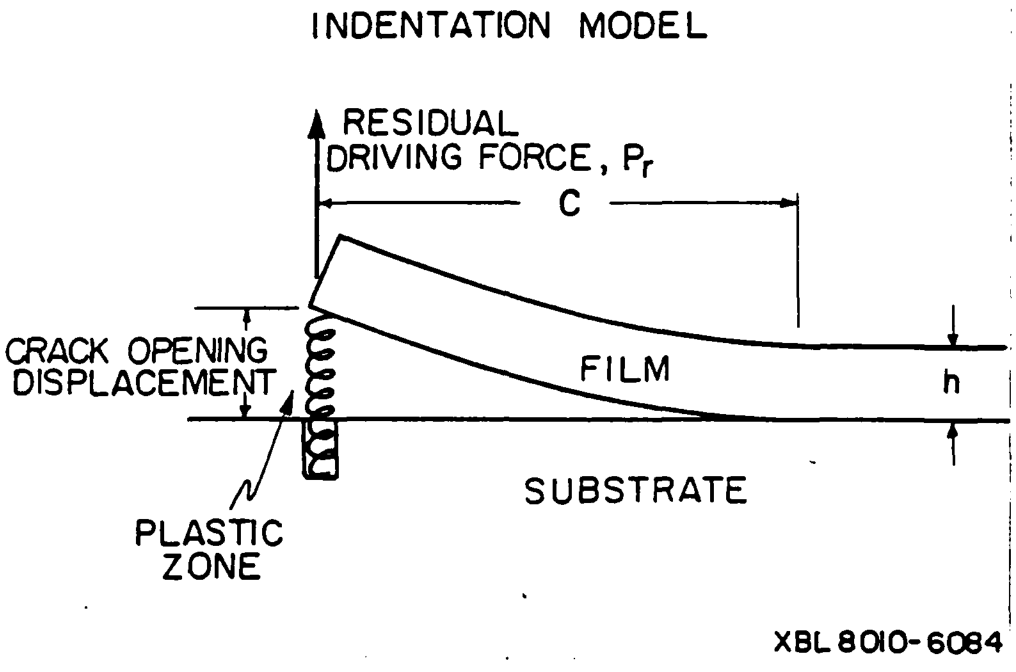
INDENTATION MODEL
RESIDUAL DRIVING FORCE, P_r
C
CRACK OPENING DISPLACEMENT
FILM
h
SUBSTRATE
PLASTIC ZONE
XBL 8010-6084

Fig. 10. A schematic of the Indentation Model indicating the residual force associated with the plastic zone that acts as the driving force for lateral crack extension.

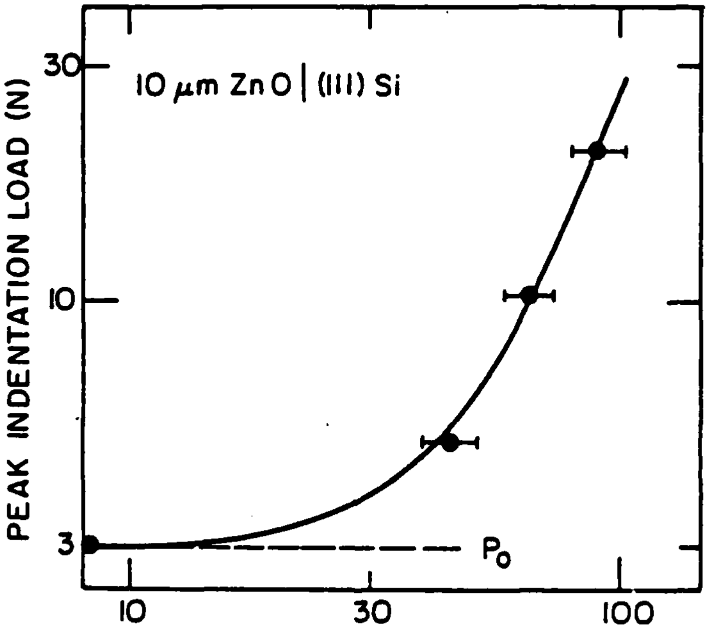

Fig. 11. Dependence of the lateral crack length on the indentation load. The specimen is 10μm ZnO/1000Å SiO_2/(111)Si.

DISCUSSION AND CONCLUSIONS

A simple indentation test for measuring the adherence of thin or thick films to substrates has been developed. The general utility of this test as a simple way for establishing trends in the adherence of film systems, achieved by employing different deposition or post-deposition techniques, has been demonstrated. This was achieved by conducting experiments on various ZnO/Si systems. Important influences on adhesion of the interlayer material (Pt/Ti being preferred to SiO_2) and of the deposition conditions (columnar ZnO grain morphologies yielding superior adhesion) were discussed and correlated with the acoustic properties. Additionally, substantial effects of heat treatment procedures on the adherence were detected in this manner. The simplicity of the indentation technique renders it ideally suitable for trend determinations of this type. The technique can be used with small specimens (a few millimeters in length), no special specimen preparation is required, a standard hardness testing machine and optical microscope are the only requirements, the adherence measurements are reproducible, and results can be obtained routinely, quickly and with minimal material damage.

The development of indentation methods for the absolute measurement of interface fracture resistance has been studied. An analytic solution for well developed lateral cracks has been shown to conform quite satisfactorily with data obtained on a ZnO/Si system. Further experimental studies are needed to substantiate the fracture model. Thereupon, the method should be capable of providing direct information concerning the fracture toughness of interfaces.

REFERENCES

1. K. L. Mittal "Adhesion Measurement: Recent Developments, Unsolved Problems, and Prospects," in Adhesion Measurement of Thin Films, Thick Films and Bulk Coatings, ASTM STP 640, K.L. Mittal Ed., pp. 5-17.
2. D. S. Campbell, "Mechanical properties of thin films," in "Handbook of Film Technology," L. I. Maissel and R. Glang, Editors, Chapter 12, McGraw Hill Book Company, N.Y., 1970.
3. B. N. Chapman,"Thin-film adhesion," J. Vac. Sci. Tech. II, 106-113 (1974).
4. K. L. Mittal "Adhesion of Thin Films," Electrocomponent Sci. Technol. 3, 21-42 (1976).
5. R. P. Arnard, Microelectronics and Reliability, Vol. 10, No. 4, 1971, pp. 269-275.
6. J. Savage in "Handbook of Thick Film Technology," P.J. Holmes and R. G. Loasby, Eds., Electrochemical Publications Ltd., Ayr, Scotland, 1976, pp. 108-112.

7. T. R. Bullet and J. L. Prosser, "The Measurement of Adhesion," Prog. Org. Coatings 1, 45-7 (1972).
8. T. T. Hitch, "Adhesion Measurement on Thick Film Conductors" in "Adhesion Measurement of Thin Film, Thick Film and Bulk Coatings," ASTM STP 640, K. L. Mittal Ed., 211-231. American Society for Testing and Materials, Philadelphia, PA (1978).
9. R. J. Good, "Locus of Failure and Its Applications for Adhesion Measurements" in ASTM STP 640 (Ed. K. L. Mittal) pp. 18-26, 1978.
10. W. D. Bascom, P. F. Becher, J. L. Batner and J. S. Murdoy, "Use of Fracture Mechanics Concepts in Testing of Film Adhesion," in ASTM STP 640 (Ed. K. L. Mittal) pp. 63-69, 1978.
11. B. R. Lawn, A. G. Evans and D. B. Marshall, "Elastic/Plastic Indentation Damage in Ceramics: The Median-Radial Crack System," J. Amer. Ceram. Soc., in press (Sept-Oct issue, 1980).
12. B. R. Lawn, A. G. Evans and D. B. Marshall, "Elastic/Plastic Indentation Damage in Ceramics: the Lateral Crack System," in preparation.
13. D. B. Marshall, B. R. Lawn and P. Chantikul, "Residual Stress Effects in Sharp Contact Cracking: II. Strength Degradation," J. Mater. Sci. 14, 2225-2235 (1979).
14. D. B. Marshall and B. R. Lawn "Flaw Characteristics in Dynamic Fatigue; the Influence of Residual Contact Stresses," J. Amer. Ceram. Soc., in press (Sept-Oct issue, 1980).
15. A. G. Evans, "Impact Damage in Ceramics" in Fracture Mechanics of Ceramics (Eds. R. C. Bradt, D. P. H. Hasselman and F. F. Lange), Plenum Press, New York, 1978, pp. 303-331, Vol. 3.
16. S. M. Wiederhorn and B. R. Lawn, "Stength Degradation of Glass Impacted with Sharp Particles: I. Annealed Surfaces," J. Amer. Ceram. Soc., 62 [1-2] 66-70 (1979).
17. D. B. Marshall, B. R. Lawn and J. J. Mecholsky, "Effect of Residual Stresses in Mirror/Flow-Size Relations," J. Amer. Ceram. Soc. 63 [5-6] 358-360 (1980).
18. A. G. Evans, M. E. Gulden and M. Rosenblatt, "Impact Damage in Brittle Materials in the Elastic-Plastic Response Regime," Proc. Roy. Soc. Lond. A361 343-365 (1978).
19. M. V. Swain, "Microcracking Associated With Scratching of Brittle Solids," in Fracture Mechanics of Ceramics (Eds. R. C. Bradt, D. P. H. Hasselman and F. F. Lange), Plenum Press, New York, 1978, pp. 257-272, Vol. 3.
20. A. G. Evans and E. A. Charles, "Fracture Toughness Determinations by Indentation," J. Amer. Ceram. Soc., 59 [7-8] 371-372 (1976).
21. G. R. Anstis, P. Chantikul, B. R. Lawn. D. B. Marshall, "A Critical Evaluation of Indentation Techniques for Measuring Fracture Toughness: I. Direct Crack Measurements," Submitted to J. Amer. Ceram. Soc.
22. P. Dokko and A. G. Evans, unpublished work.
23. S. S. Chiang, D. B. Marshall and A. G. Evans, "The Response of Solids to Elastic/Plastic Indentation," In preparation.

24. B. T. Khari-Yakub, unpublished work.
25. A. J. Bahr, R. E. Lee, F. S. Hickernell, C B. Willingham, and T. M. Reeder "A Comparison between the Physical Structure of Sputtered Zinc Oxide Films and the Measured Electrochemical Coupling Factor for Surface Acoustic Waves Generated by Such Films," Unltrasonic Symposium Proceedings, pp. 202-205, Oct. 1972.
26. F. S. Hickernell, "Microstructure of ZnO Films Used for Acoustic Surface Wave Generation," J. Vac. Sci. and Technol. Vol. 12, pp. 879-883 (1975).
27. B. T. Khuri-Yakub, G. S. Kino and P. Galle, "Studies of the Optimum Conditions for Growth of Vf-Sputtered ZnO Films," J. Appl. Phys. 46, 3266-3272 (1975).
28. T. Shiosaki, "High Speed Fabrication of High Quality Sputtered ZnO Thin Films for Bulk and Surface Wave Applications," Ultrasonic Symposium Proceedings, pp. 100-110 (1978).

ACKNOWLEDGMENT

This work was supported by a U.S. Office of Naval Research Grant, Contract number N00014-79-C-0159.

CHAPTER VII

THE MARTENSITE CRYSTALLOGRAPHY OF TETRAGONAL ZIRCONIA

by

*W. M. Kriven, **W. L. Fraser and ***S. W. Kennedy

*Department of Materials Science and Mineral Engineering,
University of California,
Berkeley, CA 94720

**Kodak Research Laboratories, Coburg, 3058, Victoria, Australia

***University of Adelaide, Adelaide, 5001, South Australia, Australia

INTRODUCTION

It is now well established that zirconia is amongst the most refractory, thermal shock and corrosion-resistant oxides. At atmospheric pressure zirconia exists as three modifications:(1)

Melt $\xrightarrow{2680^{\circ}C}$ Cubic (I) $\xrightarrow{2200^{\circ}C}$ Tetragonal (II) $\xrightleftharpoons[950^{\circ}C]{1150^{\circ}C}$ Monoclinic (III).

The tetragonal to monoclinic transformation is martensitic and accompanied by a 3% volume increase, both of which are physically delecterious to the ceramic. The transformation may be suppressed however, by small additions of other oxides, notably CaO, Y_2O_3 and MgO(2). The cubic, fluorite-type solid solution then persists to room temperature, as fully stabilized zirconia, FSZ. The more useful mechanical properties of zirconia arise from composite microstructures of monoclinic(3) or tetragonal(4) particles of pure zirconia dispersed in a matrix of cubic zirconia, constituting partially stabilized zirconia, PSZ.

The crystal structures of each phase are summarized in Fig.1. Due to the similarity of tetragonal and monoclinic face centred cells, three different lattice correspondences may arise(5) as illustrated in Fig.2. If a right hand screw convention is adopted for unit cell axes, lattice correspondences A, B or C may be defined, depending on which monoclinic axis a_m, b_m or c_m respectively is parallel to c_t.

Bailey(5) examined the II to III transformation by transmission electron microscopy and found twinning on (110), $(1\bar{1}0)$ and (100) monoclinic planes, as well as shape changes and an orientation relation, LC C. He found indirect evidence for orientation relations derived from all three lattice correspondences. A martensitic mechanism for the tetragonal to monoclinic transformation was first reported by Wolten(6) who found symmetry options and variants for the orientation relation derived from lattice correspondence C. He concluded that the interface had a monoclinic habit plane (101) which becomes (101), (110) and (011) of the tetragonal cell. His X-ray orientation relations imply all three lattice correspondences. As reviewed by Subbarao et al.(1), several other determinations of orientation relations essentially arise from LC B or LC C.

Bansal and Heuer(7,8) examined single crystal II and III transformations by transmission electron microscopy and X-ray precession experiments. They found that an orientation relation derived from LC B occured for an A_s temperature above 1000°C. A_s is the temperature at which the reverse (monoclinic to tetragonal) temperature starts. An LC C (i.e.,"type 3") orientation resulted from an M_s below 1000°c. Habit planes of the type $(671)_m$ or $(761)_m$, being approximately 7° off $(110)_m$, constituted type A, and usually occured inside the crystal as opposed to surface regions where type B habit planes were found. Type B plates were also lenticular shaped with a midrib close to $(100)_m$ or $(010)_m$, corresponding to internal twinning on these planes. Coarse $(100)_m$ twins were also observed in plate-free regions.

Martensite calculations were performed by Bansal and Heuer(8) utilizing the algebraic method of Bowles and MacKenzie(9), for eight slip lattice invariant shear (LIS) systems. They were done for lattice correspondence B and C as summarized below:

LC B	$(1\bar{1}0)[001]$	$(111)[1\bar{1}0]$	$(100)[001]$	$(100)[011]$
LC C	$(1\bar{1}0)[001]$	$(1\bar{1}0)[110]$	$(10\bar{1})[010]$	$(111)[1\bar{1}0]$

Martensite analyses on LC C by $(1\bar{1}0)[001]$ slip system predicted $\{671\}_m$ habit planes, while $(100)_m$ habit planes were predicted by slip on $(1\bar{1}0)[110]$. No martensite analyses using LIS twinning systems have as yet been reported.

In the details of the Bansal and Heuer(8) calculations, a numerical error was noted. A check on the volume increase in the transformation using the algebraically calculated magnitudes of the principle distortions had values of 1.8360% and 1.8356% for the two lattice correspondences B and C, respectively. The volume change from the unit cell dimensions at 1000°C as used by Bansal and Heuer(8) showed that the volume increase is actually 1.9030%. Errors in these initial stages of the work could be misleading.

In this work we present calculations of possible crystallographic transformation mechanisms in bulk, unconstrained zirconia crystals. For all three lattice correspondences slip as well as one twin LIS systems are analysed. Habit planes, shape changes and orientation relations for each variant are predicted in terms of the tetragonal structure. The shape changes associated with each mechanism and its variants are compared.

ANALYSIS

Lattice parameters of both tetragonal and monoclinic phases corresponded to a transformation temperature of 950°C. They were calculated from experimental parameters and thermal expansion coefficients determined by Patil and Subbarao(10,11) and gave a

II to III volume expansion of approximately 3.0%. Thermal expansion was shown to be anisotropic. The current analysis at 950°C gave a value of 3.047% which was consistent with the volume increase as calculated from lattice parameters. Buljan, McKinstry and Stubican determined lattice parameters at 1000°C which were used by Bansal and Heuer(8) and also in this analysis to compare the effect of lattice parameter differences.

The martensite analysis as formulated by Bowles and MacKenzie(9) was programmed into Fortran IV computer language by Ledbetter and Wayman(12) in PRØGRAM MRTNST. Calculations were done in an orthonormal frame of reference in which input data also needed to be expressed. In zirconia, part of the lattice deformation may be visualized as a simple contraction or expansion in the direction corresponding to b_m which was here designated as the η_3 direction. The remainder of the lattice deformation occured in the plane which is normal to this direction. The determination of the two principle axes and distortions in this plane was readily accomplished by standard geometrical theory for homogeneous strain in two dimensions(13). The details are given in Appendix 1. These calculations of principle strain magnitudes and directions were confirmed by the general method of Bowles and MacKenzie(9). Table 1 presents lattice parameters of the two phases at 950°C, while calculated values of the deformations are given in Table 2.

Important features arising from the above are firstly, that two of the principle deformation directions are irrational. Secondly, the magnitude of η_3 varies only by approx. 1% from unity for all three lattice correspondences. Finally, the values of η_3 - 3 which are usually taken as measures of the strain energy favour lattice correspondence C, but not greatly.

Physically, lattice invariant shears occur in the product, monoclinic phase, but LIS systems were specifield in the tetragonal phase to which they were referred from the monoclinic cell, by inspection of lattice correspondence. The lattice invariant shear systems investigated were derived mainly from dislocations, stacking faults and twinning shears found in the monoclinic phase after transformation, by previous experimental studies. For lattice correspondence B, the twin system (010)$[100]_t$ was analysed, where the direction of twinning shear was specified in the input data and treated as a slip system. Mathematically, computations are identical for slip and twinning. This approach was necessary as PRØGRAM MRTNST was unable to calculate twin directions for non-orthogonal systems. A simple flow chart describing the method of calculations is drawn in Fig.3.

RESULTS

It was sometimes difficult to asses whether or not a predicted magnitude of lattice invariant shear was physically reasonable. Lattice invariant shears by twinning posed no problem as magnitudes determine relative proportions of each twin in the product. The lattice invariant shear angle must therefore be less than the angle of twinning shear. For slip or stacking fault shears the shear angle associated with an individual dislocation or stacking fault was readily determined and in this work any LIS angle greater than half the maximum value was taken to indicate an unreasonable defect density. Thus, a LIS of 20° C was taken as an upper limit for " reasonable " solutions. Shape strains (m_1) greater than 20% were considered unlikely and hence not reported.

Table 3 compares the calculations of Bansal and Heuer(8) with those computed by the current method, using the same lattice parameters at 1000° C. It is seen that although there is general agreement there is a scatter of habit planes, and variation in the magnitude of shape strain by approximately 10%. Table 4 summarizes habit planes and shape strains (m_1, d_1) predicted at 950° C for each mechanism. The combination of all three lattice correspondences with LIS systems yielded 32 distinct reasonable solutions. Comparison of above results indicate that quantitative predictions of martensite mechanisms depend on lattice parameters of both phases and their values at the same transformation temperature.

Orientation relations were determined by multiplying vectors and plane normals by the total strain matrix(12) . A vector V was rotated to become a vector V' both in the same cubic basis. The mutual angle of rotation was then calculated for that crystal system. With reference to the operating lattice correspondence, the product vectors and plane normals were then re-labelled according to the monoclinic axes. The details of predicted orientation relations are presented in Table 5.

Twinning on $\{010\}\langle\bar{1}00\rangle$ as lattice invariant shear resulted in four symmetry-equivalent solutions for each twin plane. The shear angle associated with twinning in this way was 8.78°. The proportion of each twin in the product was predicted to be 0.409 : 0.591 and 0.617 : 0.383 (for LIS angle = 3.61° and 5.44°, respectively). These ratios were close to 2:3 and 3:2. Habit planes approximated to $\{\bar{1}\bar{2}1\}_t$ and the total shape change was significantly less than the shape change of the lattice. The four different (but equivalent) orientation relations for each twinning LIS system could each be described by:

$|001|_t \, {}^{\Lambda}|010|_m = 1.18^{\circ}$, $\{100\}_t \, {}^{\Lambda}(100)_m = 1.14^{\circ}$.

DISCUSSION

The calculations presented above are quantitative analyses of possible crystallographic transformation mechanism operating at a temperature of $950^{\circ}C$. Comparison of results based on different lattice parameters and values of principle strains indicates that such predictions are dependent on lattice parameters of both parent and product phases, and that their values at the same transformation temperature should be used. Since lattice parameters are affected by solute content$^{(14)}$ which also affects the M_s temperature, different mechanisms may thus be favoured or altered under different conditions.

For all three lattice correspondences the outstanding feature of the results obtained with stacking fault or slip modes (apart from $\{010\}\langle 101\rangle$) is the small ($<1^{\circ}$) of LIS shear required. The predicted crystallography is therefore very similar for a number of possible LIS systems. Individual orientation relations therefore might only be resolved with precise transmission electron microscopy since particular reflections from one variant would occur within 2-3 degrees of equivalent reflection from other variants.

The shape strain may be resolved into components parallel and perpendicular to habit planes (Fig.4).(15) From Table 3 it is seen that most of the shape strain (m_1) is resolved parallel to the habit plane. Table 4 shows that slip LIS mechansims produce shape strains of 11% - 17%, while the $(010)_{tet.}$ twin system produced strains of 5% per variant.

As mentioned in the introduction, there is some experimental evidence for the occurrence of both lattice correspondence B and C. There is no apparent reason why lattice correspondence A should be less probable. From Table 5 it is seen that the rotational component of the total mechanism is small in all instances. Hence $[\text{axis}]_t \, || \, [\text{axis}]_m$ does imply that $[\text{axis}]_t$ becomes $[\text{axis}]_m$ in the transformation.

The $(010)_t$ twin system, by lattice correspondence B (Fig.2) becomes $(001)_m$ or $(100)_m$ when equivalent a_t and b_t axes are interchanged. $(100)_m$ and $\{110\}_m$ deformation twinning was found by Bailey(5) in thin TEM specimens. Kriven(16) also found the same twin systems in small included ZrO_2 particles in Al_2O_3-ZrO_2 and pure ZrO_2 (42% volume fraction tetragonal) ceramics.

The calculations presented here however, imply that the $(100)_m$ and $(001)_m$ can also act as lattice invariant shear systems in a martensitic mechanism, giving rise to a macroscopic shape change and habit plane. This finding may be relevant to understanding how stress-induced martensitic transformation, in included zirconia particles are able to toughen composite ceramics.

The fact that $(100)_m$ may act as an LIS twin system further suggests that martensite calculations be performed for all the $(100)_m$ and $\{110\}_m$ twin systems in combination with the three lattice correspondences . Such calculations would require modification of the method here presented.

CONCLUSION

In conclusion, therefore, we have quantitatively analysed some martensitic transformation mechanisms in zirconia. The analyses presented were purely geometrical and based on the invariant plane strain criterion of a martensitic transformation in a bulk crystal. Lattice parameters were corrected for both tetragonal and monoclinic phases to the same transformation temperature of 950°C. Three principle strain axes were determined in the monoclinic unit cell, and the different tetragonal LIS systems were obtained from the monoclinic cell by inspection, with reference to three lattice correspondences. The computed martensite analyses then yielded solutions which predicted habit planes, shape strains related to the habit planes and orientation relations for each variant, given with respect to the tetragonal structure. Most of the LIS slip systems had shape strains of the order of 11% - 17%, while one twin LIS system had 5% shape strains resolved essentially parallel to the habit plane.

Thus, the work presented here has shown that (1) the $(100)_m$ or $(001)_m$ twin systems may act as lattice invariant shear systems, giving a martensitic solution with macroscopic shape changes and habit planes etc. (2) It illustrates the different shape changes associated with each mechanism and variant. (3) It indicates the importance of using lattice parameters corrected to the same transformation temperature.

ACKNOWLEDGEMENTS

The authors thank Drs. H.M.Ledbetter and C.M.Wayman for a copy of PROGRAM MRTNST. S.W.Kennedy acknowledges a calculations grant from the Australian Research Grants Commitee. W.M.Kriven thanks Mr. D.M.Huang and Prof. A.G.Evans of the University of California at Berkeley, for valuable discussions during the preparation of this manuscript which was done with the support of a U.S.Navy Grant, Contract number 842456-25989.

The authors express their appreciation for the financial support of this research provided by the Office of Naval Research (A.G.E.) under contract No. N0014-79-C-0159.

REFERENCES

1. E.C. Subbarao, H.S. Mai .i, K.K. Srivastava, Phys.stat.sol.A 21, (1974), 9-40.

2. B.C. Weber, H.J. Garrett, F.A. Mauer, M.A. Schwartz, J.Am.Ceram.Soc.39, (1956), 197-207.

3. R.C. Garvie, P.S. Nicholson, J.Am.Ceram.Soc.55, (1972), 152-157.

4. R.C. Garvie, R.H. Hannick, R.T. Pascoe, Nature 258, (1975), 703-70

5. J.E. Bailey, Proc.Roy.Soc.A 279, (1964), 359-412.

6. G.M. Wolten, Acta Cryst.17, (1964), 763-765.

7. G.K. Bansal, A.H. Heuer, Acta Met.20, (1972), 1281-1289.

8. G.K. Bansal, A.H. Heuer, Acta Met.22, (1974), 409-417.

9. J.S. Bowles, J.K. MacKenzie, I. Acta Met.2, (1954), 129-137.
II. Acta Met.2, (1954), 138-147.
III. Acta Met.2, (1954), 224-234.

10. R.N. Patil, E.C. Subbarao, J.Appl.Cryst.2, (1969), 281-288.

11. R.N. Patil, E.C. Subbarao, Acta Cryst.A 26, (1970), 535-542.

12. H.M. Ledbetter, C.M. Wayman, Mat.Sci.Eng.7, (1971), 151-157.

13. J.C. Jaeger, "Elasticity, Fracture and Flow", Methuen & Co. Ltd. London, (1964), 23-29.

14. R.H.J. Hannink, J.Mat.Sci.13, (1978), 2487-2496.

15. Z. Nishiyama, "Martensitic Transformation", 1978, Academic Press, 372-3, Ed. by M.E. Fine, M. Meshii, C.M. Wayman.

16. W.M.Kriven, submitted to Advances in Ceramics, Proc. First Intern.Conf. on Zirconia, CWRU, Cleveland, USA. June 16-18th,1980.

Table 1. Lattice Parameters

Temp.	a_m	b_m	C_m	β	Temp.	a_t	c_t
956°C (measured)	5.1882	5.2142	5.3836	81.217	1152°C (measured)	5.1518	5.2724
950°C (calculated)	5.1881	5.2142	5.3835	81.22	950°C (calculated)	5.1485	5.2692
(Thermal expansion coeff α X10^6 C°$^{-1}$)	10.31	1.35	14.68			11.60	16.08

Table 2. Principal Distortions
(indices referred to an orthonormal basis with axes parallel to the base axes of the tetragonal lattice)

		L.C. 1	L.C. 2	L.C. 3
η_1:	Direction	[0, 0.8267, 0.5627]	[0, 0.7383, −0.6745]	[0.7860, −0.6183, 0]
	Magnitude	1.0956	0.9337	0.9428
η_2:	Direction	[0, −0.5627, 0.8267]	[0, 0.6745, 0.7383]	[0.6183, 0.7860, 0]
	Magnitude	0.9287	1.0897	1.1045
η_3:	Direction	[100]	[100]	[001]
	Magnitude	1.0128	1.0128	0.9896
$\Sigma\eta_i^2 - 3 =$		0.0885	0.0850	0.0880

ΔV (increase) = $100 - |1 - \eta_1\eta_2\eta_3| = 3.047\%$.

Table 3. Comparison of computed method of calculations with those of Bansal and Heuer,(8) using uncorrected lattice parameters at 1000°C. The shape strain is resolved into components parallel and perpendicular to habit planes.(15)

Lattice Correspondence	Shear System	Habit Plane	Direction d_1	Magnitude M_1	% Strain X	% Strain Y
BANSAL & HEUER (SLIP):						
LC C	$(1\bar{1}0)[001]$	$\begin{pmatrix}-.62070\\-.775527\\-.115215\end{pmatrix}$ $\sim(\bar{6}\bar{7}\bar{1})$	$\begin{bmatrix}-.03455\\-.01366\\-.99931\end{bmatrix}$	.12363	1.8	12.2
LC C	$(1\bar{1}0)[110]$	$\begin{pmatrix}.996597\\-.014290\\.081068\end{pmatrix}$ $\sim(100)$	$\begin{bmatrix}.02768\\.10149\\.99445\end{bmatrix}$	.16248	1.73	16.1
FRASER, KRIVEN & KENNEDY (SLIP)						
LC C	$(1\bar{1}0)[001]$ (a)	$\begin{pmatrix}-.802\\-.586\\-.118\end{pmatrix}$ $\sim(\bar{7}\bar{6}\bar{1})$	$\begin{bmatrix}-.168\\.123\\-.955\end{bmatrix}$ $[\bar{1}\bar{1}\bar{8}]$	.110	1.9	10.5
	(b)	$\begin{pmatrix}-.207\\.090\\-.998\end{pmatrix}$ $\sim(\bar{1}0\bar{5})$	$\begin{bmatrix}-.799\\.598\\-.061\end{bmatrix}$ $\sim[110]$	.110	1.9	10.5
LC C	$(1\bar{1}0)[110]$ (a)	$\begin{pmatrix}-.014\\.997\\.084\end{pmatrix}$ $\sim(010)$	$\begin{bmatrix}.002\\.043\\.975\end{bmatrix}$ $\sim[001]$	.153	1.9	14.8
LC C	(b)	$\begin{pmatrix}.001\\.118\\1.017\end{pmatrix}$ $\sim(010)$	$\begin{bmatrix}-.015\\1.000\\.007\end{bmatrix}$ $\sim[010]$	.153	1.87	15.1

Table 4. PREDICTIONS OF HABIT PLANES AND SHAPE STRAINS.

LATTICE INVARIANT SHEAR SYSTEM	HABIT PLANE INDICES (P1)	DIRECTION OF SHAPE STRAIN D1	MAGNITUDE OF SHAPE STRAIN M1
Lattice Correspondence: A			
$(010)\ [101]$	$\begin{pmatrix}0.162\\-0.971\\0.181\end{pmatrix}$ $\sim(1\bar{6}1)$	0.638 -0.281 0.701 $\sim[2\bar{1}2]$	0.122
	$\begin{pmatrix}0.637\\-0.335\\0.711\end{pmatrix}$ $\sim(2\bar{1}2)$	0.126 -0.967 0.217 $\sim[1\bar{8}2]$	0.122
$(110)\ [\bar{1}10]$	$\begin{pmatrix}-0.012\\-0.996\\0.094\end{pmatrix}$ $\sim(0\bar{1}0)$	-0.002 -0.266 -0.942 $\sim[0\bar{2}\bar{7}]$	0.173
	$\begin{pmatrix}-0.003\\-0.346\\-0.960\end{pmatrix}$ $\sim(0\bar{1}\bar{3})$	-0.012 -0.984 0.171 $\sim[0\bar{6}1]$	0.173
$(101)\ [\bar{1}01]$	$\begin{pmatrix}0.012\\0.280\\0.982\end{pmatrix}$ $\sim(027)$	0.000 0.995 -0.094 $\sim[010]$	0.164
	$\begin{pmatrix}-0.001\\-1.000\\0.018\end{pmatrix}$ $\sim(0\bar{1}0)$	-0.012 -0.203 0.957 $\sim[0\bar{1}5]$	0.164

LATTICE INVARIANT SHEAR SYSTEM	HABIT PLANE INDICES (P1)	DIRECTION OF SHAPE STRAIN D1	MAGNITUDE OF SHAPE STRAIN M1
$(\bar{1}11)\ [110]$	$\begin{pmatrix}-0.057\\-0.996\\0.075\end{pmatrix}$ $\sim(0\bar{1}0)$	$\begin{matrix}0.031\\-0.238\\0.948\end{matrix}$ $\sim[014]$	0.185
	$\begin{pmatrix}0.025\\-0.324\\-0.968\end{pmatrix}$ $\sim(0\bar{1}\bar{3})$	$\begin{matrix}-0.061\\-0.985\\0.159\end{matrix}$ $\sim[0\bar{6}1]$	0.185
	$\begin{pmatrix}0.661\\0.354\\-0.678\end{pmatrix}$ $\sim(21\bar{2})$	$\begin{matrix}0.796\\-0.557\\0.232\end{matrix}$ $\sim[8\bar{5}2]$	0.178
	$\begin{pmatrix}0.839\\-0.515\\0.180\end{pmatrix}$ $\sim(5\bar{3}1)$	$\begin{matrix}0.598\\0.407\\-0.674\end{matrix}$ $\sim[32\bar{2}]$	0.178

Lattice Correspondence: B

$(010)\ [101]$	$\begin{pmatrix}-0.615\\-0.334\\0.730\end{pmatrix}$ $\sim(\bar{2}\bar{1}2)$	$\begin{bmatrix}-0.067\\-0.984\\-0.160\end{bmatrix}$ $\sim[0\bar{6}\bar{1}]$	0.120
	$\begin{pmatrix}-0.103\\-0.988\\0.122\end{pmatrix}$ $\sim(\bar{1}\bar{9}1)$	$\begin{bmatrix}-0.620\\-0.281\\0.716\end{bmatrix}$ $\sim[\bar{6}\bar{3}7]$	0.120
$(011)\ [01\bar{1}]$	$\begin{pmatrix}-0.049\\-0.999\\0.011\end{pmatrix}$ $\sim(0\bar{1}0)$	$\begin{bmatrix}-0.990\\-0.144\\-0.000\end{bmatrix}$ $\sim[\bar{7}\bar{1}0]$	0.159
	$\begin{pmatrix}-0.976\\-0.219\\0.001\end{pmatrix}$ $\sim(\bar{5}\bar{1}0)$	$\begin{bmatrix}0.026\\-1.000\\0.010\end{bmatrix}$ $\sim[0\bar{1}0]$	0.159

LATTICE INVARIANT SHEAR SYSTEM	HABIT PLANE INDICES (P1)	DIRECTION OF SHAPE STRAIN D1	MAGNITUDE OF SHAPE STRAIN M1
(010) $[\bar{1}00]$ (cont.)	$\begin{pmatrix} 0.383 \\ -0.810 \\ -0.455 \end{pmatrix}$ $\sim(1\bar{2}\bar{1})$	$\begin{matrix} 0.379 \\ -0.801 \\ 0.452 \end{matrix}$ $\sim[1\bar{2}1]$	0.052
	$\begin{pmatrix} 0.383 \\ -0.810 \\ 0.455 \end{pmatrix}$ $\sim(1\bar{2}1)$	$\begin{matrix} 0.379 \\ -0.801 \\ -0.452 \end{matrix}$ $\sim[1\bar{2}\bar{1}]$	0.052
(110) $[\bar{1}10]$	$\begin{pmatrix} 0.000 \\ -0.132 \\ -1.015 \end{pmatrix}$ $\sim(0\bar{1}\bar{8})$	$\begin{bmatrix} -0.013 \\ -0.998 \\ 0.063 \end{bmatrix}$ $\sim[0\bar{1}0]$	0.156
	$\begin{pmatrix} -0.013 \\ -0.990 \\ -0.142 \end{pmatrix}$ $\sim(0\bar{7}\bar{1})$	$\begin{bmatrix} 0.000 \\ -0.057 \\ -0.976 \end{bmatrix}$ $\sim[00\bar{1}]$	0.156
(101 $[\bar{1}01]$	$\begin{pmatrix} -0.013 \\ -0.049 \\ 1.022 \end{pmatrix}$ $\sim(001)$	$\begin{bmatrix} -0.004 \\ -0.990 \\ -0.140 \end{bmatrix}$ $\sim[0\bar{7}\bar{1}]$	0.159
	$\begin{pmatrix} -0.005 \\ -0.976 \\ -0.224 \end{pmatrix}$ $\sim(0\bar{9}\bar{2})$	$\begin{bmatrix} -0.013 \\ 0.028 \\ -0.977 \end{bmatrix}$ $\sim[00\bar{1}]$	0.159
$(\bar{1}11)$ [110]	$\begin{pmatrix} -0.062 \\ -0.988 \\ -0.144 \end{pmatrix}$ $\sim(0\bar{7}\bar{1})$	$\begin{bmatrix} 0.014 \\ -0.041 \\ -0.976 \end{bmatrix}$ $\sim[00\bar{1}]$	0.169
	$\begin{pmatrix} 0.009 \\ -0.122 \\ -1.016 \end{pmatrix}$ $\sim(0\bar{1}\bar{8})$	$\begin{bmatrix} -0.064 \\ -0.996 \\ -0.058 \end{bmatrix}$ $\sim[0\bar{1}0]$	0.169

Table 5. Details of Predicted Orientation Relations

(Angles are between planes and directions marked X)

L.I. Shear System	Solution	Tet. Planes {100}	Tet. Planes (001)	Mon. Planes (100)	Mon. Planes (010)	Mon. Planes (001)	Angle (°)	Tet. Directions <100>	Tet. Directions [001]	Mon. Directions [100]	Mon. Directions [010]	Mon. Directions [001]	Angle (°)
Lattice Correspondence A													
(010) [101]	1 (a)	X				X	0.47	X			X		0.86
	1 (b)	X				X	6.40	X			X		4.37
(110) $[\bar{1}10]$	1 (a)	X				X	0.76	X			X		0.72
	1 (b)		X	X			0.57	X			X		0.74
(101) $[\bar{1}01]$	1 (a)		X	X			0.77	X			X		0.73
	1 (b)	X				X	0.00	X			X		0.72
$(\bar{1}11)$ [110]	1 (a)	X				X	1.32	X			X		1.16
	1 (b)		X	X			0.53	X			X		0.51
	2 (a)	X				X	11.10	X			X		7.88
	2 (b)	X				X	5.47	X			X		5.78
Lattice Correspondence B											[010]		
(010) $[\bar{1}00]$	1 (a)	X				X	1.40		X		X		1.18
(Twin Shear)	1 (b)	X				X	1.40		X		X		1.18
	2 (a)	X				X	1.40		X		X		1.18
	2 (b)	X				X	1.40		X		X		1.18
(010) [101]	1 (a)	X		X			4.61		X		X		4.91
	1 (b)	X				X	0.31		X		X		0.56
(011) $[01\bar{1}]$	1 (a)	X				X	0.60		X		X		0.59
	1 (b)	X		X			0.05		X		X		0.61
(101) $[\bar{1}01]$	1 (a)	X				X	0.03		X		X		0.61
	1 (b)	X		X			0.64		X		X		0.59
$(\bar{1}11)$ $[01\bar{1}]$	1 (a)	X				X	0.74		X		X		0.79
	1 (b)	X		X			0.05		X		X		0.73
Lattice Correspondence C											$[0\bar{1}0]$		
(110) $[\bar{0}01]$	1 (a)	X		X			3.15	X			X		5.50
	1 (b)	X		X			0.43	X			X		0.45
(110) $[\bar{1}10]$	1 (a)		X			X	0.07	X			X		0.74
	1 (b)	X		X			0.72	X			X		0.72
(101) $[\bar{1}01]$	1 (a)		X			X	0.74	X			X		0.73
	1 (b)	X		X			0.05	X			X		0.72
$(\bar{1}11)$ [110]	1 (a)	X		X			1.00	X			X		1.48
	1 (b)		X			X	0.07	X			X		0.65

Figure Captions

Figure 1. Crystal structures of monoclinic and tetragonal zirconia with lattice parameters at 950°C for both phases. Monoclinic twin planes(5) are (100),(110) and ($1\bar{1}0$) while slip occurs on(010).

Figure 2. Lattice correspondences for zirconia.

Figure 3. Flow chart illustrating method of calculations.

Figure 4. The relation between shape deformation, angle of shear and habit plane.

Figure5. The determination of magnitudes and directions of principle strains by a coordinate geometry method.

ZIRCONIA

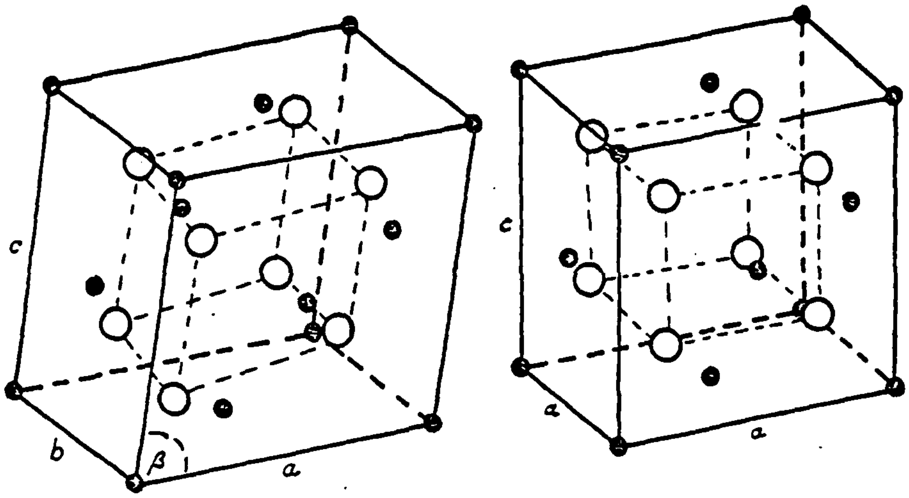

MONOLINIC
a_m = 5.1881 Å
b_m = 5.2142 Å
c_m = 5.3835 Å
β = 81.22°

TETRAGONAL
a_t=5.1485 Å
c_t= 5.2692 Å

Fig.1. Lattice parameters at 950°C for monoclinic and tetragonal Monoclinic twin planes (Bailey, 1964): (100),(110), (1$\bar{1}$0) slip planes: (010)

LATTICE CORRESPONDENCES FOR ZRO_2

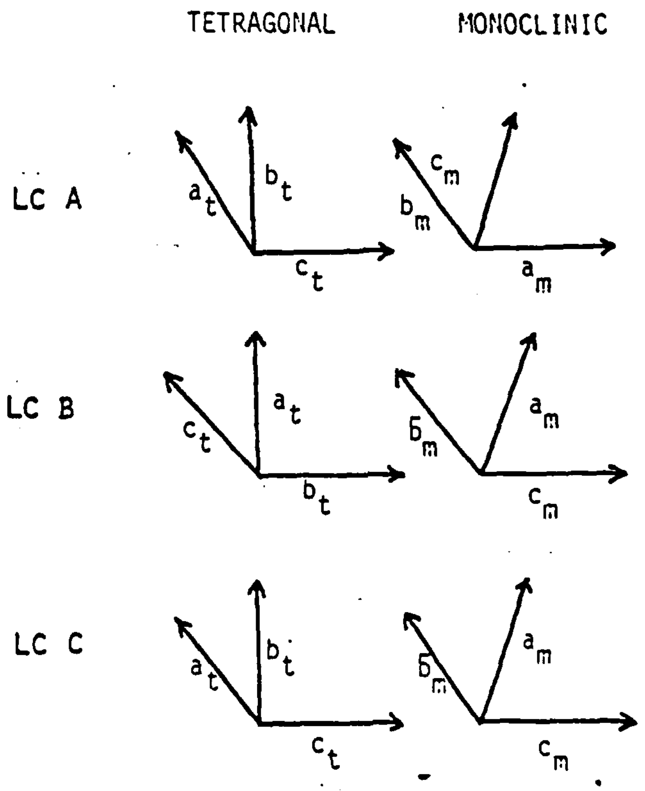
TETRAGONAL
MONOCLINIC
LC A
a_t
b_t
c_t
c_m
b_m
a_m
LC B
c_t
a_t
b_t
$\bar{b}_m$
a_m
c_m
LC C
a_t
b_t
c_t
$\bar{b}_m$
a_m
c_m

Fig.2.

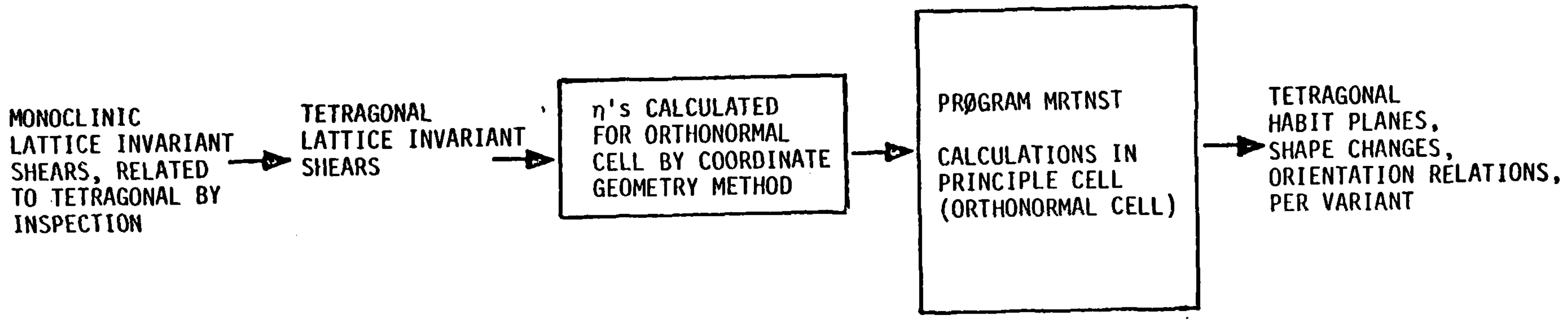
MONOCLINIC
LATTICE INVARIANT
SHEARS, RELATED
TO TETRAGONAL BY
INSPECTION
TETRAGONAL
LATTICE INVARIANT
SHEARS
η's CALCULATED
FOR ORTHONORMAL
CELL BY COORDINATE
GEOMETRY METHOD
PRØGRAM MRTNST
CALCULATIONS IN
PRINCIPLE CELL
(ORTHONORMAL CELL)
TETRAGONAL
HABIT PLANES,
SHAPE CHANGES,
ORIENTATION RELATIONS,
PER VARIANT

Figure 3.

RELATIONS BETWEEN SHAPE DEFORMATION, ANGLE OF SHEAR, AND HABIT PLANE

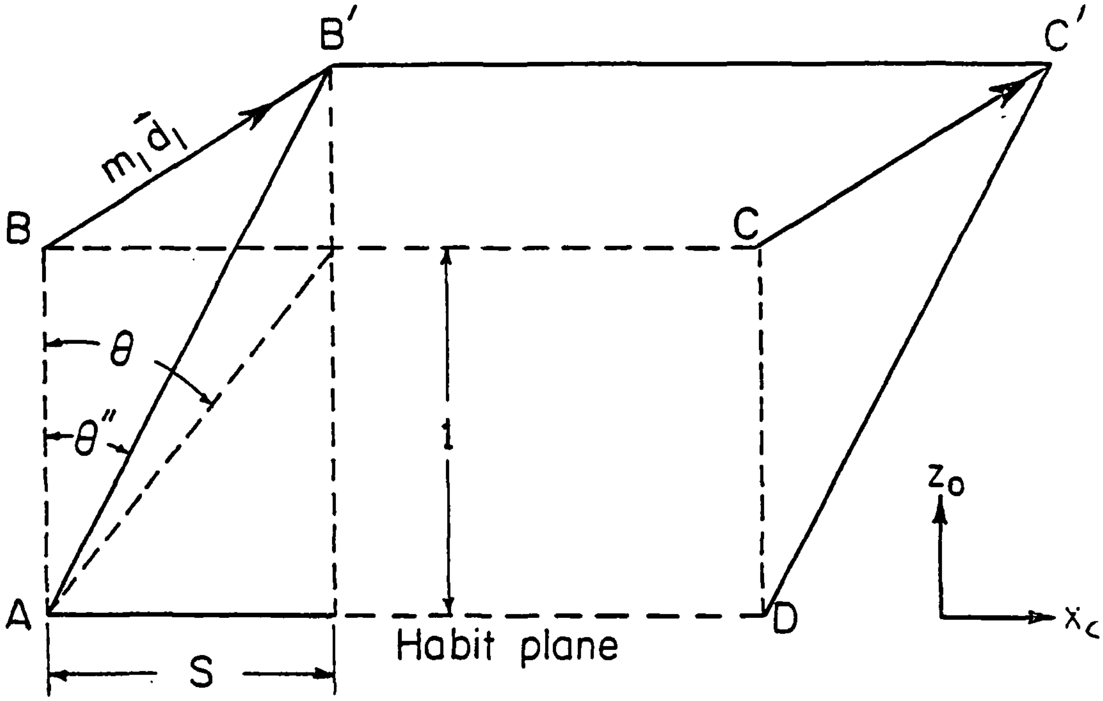
B′
C′
$m_1 \bar{d}_1$
B
C
θ
θ″
1
z_0
A
D
x_c
Habit plane
S

FIG. 4

APPENDIX I

The Determination of Directions and Magnitudes
Of Principal Distortions for the
Tetragonal → Monoclinic Phase Transformation
in Zirconia (ZrO_2)

Directions and magnitudes of the principal distortions associated with the three possible lattice correspondences between tetragonal and monoclinic zirconia have been determined by the method of analytical geometry.

The problem is two dimensional as one principal axis is obtained directly by inspection (Fig 2 , $n_3//b_m$). The remaining two principal distortions must lie in the plane of which the n_3 direction is the normal. The theory of finite homogeneous strain in two dimensions (e.g. Jaeger(13)) gives a simple method for the location of these two vectors:

The changes in the relevant tetragonal plane can be factorised into (a) a change of dimensions (expansion/contraction) and (b) a change of shape (simple shear). This is illustrated in figure 5

Consider a point (x,y) in the tetragonal plane:

(i) $x \rightarrow \frac{x_m}{x_t} x$, $y \rightarrow \frac{y_m \sin \beta}{y_t} y$ (by expansion)

$(x \rightarrow ax)$ $(y \rightarrow dy)$

(ii) $ax \rightarrow ax + \tan (90 - \beta) dy$, dy unchanged (by shear)

$(ax \rightarrow ax + by)$ $(dy \rightarrow dy)$

Hence $x \rightarrow \frac{x_m}{x_t} x + \tan (90 - \beta) \frac{y_m \sin \beta}{y_t} y$

$(x \rightarrow ax + by)$

and $y \rightarrow \frac{y_m \sin \beta}{y_t} y$

$(y \rightarrow dy)$

From two dimensional strain theory, for x → ax + by and y → cx + dy directions of the principal distortion axes are given by :

$$\tan 2\alpha = \frac{2\,(ab + cd)}{a^2 + c^2 - b^2 - d^2} = \frac{2ab}{a^2 - b^2 - d^2}$$

(since c = o in this case).

(α is the angle made with the x axis, and the required angles are α, $\alpha + \Pi/2$).

Magnitudes (A, B) are given by:

$$(A + B)^2 = (a + d)^2 + (b - c)^2 = (a + d)^2 + b^2$$

$$(A - B)^2 = (a - d)^2 + (b + c)^2 = (a - d)^2 + b^2$$

Directions of the principal distortion axes in the monoclinic phase can also be determined:

$$\tan 2\alpha' = \frac{2\,(ac + bd)}{a^2 + b^2 - c^2 - d^2} = \frac{2bd}{a^2 + b^2 - d^2}$$

(α', $\alpha' + \Pi/2$ are the angles formed by the principal distortion axes and the x axis).

Rotation of the principal axes during the deformation is therefore ($\alpha' - \alpha$).

These formulae can be applied to tetragonal $\rightleftarrows$ monoclinic, orthorhombic $\rightleftarrows$ monoclinic and cubic $\rightleftarrows$ monoclinic changes.

The Determination of Directions and Magnitudes
Of Principal Distortions for the
Tetragonal → Monoclinic Phase Transformation
in Zirconia (ZrO_2)

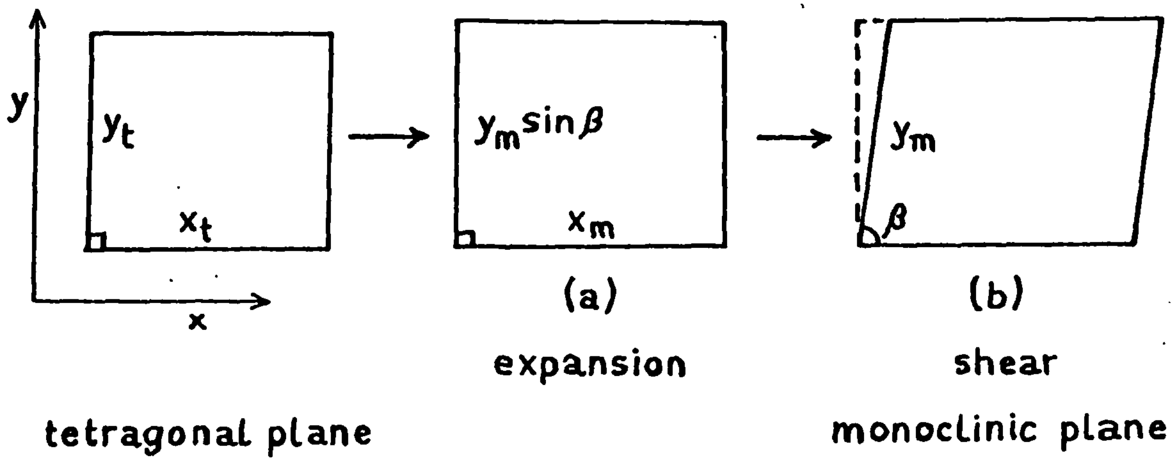
y
y_t
x_t
x
tetragonal plane
$y_m \sin\beta$
x_m
(a)
expansion
y_m
β
(b)
shear
monoclinic plane

Figure 5

CHAPTER VIII

WEAR MECHANISMS IN CERAMICS

by

A. G. Evans and D. B. Marshall

Department of Materials Science and Mineral Engineering,
University of California,
Berkeley, CA 94720

WEAR MECHANISMS IN CERAMICS

A. G. Evans and D. B. Marshall

Department of Materials Science and Mineral Engineering,
University of California,
Berkeley, CA 94720

ABSTRACT

The mechanisms of material removal during wear have been examined. Primary emphasis has been placed on the lateral fracture mechanism, in an attempt to elucidate both its realm of importance and the concomitant material removal rates. Correlations with existent data are shown to be encouraging. The enhancement of material removal by heat generation in the plastic zone has been examined and shown to be generally of minor significance. Some considerations of material removal below the fracture threshold have also been presented.

I. INTRODUCTION

The wear of ceramics has been the subject of extensive empirical investigation[1]. For example, material removal rates have been measured on various materials as functions of the normal force, the horizontal (frictional) force, the wheel speed, etc. However, the detailed mechanisms of material removal have only been cursorily explored. Yet, some understanding of mechanisms is an essential prerequisite to the development of optimum wear characteristics (especially for complex processes such as abrasive wear). The intent of the present paper is to examine possible mechanisms of material removal.

Several investigators[2-4] have recently recognized the important role of lateral fracture (fig. 1a) in material removal. This mechanism of wear is explored in some detail, to determine both its realm of importance and the parameters that might influence the removal rate.

Lateral cracking occurs above a threshold force[5,6]. This threshold coincides with a transition from a relatively severe lateral fracture dominated material removal process at higher force levels to other less damaging wear mechanisms. The fracture threshold is thus an important concept in the study of wear, and the nature of the threshold should be afforded appreciable emphasis. The material removal mechanism below the fracture threshold is presently uncertain. An operative (although not necessarily exclusive) mechanism involves the plastic cutting that occurs during the grooving process (fig. 1b).

The material removal rate above the fracture threshold evidently depends on the extent of the lateral fracture. An analysis of lateral crack extension will thus be used to predict wear rates as a function of the dominant material variables. Data for a range of materials will be correlated with the predictions.

The plastic flow associated with surface penetration must lead to a local temperature increase. This temperature rise inevitably results in thermal stresses, that enhance the extension of the lateral cracks. The importance of thermal effects vis-a-vis residual stress motivated lateral fracture is examined in the third section of the paper. Then, some considerations of material removal below the fracture threshold are presented. Finally, some general implications for the development of wear resistant materials are discussed from the perspective provided by the present analyses.

2. THE LATERAL FRACTURE MODEL

2.1 *The Threshold*

The fracture threshold is a phenomenon with major significance for the control of wear, because it signifies a change in wear mechanism and a concommitant order-of-magnitude increment in wear rate. The general characteristics of fracture thresholds, at sites of plastic penetration, are reasonably well comprehended[5,6,7], although detailed quantitative predictions are subject to some uncertainty. Of particular interest to the wear mechanism transition is the minimum threshold load P^*. This threshold load pertains in the presence of an adequate spatial density of crack precursors.in the vicinity of the plastic zone[6]; a situation that is expected to prevail near surfaces subject to wear damage. The minimum threshold is dictated by the hardness H, toughness K_c and elastic modulus E of the material, in accord with the relation

$$P^{*} = \zeta \left(\frac{K_c^{4}}{H^{3}}\right) f\ (E/H) \qquad (1)$$

where the function $f(E/H)$ and the constant ζ depend upon the type of crack. For lateral cracks, recent analysis[6] indicates that f is insensitive to E/H and that $\zeta f \approx 2 \times 10^{5}$. Threshold predictions for lateral fracture in several important material systems are summarised in Table I. The threshold load levels are relatively low, but loads of this magnitude can exist at individual wear particles: depending upon the nature of the wear medium, the contact points and the constraints imposed on the wear system. There have been few experimental studies of lateral fracture initiation and validation of the predicted threshold characteristics is not possible at this juncture. Such studies are now in progress. However, it is noted that predictions of the radial fracture threshold using the same analytic procedures are in good accord with the more comprehensive experimental observations that exist for this system[6,7].

2.2 *The Lateral Crack Extension*

Lateral cracks develop exclusively due to the residual stress created by indentation[8]. The maximum extension of the crack is thus realised when the penetrating particle is removed. The cracking behavior can be analysed by regarding the plastic zone as a precompressed spring which motives crack extension[9,10]. The crack advance is then dictated by the compliance of the material above the crack, treated as an elastic cantilever. The specific crack extension depends, in part, upon the morphology of the plastic penetration. For axisymmetric indentation (most pertinent to intermittent particle contact) the lateral crack length c is given by[10];

$$c = c^{L}\left[1 - (P_0^{*}/\hat{P})^{1/4}\right]^{1/2} \qquad (2)$$

where $\hat{P}$ is the peak load during particle penetration, P_0^{*} is an apparent threshold load for fully developed cracking and c^{L} is given by;

$$c^{L} = \alpha_1 \left(\frac{(E/H)^{2/5}}{K_c^{1/2} H^{1/8}}\right) \hat{P}^{5/8} \qquad (3)$$

where α_1 is a material independent constant that depends on the particle shape and can be determined by calibration on a material with well characterised fracture properties (e.g. glass). For a linear plastic groove (as might pertain for continuous particle penetration) the equivalent result (Appendix, eqn A-9) is;

$$c^{L} = \alpha_2 \left[\frac{(E/H)^{3/5}}{K_c^{1/2}\ H^{1/8}}\right] \hat{P}^{5/8}$$

where α_2 is another material independent constant $(\alpha_2 \approx \alpha_1)$. The only significant difference between the two solutions for c^{L} occurs in the (E/H) exponent. But, since the range of E/H values for most ceramics is less than an order of magnitude, the influence of the grinding morphology upon crack extension is considered to be of minor importance.

For present purposes, the indentation forces are considered to be sufficiently in excess of the apparent threshold to permit the direct use of eqn. (3) for the prediction of crack extension. The wear behavior under these conditions will exhibit relatively simple functional dependencies on the dominant material variables (as described in the subsequent section). The predictions can thereupon be straightforwardly correlated with experimental results. The cracking behavior at intermediate loads is less extensive than that predicted from eqn. (3) and hence, the wear predictions based on eqn. (3) represent an upper bound wear rate. A more complete analysis of crack extension at intermediate loads can be conducted if experimental correlations indicate that some important trends are inadequately predicted by neglect of the apparent threshold.

The above solutions for the lateral crack length pertain to conditions wherein all of the plastically deformed material is retained within the plastic zone and thus represent an upper bound crack driving force. When some of the plastically deformed material is removed by plastic cutting, the residual forces will be reduced and hence, the lateral crack extension diminished. It is not known at this juncture whether the relative alleviation of the residual forces by cutting exhibits important material dependencies. Such effects would emerge from inadequate correlations of experimental results (between materials) with models based on eqn. (3).

2.3 *The Material Removal Rate*

The material removal analysis considers the extension of the lateral cracks normal to the motion of the abrading particle (fig. 1a), since this distance defines the width of the potential material removal zone. The situation to be modelled is defined in fig. 1a; it consists of an abrasive particle subject to a normal force P_n, moving with a prescribed lateral velocity v_ℓ.

The volume V_i of material removed by the passage of each abrasive particle that exceeds the fracture threshold force P^* is determined by the extent c_i and the depth h_i of the lateral fracture. The upper bound volume removal is;

$$\hat{V}_i = 2h_i c_i \ell_i \tag{4}$$

where ℓ_i is the distance of motion. The lateral fracture depth typically scales with the plastic zone radius b [6,10], which, in turn, relates to the plastic penetration radius, a, by[6]

$$b \sim a\,(E/H)^{2/5} \quad , \tag{5}$$

and the indentation radius is related to the hardness and the peak normal penetration force by

$$a^2 \sim (\hat{P}_n/H) \tag{6}$$

Substituting eqns. (3), (5) and (6) into eqn.(4), the volume removed becomes;

$$\hat{V}_i = \alpha_3 \frac{\hat{P}_n^{9/8}}{K_c^{1/2}\, H^{5/8}} (E/H)^{4/5}\, \ell_i \tag{7}$$

where α_3 is a material independent constant.

Implicit in the preceding analysis is the dominant influence of the normal force P_n upon the material removal process. The lateral force $P_\ell = \mu P_n$ (presumed to be dictated by the resistance of the material to plastic grooving, i.e. ductile cutting resistance) is considered incidental to material removal by lateral fracture. Some substantiation of this premise will emerge later from experimental correlations. At this juncture, it is noted that, by analogy with the equivalent elastic problem[11], the lateral force may tend to rotate the stress field in the direction of P_ℓ, in the sense that the tension is enhanced behind the contact zone and suppressed ahead of the contact. However, even if this occurs, there should be no appreciable influence on the stresses contained in the plane normal to P_n ; stresses which have the primary effect on lateral crack extension. Hence under quasi-static conditions, the width of the lateral fracture zone should be relatively insensitive to the magnitude of the lateral force.

At relatively high lateral velocities, local instabilities tend to develop. These instabilities presumably occur following a fracturing event and result in an abrubt increase in the local particle velocity, as manifest in the lateral force oscillations typically observed in studies of the motion of abrading particles. The impact events that result from the instabilities are likely to have impulse components both normal and parallel to the surface. The normal component affects the penetration, and thus has the more significant influence on the material removal process. The normal velocity, and the consequent magnitude of the lateral fracture, may depend upon the amplitude of the instability and hence, indirectly upon the friction coefficient. These complexities may be of secondary significance, and the existence of dynamic effects should be sought in experimental results before embarking on an analytic study of the role of friction in the wear process.

2.4 *Correlations With Experiment*

Experimental results suitable for correlation with the present wear predictions include measurements of the influence of the normal force on the wear rate (observed for a specific material) and, more significantly, studies of the trends in the wear rate among different materials. The influence of material properties on wear can be compared with the lateral fracture model either from measurements of the wear forces at a specified (constant) volume rate of removal, or from removal rates at a constant level of applied force.

Direct measurements of the lateral crack width have been conducted on MgZn ferrite as a function of the normal force[3]. These results are consistent with the force exponent of 5/8 predicted for the lateral crack extension (fig. 2). The influence of the normal force on the volume removal rate has been studied for several materials by Wilshaw and Hartley[12]. These results (fig. 3) indicate a force exponent that exceeds unity, as anticipated by the present analysis (eqn. (7)). The experimentally observed exponent ranges between 1.07 and 1.3: values which compare quite favorably with the predicted value of 1.13.

The most comprehensive material removal data suitable for comparison with the present predictions are grinding data obtained by Koepke and Stokes[13]. These data comprise force measurements determined on different materials for constant volume removal conditions. For up-grinding conditions, which best simulate the behavior analysed in the preceding section (because fracture chips are directly ejected from the system), the force data for a wide range of materials (fig. 4) are in remarkable accord with the predicted material dependence, $K_c^{-1/2} H^{-5/8}$. The superior correlation exists for the dependence on the normal force; while, a more modest correspondence obtains for the lateral force. These relative correlations tend to substantiate that the development of a lateral force is incidental to the material removal process. The one material that deviates from the correlation is lucalox Al_2O_3. This is a relatively coarse grained Al_2O_3 that also exhibits unusual indentation fracture characteristics[14]. Under indentation conditions extensive grain boundary separation occurs, rather than the formation of discrete crack systems. Grinding in this (and similar) materials could thus procede by grain ejection and hence, the material removal would be expected to exhibit a different dependence on material properties than anticipated by the lateral fracture model.

Machining data at constant force are also available for a range of materials[15]. However, the data exhibit an appreciable grain size dependence. This behavior presumably arises because the lateral fracture in the coarser grained materials extends over a relatively small number of grains and hence, the K_c and H values required for the volume removal predictions are smaller than the isotropic polycrystalline values. It is expedient, therefore, to conduct the comparison at the small extreme of grain size for which available polycrystalline material parameters are most likely to pertain. The resultant correlation is summarised in fig. 5. The correct trends are predicted by the material parameter, $K_c^{-1/2} H^{-5/8}$, although the correlation is not as satisfying as that evident for the force measurements.

The relatively consistent trends in both the material removal rate and the grinding forces with the material parameters suggested by the simple lateral crack analysis indicates that most of the proposed complexities, if they occur, do not impose additional material dependent influences upon the wear process[†]. Dynamic effects and residual force relaxation by plastic removal can presumably, therefore, be considered to introduce only small perturbations upon the wear characteristics anticipated from the quasi-static lateral fracture analysis, at least for the test conditions used and for materials within the range of properties encompassed by the existent experimental results.

[†] Recent abrasive wear studies reported by Moore and King[16] indicate a poor experimental correlation based on $K_c^{5/8}H^{1/2}$. However, the toughness values determined in the analysis are substantially inaccurate (e.g. 3.8 $\mathrm{MPa}\sqrt{m}$ for soda lime glass compared with a generally accepted value of 0.7 $\mathrm{MPa}\sqrt{m}$: 9.1$\mathrm{MPa}\sqrt{m}$ for Si_3N_4 compared with 4-5 $\mathrm{MPa}\sqrt{m}$ etc.) Reanalysis of their results is thus needed before embarking on an assessment of the inadequacies of the simple lateral fracture model.

3. THERMAL EFFECTS

Heat is invariably generated during a grinding operation. This heat derives from the plastic work expended by the penetration of the abrading particle. The heat is generated within the plastic zone and leads to an expansion of this zone vis-a-vis the surrounding elastic material. The zone expansion is directly analagous to the effective expansion induced by plastic penetration[9,10]. Hence, heat generation can be considered to yield a lateral crack driving force that simply superimposes on that associated with the residual indentation field. The ratio of crack driving forces attributed to these two sources of zone expansion will determine their relative influence upon the wear rate, by lateral fracture. Additionally, it is noted that the zone expansion induced by heating creates shear stresses outside the isothermal plastic zone. These stresses tend to enlarge the plastic zone, increasing its volume from V to V^*. This zone enlargement also contributes to the crack driving force ratio.

The work done in creating an indentation of volume ΔV is simply, $H\Delta V$[6]. If this work is dissipated as heat within the plastic zone, the average temperature rise θ for adiabatic conditions is

$$\theta = H\Delta V/\rho c_p V^* \tag{8}$$

where ρ is the density and c_p is the specific heat. The local temperature rise ΔT at a radial location r is related to the average temperature θ by[17];

$$\Delta T = 3\theta \ln(b/r) \tag{9}$$

The adiabatic unconstrained volume strain is thus[†],

$$\begin{aligned} e_T &= 3\alpha \int_0^b (r/b)^3 d\Delta T \\ &= \left(\frac{3\alpha H}{\rho c_p}\right) \left(\frac{\Delta V}{V^*}\right) \end{aligned} \tag{10}$$

where α is the linear thermal expansion coefficient. Since $\Delta V/V$ is the unconstrained volume strain of isothermal plastic penetration, the adiabatic crack driving force ratio becomes;

$$R \equiv e^T/(\Delta V/V) = (3\alpha H/\rho c_p)(V^*/V) \tag{11}$$

Inserting some typical values for the material parameters ($H \sim 10\text{GPa}$, $a \sim 5 \times 10^{-6}\text{K}^{-1}$, $\rho \sim 3 \times 10^3\text{Kgm}^{-3}$, $c_p \sim 600\text{JKg}^{-1}\text{K}^{-1}$) indicates that R is ~ 0.1 when $V^* \approx V$. Usually, therefore, thermal effects would be expected to exert a minor influence on the wear rate. A significant thermal effect may emerge, however, in hard materials that exhibit a large thermal expansion coefficient and a low specific heat.

4. SUB THRESHOLD WEAR RATES

Below the lateral fracture threshold, material is removed by a plastic cutting process (fig. 1b). The material removal rate is presumably dictated by the plastic penetration and should thus be uniquely related to the material hardness, the normal force and the particle geometr ;

[†] It is noted that the assumption of a uniform temperature rise θ within the plastic zone yields an identical result.

$$V_i \sim \frac{\hat{P}_n \ell_i}{H} \cot(\Psi/2) \tag{12}$$

where Ψ is the included angle of the penetrating particle. The volume removal rate induced by plastic cutting is about an order of magnitude smaller than that associated with the lateral fracture mechanism[16]. Appreciable wear resistance is thus experienced with this regime. The choice of wear conditions that exclude lateral fracture is evidently a highly desirable material/design objective.

5. IMPLICATIONS AND CONCLUSIONS

The analyses of fracture dominated wear processes in brittle solids indicates a reasonably good correlation with available experimental data. This correlation substantiates the strong importance of both the fracture toughness and the hardness upon the wear rate: high toughness and high hardness both being desirable for optimum wear resistance. A small influence of the material's thermal parameters is also anticipated, but only for hard materials with a large thermal expansion coefficient or a small specific heat.

A major diminution in wear rate is associated with force levels below the fracture threshold. The force at the fracture threshold is strongly influenced by both the hardness and the toughness, such that fracture can be suppressed by a high toughness or a low hardness. Below this threshold, the material removal rate is substantially diminished and depends principally upon the hardness.

In general, materials with an optimum combination of high toughness and high hardness will be the most wear resistant. However, there is some ambiguity associated with the role of the hardness. Although a high hardness minimizes the wear rate both below and above the fracture threshold, the threshold force is diminished by an increase in hardness. Situations can arise, therefore, when a hardness increase in the vicinity of the threshold leads to an enhanced wear rate, as depicted in fig. 6.

The influence of the fracture toughness also requires some qualification. The toughness needed to resist lateral fracture must be developed on the appropriate scale. Specifically, the microstructural scale must be appreciably smaller than the length of the lateral fracture in order to experience the macroscopic fracture toughness. Some important effects of the dominant microstructural size (e.g. the grain size) are thus to be anticipated, especially at force levels in the vicinity of the threshold. These effects will require more detailed consideration on an individual basis.

ACKNOWLEDGMENT

The authors express their appreciation for the financial support of this research provided by the Office of Naval Research under contract no. N0014-79-C-0159.

APPENDIX

LATERAL CRACK EXTENSION

Consider a two-dimensional lateral crack configuration created by a linear groove of length ℓ . The strain energy release rate is

$$= (P_r^2/2\ell)\, d\lambda/dc \qquad \text{(A-1)}$$

where P_r is the residual normal force exerted by the plastic zone on the surrounding elastic material, λ is the compliance of the elastic layer above the crack, and c is lateral crack length. Linear elasticity requires that[10]

$$P_r = P_r^o[1-u_r/u_r^o] \qquad \text{(A-2)}$$

where P_r^o is the initial residual force (at zero crack length), u_r is the opening displacement at the crack center, and u_r^o is the opening displacement when the driving force relaxes to zero. For well developed cracks (c>>h where h is the depth of the lateral fracture) the compliance may be well approximated by[†]

$$\lambda = 4c^3/E\ell h^3 \qquad \text{(A-3)}$$

Combining eqns. (A-1), (A-2) and (A-3), the stress intensity factor becomes;

$$K \equiv \left(\frac{E\mathcal{G}}{1-\nu^2}\right)^{1/2} = \left[\frac{6}{1-\nu^2}\right]^{1/2} \frac{cP_r^o}{\ell h^3(1+\beta c^3)} \qquad \text{(A-4)}$$

[†] Eqn. (A-3) is the standard solution for a thin elastic cantilever. The cantilever in the present model is disproportionately wide and may not extend to the edges of the material. The major influences of these deviations from ideal geometry are expected to be reflected in the numerical factor in eqn. (A-3) and in the introduction of a Poisson's ratio dependence.

where $\beta = (P_r^o/u_r^o)(4/E\ell h^3)$. Equating K to the critical value K_c, the lateral crack length becomes;

$$1 + \beta c^3 = [\bar{\omega}/(1-\nu^2)]^{1/2} P_r^o c/\ell K_c h^{3/2} \tag{A-5}$$

which, to the same level of approximation used in eqn (3a), is

$$c \approx [\bar{\omega}/(1-\nu^2)]^{1/4} (Eh^{3/2}u_r^o/4K_c)^{1/2} \tag{A-6}$$

Noting that (from eqns 5 and 6)

$$h \sim b \approx (E/H)^{2/5} (\hat{P}/H)^{1/2} \tag{A-7}$$

and that[9,10]

$$u_r^o \sim \Delta V/\ell b \sim a^2/\ell b$$

$$\approx (H/E)^{2/5} (P/H)^{1/2}, \tag{A-8}$$

the lateral crack length becomes

$$c \sim \frac{(E/H)^{3/5}\ \hat{P}^{5/8}}{H^{1/8}\ K_c^{1/2}}, \tag{A-9}$$

as in eqn. (3b).

REFERENCES

1. P. J. Gielisse and J. Stanisloa, The science of ceramic machining and surface finishing, NBS Special Technical Publication, 348, 5 (1972).
2. M. V. Swain, Fracture mechanics of ceramics (Ed. R. C. Bradt, D. P. H. Hasselman and F. F. Lange), Plenum, NY, 3, 257 (1978).
3. J. D. B. Veldkamp, N. Hattu and V. A. C. Snyders, Fracture mechanics of ceramics, 3, 273, (1978).
4. A. G. Evans and T..R. Wilshaw, Acta Met., 24, 939 (1976).
5. B. R. Lawn and A. G. Evans, Jnl. Mater. Sci. 12, 2195 (1977).
6. S. S. Chiang, D. B. Marshall and A. G. Evans, to be published.
7. J. Lankford and D. L. Davidson, Jnl. Mater. Sci., 14, 1662 (1979).
8. B. R. Lawn and M. V. Swain, Jnl. Mater. Sci. 10, 113 (1975).
9. B. R. Lawn, A. G. Evans and D. B. Marshall, Jnl. Amer. Ceram. Soc., in press.
10. D. B. Marshall, B. R. Lawn and A. G. Evans, to be published.
11. G. M. Hamilton and L. E. Goodman, Jnl. Appl. Mech., 33, 371 (1966).
12. T. R. Wilshaw and H. E. W. Hartley, (Proc. Third European Symposium on Comminution), Chemia GMBH, Weinheim/Bergestrasse, (1972).
13. B. G. Koepke and R. J. Stokes, Science of Ceramic Machineing and Surface Finishing, NBS Special Technical Publication, 562, 75 (1979).
14. A. G. Evans, ASTM STP, 678 (1978) 112.
15. R. W. Rice and B. K. Speronello, Jnl. Amer. Ceram. Soc. 59, 330 (1976).
16. M. A. Moore and F. S. King, Wear, 60, 123 (1980).
17. B. R. Lawn, B. J. Hockey and S. M. Wiederhorn, Jnl. Amer. Ceram. Soc., 63, 356 (1980).

TABLE I

LATERAL CRACK NUCLEATION ESTIMATES[†]

Material	Toughness (MPa$\sqrt{m}$)	Hardness (GPa)	Threshold (N)
Al_2O_3	2.2	20	0.4
Glass	0.7	6	0.2
MgO	1.1	8	0.9
Si_3N_4	5 (polycrystal)	16	31
Si_3N_4 (estimate)	~2 (single crystal)	16	~0.8

[†] The threshold in most brittle materials occurs at load levels wherein the scale of the cracks is on the order of (or smaller than) the grain size[6]. Single crystal values of toughness are thus pertinent unless the material is particularly fine grained. The thresholds are thus based on single crystal toughness levels unless otherwise stated.

FIGURE CAPTIONS

Fig. 1. A schematic indicating the mechanisms of material removal by (a) lateral fracture and (b) plastic cutting.

Fig. 2. The influence of the normal force on the extent of lateral fracture[3].

Fig. 3. The effect of the applied force on the material removal[12].

Fig. 4. A correlation of grinding forces at constant removal rates[13] with the toughness, hardness parameter predicted by the present analysis. The toughness values are in $MPa\sqrt{m}$ and the hardness values are the the Knoop hardness.

Fig. 5. A correlation of material removal rates at constant force[15] with the toughness, hardness parameters predicted by the present analysis.

Fig. 6. A schematic indicating the wear rate as a function of normal force in two materials with a different hardness H but comparable levels of toughness K_c and of E/H.

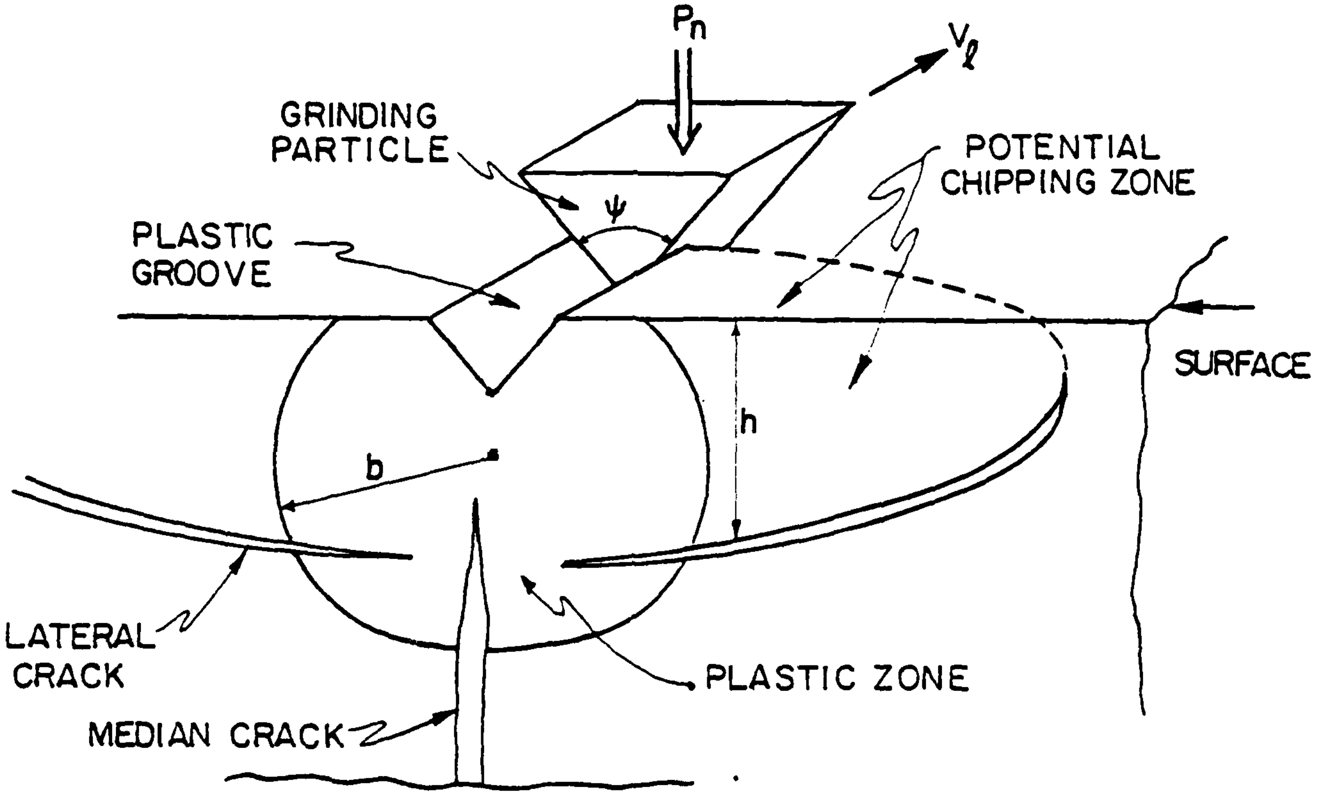
Pn
Vℓ
GRINDING PARTICLE
POTENTIAL CHIPPING ZONE
ψ
PLASTIC GROOVE
SURFACE
h
b
LATERAL CRACK
PLASTIC ZONE
MEDIAN CRACK

(a) LATERAL FRACTURE MECHANISM

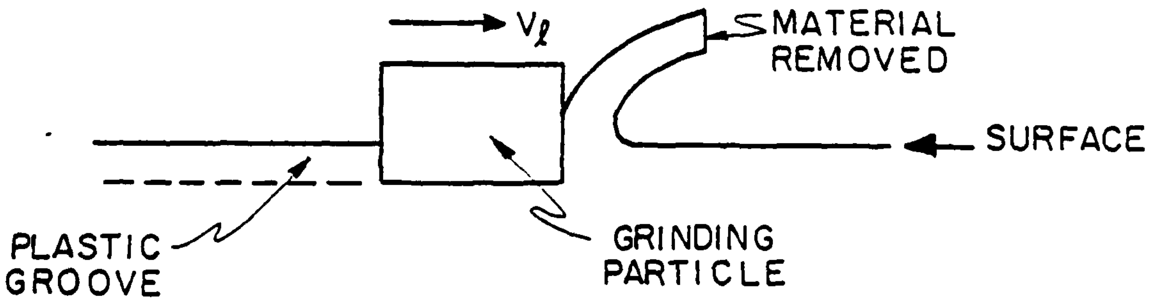
Vℓ
MATERIAL REMOVED
SURFACE
PLASTIC GROOVE
GRINDING PARTICLE

(b) PLASTIC GROOVING MECHANISM

XBL 8011-6355

Fig. 1

AD-A098 966   CALIFORNIA UNIV BERKELEY DEPT OF MATERIALS SCIENCE A--ETC   F/G 11/2
IMPACT DAMAGE AND EROSION OF CERAMICS AND COMPOSITES.(U)
DEC 80   A G EVANS, N BURLINGAME, S S CHIANG   N00014-79-C-0159

UNCLASSIFIED   NL

3 of 3
AD
A098966

END
DATE
FILMED
8-81
DTIC

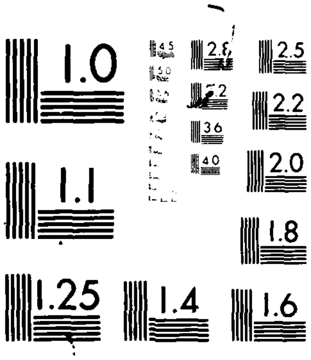
1.0
4.5
5.0
5.6
2.8
3.2
3.6
4.0
2.5
2.2
2.0
1.1
1.8
1.25
1.4
1.6

MICROCOPY RESOLUTION TEST CHART
NATIONAL BUREAU OF STANDARDS 1963 A

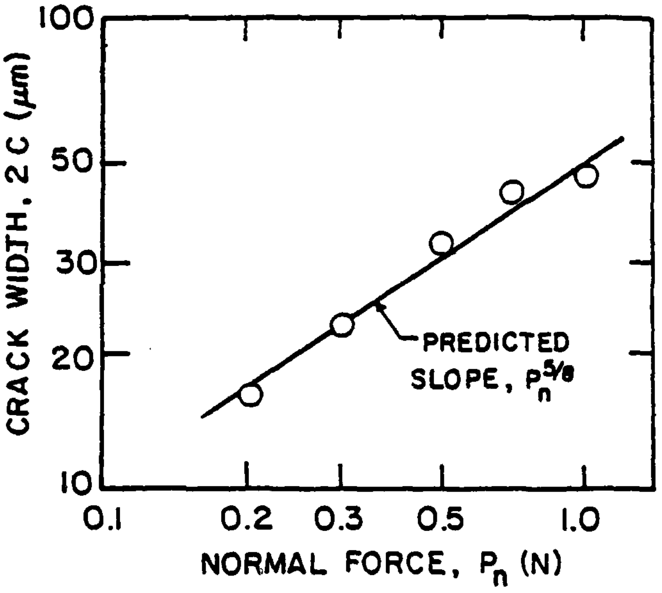

XBL8011-6359

Fig. 2

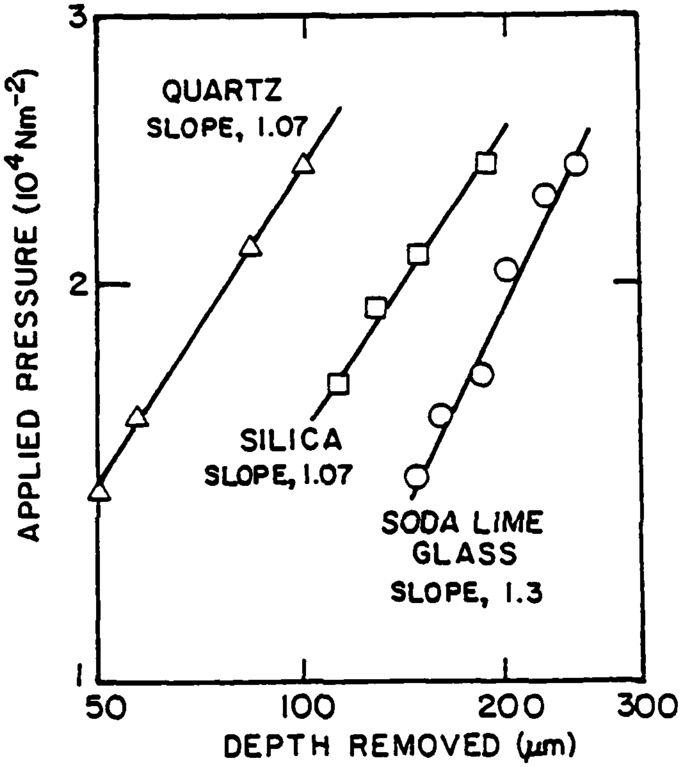

XBL8011-6357

Fig. 3

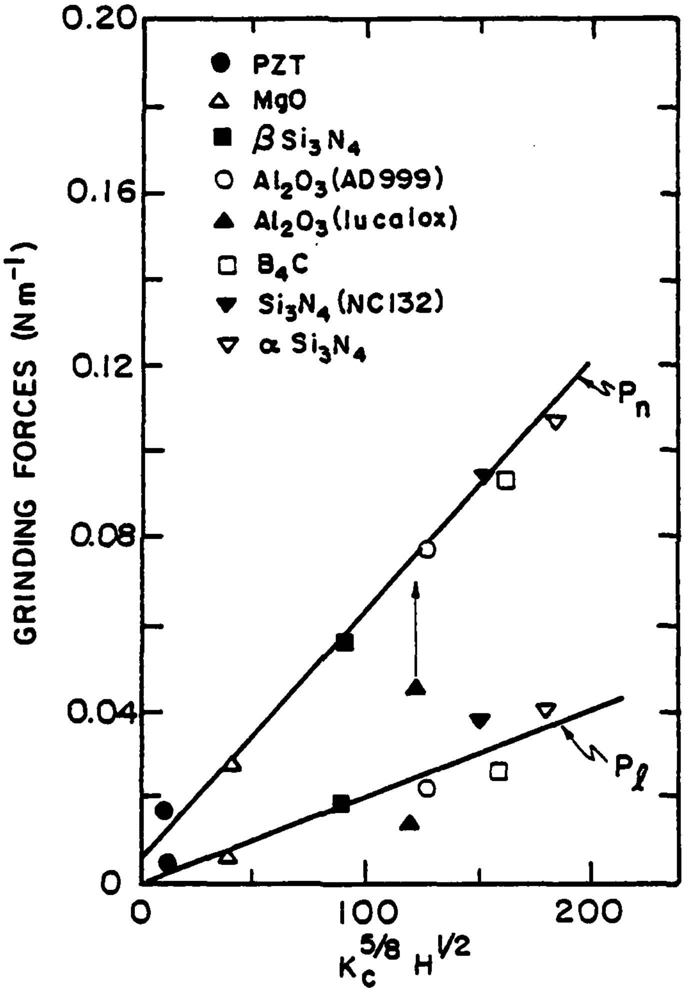

XBL8011-6360

Fig. 4

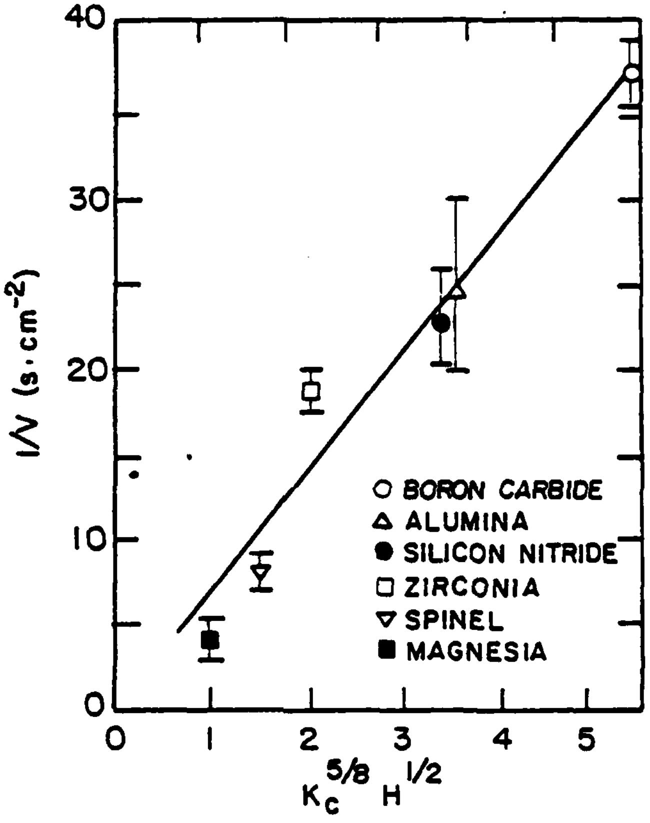

XBL 8011-6358

Fig. 5

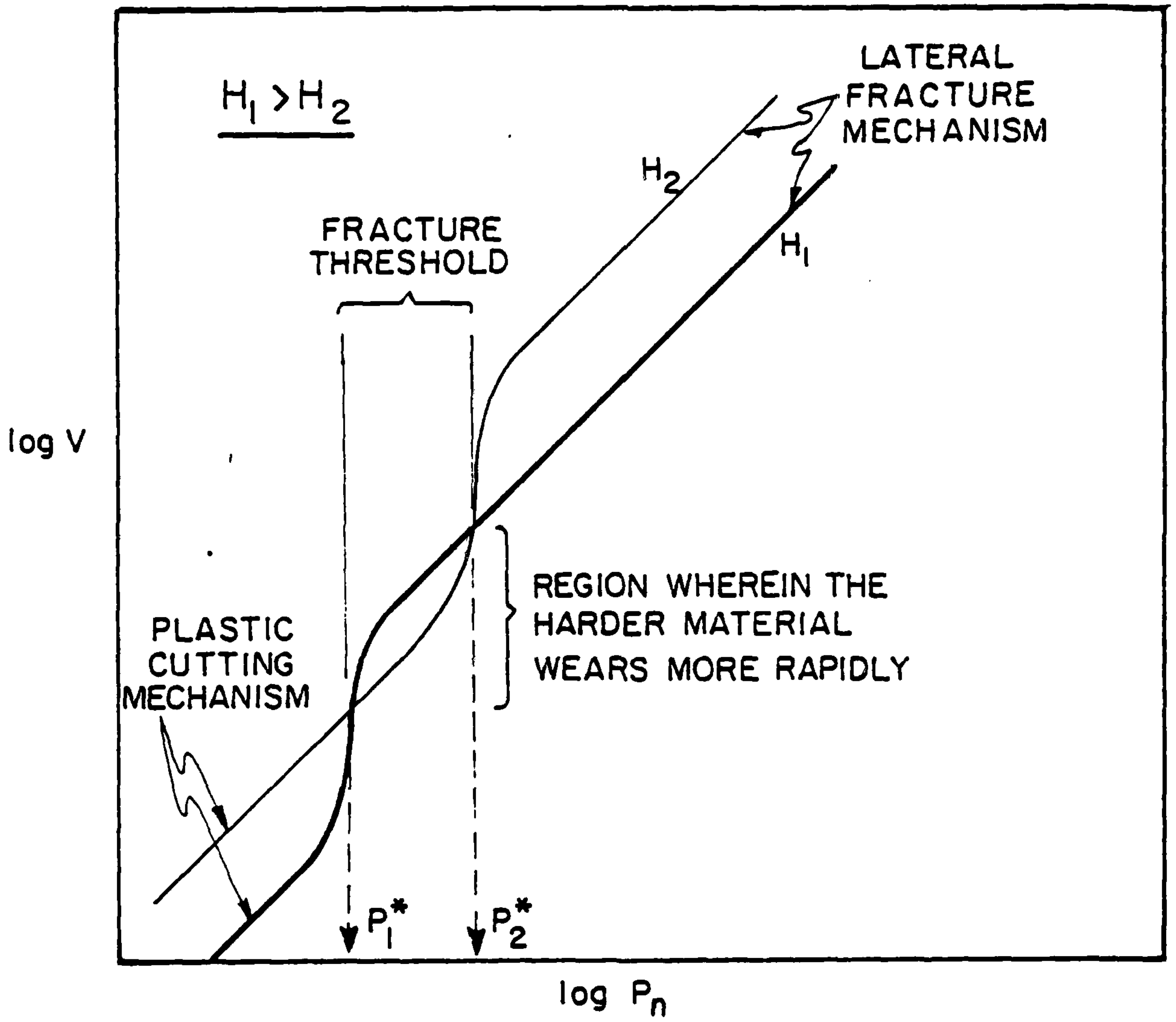
$H_1 > H_2$
LATERAL FRACTURE MECHANISM
H_2
H_1
FRACTURE THRESHOLD
log V
REGION WHEREIN THE HARDER MATERIAL WEARS MORE RAPIDLY
PLASTIC CUTTING MECHANISM
P_1^*
P_2^*
log P_n

XBL 8011-6356

Fig. 6

CHAPTER IX

PARTICLE-SIZE DISTRIBUTION EFFECTS ON SOLID PARTICLE EROSION OF BRITTLE MATERIALS

by

*D. B. Marshall, *A. G. Evans, **M. E. Gulden,

***J. L. Routbort and ***R. O. Scattergood

*Department of Materials Science and Mineral Engineering,
University of California,
Berkeley, CA 94720

**Solar Turbines, San Diego, CA 92101

***Argone National Laboratory, Argonne, IL 60439

SUMMARY

The effects of distributions of projectile size and velocity on the erosion of brittle materials is assessed. Strong dependencies of erosion rate on the width of the particle-size distribution and on the velocity characteristics of the erosion equipment are predicted. The predictions are confirmed by experiment. The results indicate that careful design of controlled erosion experiments is essential, in order to avoid misleading predictions of in-service erosion rates. The implications of the analysis for the interpretation of threshold effects and for experiments designed to verify erosion theories are also discussed.

1. INTRODUCTION

The extent of solid particle impact damage in brittle materials has been demonstrated, both theoretically [1-4] and experimentally [1-8], to depend strongly on the size and velocity of the impacting particles, as well as the relevent material properties (hardness, toughness, elastic modulus, density, acoustic impedance). In any experimental, or in-service exposure involving multiple impacts, the sizes and velocities of the projectiles are distributed over a finite range. The velocity and size distributions must be incorporated into damage analyses. Strength degradation properties are simply determined by the maximum projectile size and velocity, which dictate the most severe damage. Material removal processes, on the other hand, are cumulative and are therefore determined by the entire particle size and velocity distributions. Previous erosion analyses have been based on velocity and size parameters defined simply in terms of the mean projectile diameter and velocity. In this paper the influence on erosion of an additional parameter, the particle size variance, is assessed. The implications of the analysis for the controlled experimental measurement of in-service erosion rates, for experiments designed to test erosion theories, and for the interpretation of threshold effects are discussed. The analysis is confined to the elastic/plastic regime relevent to angular, hard particles [1-4].

Two fundamentally different erosion test configurations are in current use. In one, the projectiles are accelerated in a gas stream and the particle velocity, for a given gas stream velocity, is dependent upon the particle size [9]. In the other, which simulates a target moving through stationar particles, the relative velocity is independent of particle size [10]. The influence of a particle size distribution would be expected to differ in these two cases. The difference is assessed and the predictions confirmed by experiment.

2. ANALYSIS

The general features of single particle impact damage in the elastic/plastic regime are relatively insensitive to projectile shape and mechanical properties. The fracture pattern shows strong similarity to the damage produced by quasi-static indentation [1,5]. Most notably, two primary types of fracture have been identified. Half-penny shaped radial/median cracks develop normal to the target surface. These cracks control the strength properties. Lateral cracks form parallel to the target surface and are centered near the base of the plastically deformed zone. Propagation of the lateral cracks to the surface produces material removal.

Existing erosion models are based on analysis of the volume of material removed by the lateral cracks in single particle impact. Interaction effects are assumed to be negligible, so that the cumulative effect of multiple impacts is obtained by summing the volumes removed by individual (independent) impacts. Two quantitative models have been developed for predicting the erosion rate, E, (volume loss per impact). One is based upon analysis of quosi-static indentation [1,2] and employs an upper bound quasi-static impulse load (determined by equating the projectile kinetic energy to the work required to produce the elastic/plastic indentation). The resulting erosion rate is

$$E = v^{2.4} R_p^{3.7} \rho_p^{1.2} K_c^{-1.3} H^{0.1} \qquad (1)$$

where v, R_p, and ρ_p are the projectile velocity, diameter and density, and K_c and H are the target toughness and hardness. The other model is based on a dynamic analysis of the elastic/plastic stress field, and gives the result [3,4];

$$E = v^{3.2} R_p^{3.7} \rho_p^{0.25} K_c^{-1.3} H^{-0.25} \qquad (2)$$

Despite the different physical assumptions the two theories predict similar erosion rates. Here we confine our interest to particle size and velocity effects in a given projectile target system and express equations 1 and 2 as;

$$E = k\, v^n R^m \qquad (3)$$

where target material parameters are included in the constant k. The influences of projectile size and velocity distribution on the erosion rate follow directly from the explicit size and velocity dependence of eqn. 3.

Particle sizes generally conform to a logarithmic-normal distribution [11]:

$$\phi(R)dR = [1/\sigma(2\pi)^{1/2}] \exp [-(\ell nR - \ell nR_\mu)^2/2\sigma^2] d\ell nR \qquad (4)$$

where $\phi(R)dR$ is the fraction of particles with diameter between R and $R+dR$, R_μ is the median particle diameter, and σ^2 is the variance of ℓnR (Fig. 1). In the following analysis it is assumed that all particles of a given diameter impact the target at the same velocity, but the impact velocity is allowed to exhibit some dependence upon the particle diameter

(Appendix). Hence, by adopting a relation between velocity and size (Appendix, eqn. A1), the erosion rate (eqn. 3) can be expressed exclusively in terms of the particle diameter;

$$E(R) = k\, a^{n}\, R^{nx+m} \tag{5}$$

where x and a are characteristic of the erosion test configuration. The erosion resulting from a distribution of projectile sizes can be directly assessed from eqns. 4 and 5.

The erosion rate is generally measured in terms of the total volume of target removed, normalized by the calculated number of impacts. The calculated number of impacts, N, (in general not equal to the actual number N_0) is expressed in terms of the measured total mass of projectiles divided by the mass of the projectile with the median diameter:

$$N = N_0 \int_0^\infty R^3 \phi(R)\, dR / R_\mu{}^3 \tag{6}$$

With the logarithmic-normal size distribution (eqn. 4), eqn. (6) becomes

$$N = N_0 \exp(9\sigma^2/2) \,. \tag{7}$$

The total volume of target removed by N_0 impacts is

$$V = \int_0^\infty E(R)\, N_0\, \phi(R)\, dR \,, \tag{8}$$

which, in conjunction with eqns. (4) and (5) becomes

$$V = N_0\, k\, a^{n}\, R_\mu^{nx+m} \exp[\sigma^2 (nx+m)^2/2] \tag{9}$$

The measured erosion rate is therefore,

$$E = E(R_\mu) \exp \; (\sigma^2/2)[(nx+m)^2-9] \tag{10}$$

where $E(R_\mu) = k\,V_\mu^n R_\mu^m$ is the erosion rate corresponding to projectiles with the median diameter (i.e. $\sigma = 0$). A potentially strong dependence of measured erosion rate on σ is apparent.

3. EXPERIMENTAL

In order to test the predicted dependence of erosion rate on particle-size distribution, several distributions of SiC particles were prepared. The particle sizes within each distribution conformed approximately to a log-normal function, with a median diameter of 38 μm, but the variances ranged from 0.2 to 0.6 (Fig. 2). The distributions were prepared by mixing commercial SiC powders (grit sizes 120, 150, 180, 240, 280, 400, 600) in the appropriate ratios, as calculated from the measured* size distributions of each constituent.

Erosion experiments were performed using both of the test techniques described in the Appendix. Single crystal silicon† was chosen as a target material because complications associated with microstructural variability and subcritical crack growth can be exclud-d, and because impact damage in the SiC/Si projectile/target system conforms well to the elastic/plastic damage scheme described in section 2[12]. Target slabs measuring 25 x 25 x 5 mm, with (111) planes parallel to the face, were eroded at normal incidence and at a projectile velocity of 100 m s^{-1}.

---

*by sedimentation; sedigraph-L, Micromeritics Corp.

†Monsanto Commercial Products, St. Peters, Missouri.

The erosion rates were determined from measurements of the target mass loss and the mass of projectiles. Several successive measurements were performed for each experiment to ensure that the erosion rate was steady. Typical weight loss results for both erosion devices are shown in Fig. 3.

The measured erosion rates are listed in Table I and plotted in normalized form, as a function of σ , in Fig. 4. A strong dependence of erosion rate on σ is evident. The solid lines in Fig. 4 are predictions based on equation (10) with the following parameters; $n = 3$, $m = 3.7$ (experimental determination for Al_2O_3/Si system [8]), $x - 0$ for the slinger device, and $x = -0.16$ for the gas stream apparatus (Fig. A1). The normalizing factor, $E(R_\mu)$, (the erosion rate corresponding to $\sigma = 0$) was calculated from equation (10) using the same values of n, m and x, and the erosion rate measured for batch A particles. This procedure gave, $E(R_\mu) = 246\ \mu m^3$/ impact for the gas stream apparatus, and $E(R_\mu) = 305\ \mu m^3$/impact for the slinger device. With due allowances for the uncertainty in the particle size variances, the predictions and experiments show good agreement.

4. DISCUSSION

4.1 General Discussion

The dependence of erosion rate on particle size distribution is sensitive to the values of the particle velocity and size exponents n, m and x (eqn. 10). Consequently the absolute erosion rates measured by the two erosion devices (under otherwise identical conditions) are significantly different (Table I). It is of interest to examine this difference in more detail. The errors listed in Table I represent the scatter in measurements, and are therefore appropriate for comparison of results from a particular apparatus under constant operating conditions. Comparison of results from the two erosion devices requires the additional systematic error due to uncertainty in velocity calibration to be accounted. Taking $E \propto v^3$, along with 5% velocity error for the gas stream apparatus and 2% velocity error for the slinger device, the required erosion rate errors are $\approx$20% and $\approx$10% respectively. With these errors all of the results in Table I still differ significantly. However, the calculated erosion rates at $\sigma=0$ (i.e. $E(R_\mu) = 246 \pm 50$ μm^3/impact for the gas stream, and $E(R_\mu) = 305 \pm 30$ μm^3/impact for the slinger device) are consistent, indicating that the apparent inconsistency in Table I is due to the different dependencies of E on σ, arising from the different values of x.

An underlying assumption of the present analysis is that interaction affects are negligible, so that the cumulative effect of multiple impacts is given by summing the volumes removed by individual (independent) impacts. The agreement shown between prediction and experiment would appear to lend some support to the assumption. The subject of interaction effects has been addressed in two prior studies. In the first, Gulden [13] showed that interaction effects between particles of uniform size are negligible, by demonstrating the absence of an incubation period in the erosion of polished surfaces. However, an enhanced erosion rate was observed for the initial impacts by 50 μm particles on a surface which had been previously eroded by 270 μm particles. This result is consistent with the observation by Routbort et al [8] of an enhanced erosion rate from a mixture consisting of equal weight fractions of 40 μm and 270 μm particles. These results imply that the erosion rate for small particles can be increased by the prior damage produced by much larger particles. In the present experiments most of the material removal is produced by the larger particles in the distributions, so that any enhancement of the contributions of the smaller particles is not expected to influence the total erosion rate significantly. An upper-bound estimate indicates that the enhancement is less than 2%.

4.2 Implications

4.2.1 Simulation of In-Service Erosion

The strong dependence of E on σ has important implications for the use of controlled experiments to simulate in-service erosion rates. Firstly, a controlled experiment using projectiles matched in median size to the in-service projectiles, but with a narrower distribution of sizes, would result in a serious underestimate of erosion rate. The underestimate is largest for situations most closely simulated by the slinger device (e.g. target moving through a stationery dust cloud) rather than the gas stream apparatus (e.g. stationary target subjected to dust storm). Secondly, use of the gas stream apparatus for predict erosion rates for in-service conditions approximating the slinger device will also result in an underestimate (even if the actual in-service projectiles are used). Therefore careful design of controlled erosion experiments is essential.

4.2.2 Evaluation of Erosion Parameters

The result in eqn. (10) has potential implications for experiments designed to evaluate the parameters m and n in eqn. (3). These parameters are usually determined from the gradients of logarithmic plost of E vs R_μ at constant v, and E vs. v at constant R_μ. However it is immediately evident from eqn. (10), that if x or σ vary between experiments, the erosion rate will not show the functional dependence of eqn. (3). Consider first experiments involving constant particle size and varying velocities. Then σ is constant, while x is zero for the slinger device and non-zero (but constant) or the gas stream apparatus (Fig. A1). The correct dependence of erosion rate on velocity is thus obtained with both erosion devices. This result contrasts with that expected for experiments in which the velocity is held constant but the particle size varies. Then, provided that the variance remains constant for each particle size, the correct dependence of erosion rate on particle size is obtained for the slinger device, but not for the gas stream apparatus. (The constant variance condition is reasonably well satisfied, for example, by commercially sized SiC powders ($\sigma \approx 0.2$).) For the gas stream apparatus, where x varies between -0.13 at R_μ = 50 μm, and -0.32 at R_μ = 1100 μm (Fig. A1), the size exponent of the erosion rate deviates from the required value, m . However for the typical values of the erosion parameters used in this paper (n = 3, m = 3.7) an insignificant error (≈1%) in the experimental determination of m would result. Therefore it appears that, provided care is taken to use constant width particle distributions, the conventional experimental determinations of m and n yield accurate results.

4.2.3 Interpretation of Threshold Effects

The existence of a finite distribution of projectile size bears on the interpretation of threshold effects in erosion. Several studies have established that eqn. (3) is well satisfied for relatively large particle sizes and velocities. However, as a threshold is approached, the erosion rate decreases continuously below a linear extrapolation from large size-velocity data (Fig. 5) [2,8]. This behavior can be described empirically by modifying eqn. (3) to incorporate a threshold velocity v_0 and size R_0 [8];

$$E = k(v-v_0)^n \, (R-R_0)^m \qquad (11)$$

where v_0 and R_0 are determined by fitting eqn. (11) to experimental data. Equation (11) implies that the extent of cracking in single particle impacts increases continuously from zero, as the excess driving force above the threshold increases, as shown schematically by curve 1 in Fig. 6. Single particle impact and indentation studies have verified the existence of a threshold below which no cracking occurs [6,12,13]. However, at the threshold, lateral cracks usually initiate discontinuously as shown by curve 2 in Fig. 6. Erosion with uniformly sized particles would thus be expected to exhibit a corresponding discontinuous increase at the threshold. However, a distribution of particle sizes would yield a continuous increase, because (near the threshold) only that fraction of particles with radii in excess of the threshold radius would remove material. A discontinuous cracking threshold can be incorporated into the analysis of section 2 by replacing the lower integration limit in eqn. (8) by the threshold size R_0. Comparison of the corresponding prediction with data from Ref. [8] in Fig. 5 shows good agreement (similar to the agreement obtained from eqn. (11)). Distinction of the two threshold behaviors depicted in Fig. 6 is not possible from the erosion data, but the discontinuous threshold is considered to be the more plausible alternative.

5. CONCLUSIONS

The rate of material removal in the elastic/plastic damage regime is sensitive to both the distribution of projectile sizes and the velocity characteristics of the erosion apparatus. Consequently, experimental erosion measurements can appreciably underestimate in-service erosion rates if the experimental projectile size distribution is narrower than that of the in-service projectiles, or if the velocity characteristics of the experimental and in-service erosion configurations differ.

Results of experiments designed to measure the velocity and particle size exponents in the single particle erosion expression can also be influenced by the size distribution. However, under commonly used test conditions the influence is insignificant, so conventional measurements, which ignore the effect, yield accurate results.

A straightforward interpretation of erosion threshold behavior, in terms of observed single-particle damage initiation characteristics in conjunction with a projectile size distribution, is suggested.

ACKNOWLEDGMENTS

This work was supported by the U.S. Office of Naval Research, under Contract Number N00014-79-C-0159.

APPENDIX

Velocity/particle-size characteristics of erosion experiments

Two different experimental erosion facilities are used to investigate the effects of particle size distribution on erosion. In one the projectiles are introduced into a uniformly moving gas stream in a 0.95 cm diameter tube, and accelerated over a distance of 3 m before impacting the target.† The calculated velocities for a range of particle diameters and gas stream velocities are shown in Fig. A1. These calculations have been verified by direct experimental measurement using the double rotating disc method [9]. For a given gas velocity, the particle velocity can be approximated by

$$v = a\ R^{x} \qquad \text{(A1)}$$

where a and x can be taken as constants for a given experiment, provided that the range of particle diameters is restricted. Over the full range of particle sizes shown in Fig. A1 (a factor of 100) x varies between -0.13 and -0.32; in a typical experiment the range of particle diameters is about a factor of 2.

The other erosion method utilizes a "slinger" device* [10], in which the projectiles are introduced into the center of a rotating tube with open slits at both ends. After moving slowly along the tube the projectiles are thrown from the slits in a tangential direction, with the speed of the tube ends, and impact stationary targets. The experiment is performed in vacuum. Rotating double disc measurements have verified that the particle velocity is the same as the velocity of the tube ends, and independent of particle size. Therefore, for the purposes of analysis, the particle velocity can be expressed by eqn. (A1) with $x = 0$.

---

† Erosion test facility at Solar Turbines [14].

*Erosion facility at Argonne National Laboratory [15].

REFERENCES

1. B. J. Hockey and S. M. Wiederhorn, Proc. 5th Int. Conf. on Erosion by Solid and Liquid Impact, 1979, ch. 26.
2. A. W. Ruff and S. M. Wiederhorn, Treatise on Materials Science and Technology, Vol. 16, Edited by C. M. Preece, Academic Press, 1979, 69.
3. A. G. Evans, Treatise on Materials Science and Technology, Vol. 16, Edited by C. M. Preece Academic Press, 1979, 1.
4. A. G. Evans, M. E. Gulden and M. Rosenblatt, Proc. Roy. Soc. Lond., A361 (1978) 343.
5. B. J. Hockey, S. M. Wiederhorn and H. Johnson, Fracture Mechanics of Ceramics, Vol. 3, Edited by R. C. Bradt, D. P. H. Hasselman and F. F. Lange, Plenum, New York, 1978, 379.
6. A. G. Evans, Fracture Mechanics of Ceramics, Vol. 3, Edited by R. C. Bradt, D. P. H. Hasselman and F. F. Lange, Plenum, New York, 1978, 303.
7. M. E. Gulden, ASTM, STP 664, Edited by W. F. Adler, 1979, 101.
8. J. L. Routbort, R. O. Scattergood, E. W. Kay, J. Amer. Ceram. Soc., 63 (1980).
9. M. E. Gulden and A. G. Metcalfe, U. S. Office of Naval Research 4th Technical Report, Solar Turbines, San Diego, April 1978.
10. T. H. Kossel, R. O. Scattergood and A. P. L. Turner, Wear of Materials, Edited by K. C. Ludema, W. A. Glaeser and S. K. Rhee, ASME, New York, 1979, 192.
11. A. G. Evans and F. F. Lange, J. Amer. Ceram. Soc., 62 (1979) 62.
12. B. R. Lawn, B. J. Hockey and S. M. Wiederhorn, J. Mater. Sci., 15 (1980) 1207.
13. M. E. Goulden, J. Amer. Ceram. Soc., 63 (1980) 121.
14. B. R. Lawn and A. G. Evans, J. Mater. Sci., 12 (1977) 2195.
15. J. Lankford and D. L. Davidson, J. Mater. Sci., 14 (1979) 1662.

Table 1

Erosion of single crystal silicon by the silicon carbide particles of Fig. 3. Normal incidence, velocity 100 M S^{-1}.

Erosion Apparatus	Erosion Rate μm³/impact			
	Batch A	Batch B	Batch C	Batch D
Gas Stream	254 ± 10	262 ± 10		325 ± 10
Slinger	340 ± 10	492 ± 10	527 ± 10	646 ± 10

FIGURE CAPTIONS

1. Typical probability distribution for particle distributions (logarithmic-normal).
2. Size distribution for three batches of SiC particles used in erosion experiments.
3. Typical measurements of target weight loss as a function of mass of projectiles. Batch A SiC particles, $v = 100\ \mathrm{ms}^{-1}$, normal incidence, silicon target.
4. Erosion rate as a function of particle distribution width for two erosion devices. Data obtained from the SiC particles of Fig. 3 impacting a silicon target at normal incidence and $v = 100\ \mathrm{ms}^{-1}$. Solid curves are predictions from eqn. (11).
5. Erosion threshold. Data from Ref. [4]; Al_2O_3 projectiles impacting silicon target, normal incidence, $v = 107\ \mathrm{ms}^{-1}$. Straight line fitted to data. Solid line for $R \lesssim 40\ \mu m$ predicted from the analysis of section 2.2, with lower integration limit in eqn. (9) replaced by $R_0 = 27\ \mu m$.
6. Schematic representation of single particle contact damage near the threshold.

A1. Velocity/particle-size relation for gas-stream erosion apparatus.

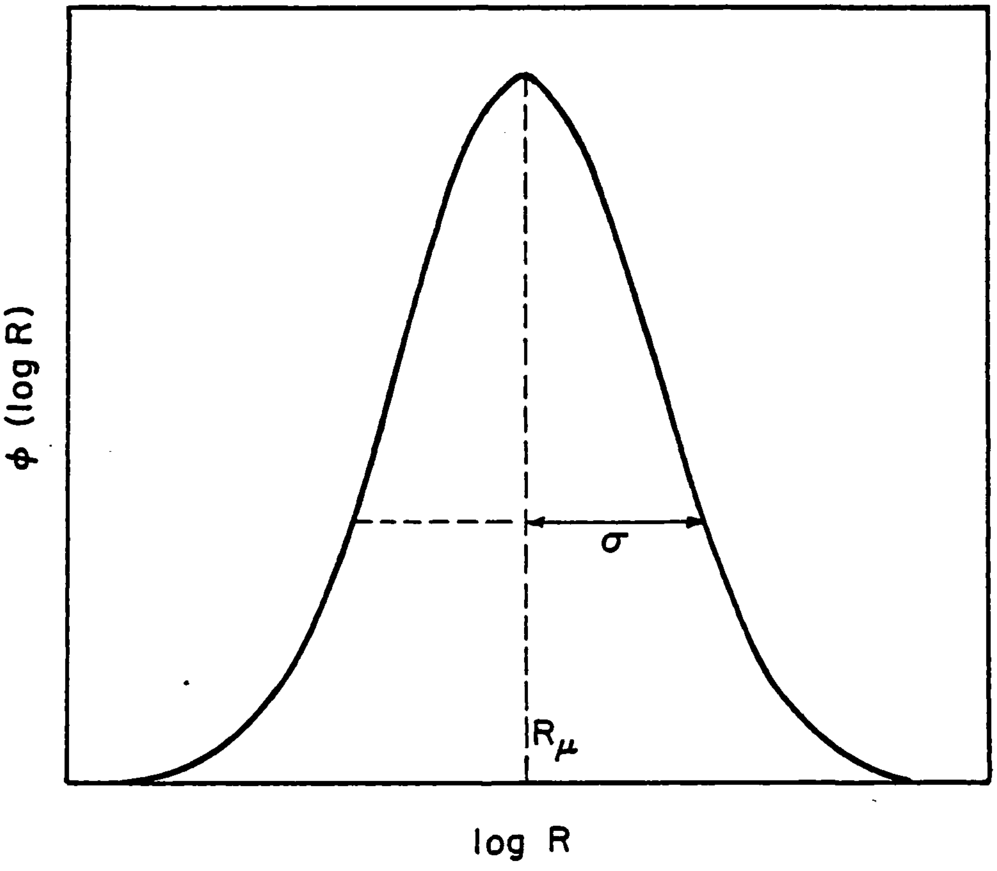

XBL 8012-13449

Fig. 1

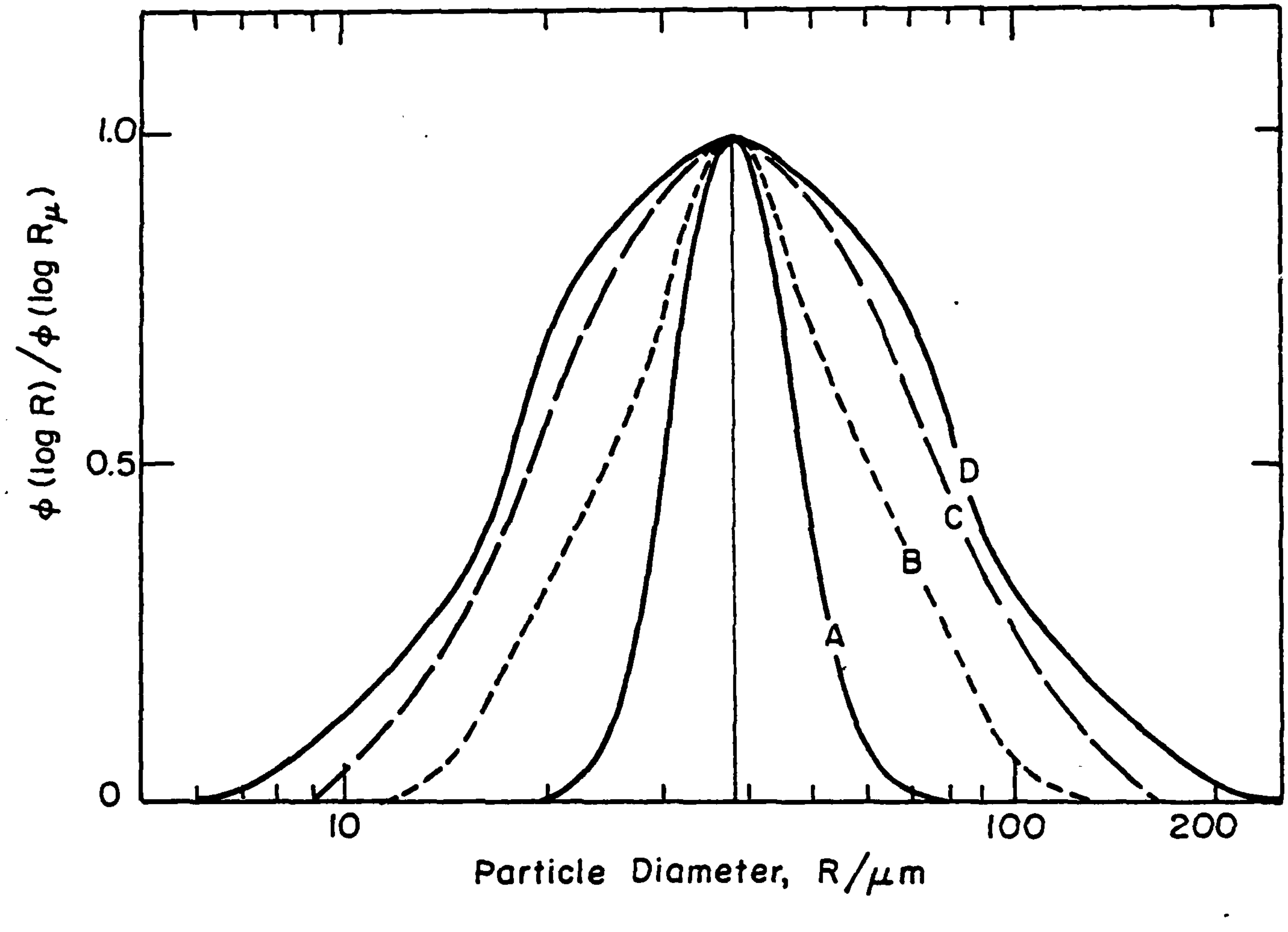
1.0
0.5
0
φ (log R) / φ (log R$_\mu$)
A
B
C
D
10
100
200
Particle Diameter, R/μm
XBL8012-13450

Fig. 2

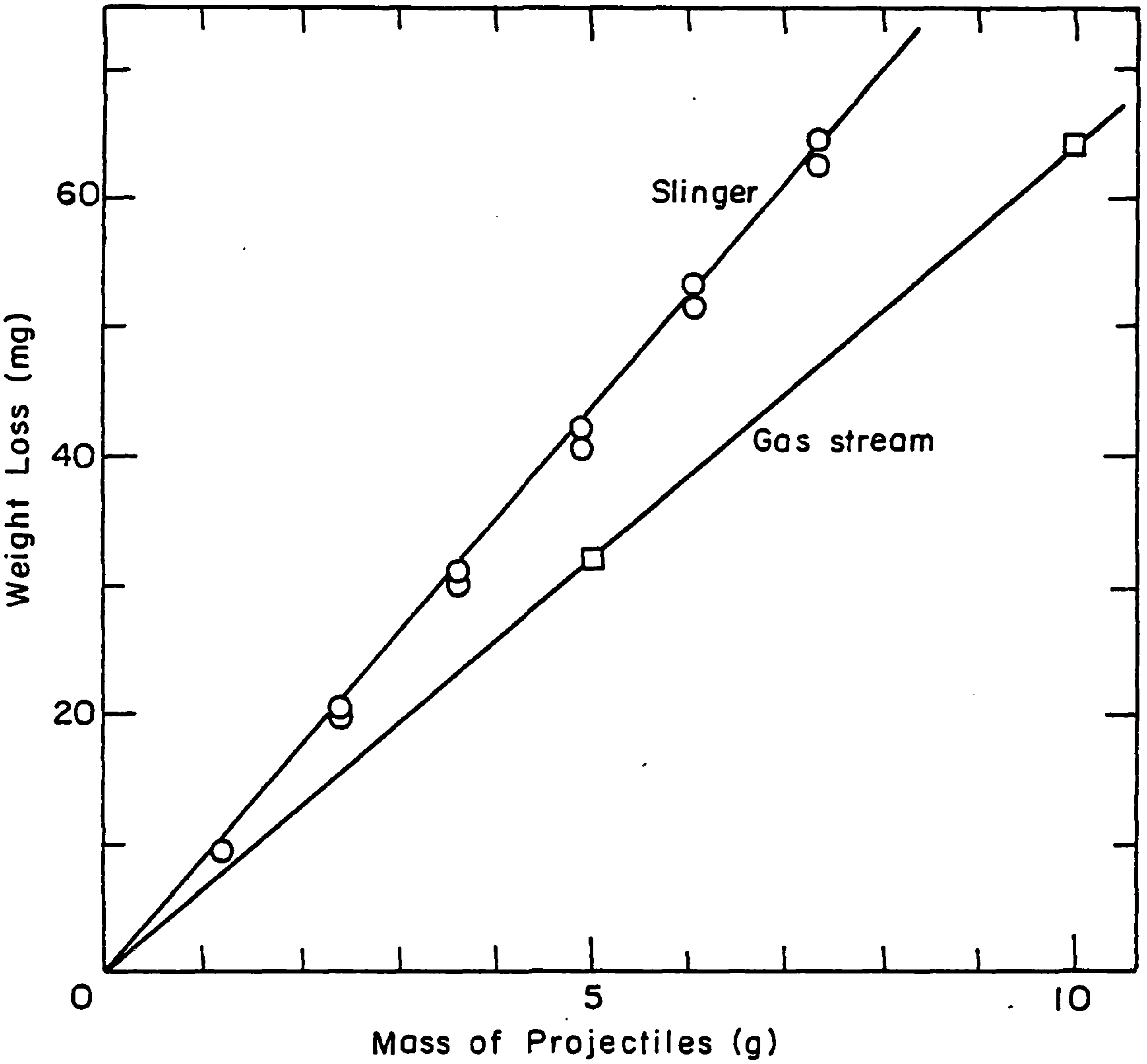

XBL 8012-13451

Fig. 3

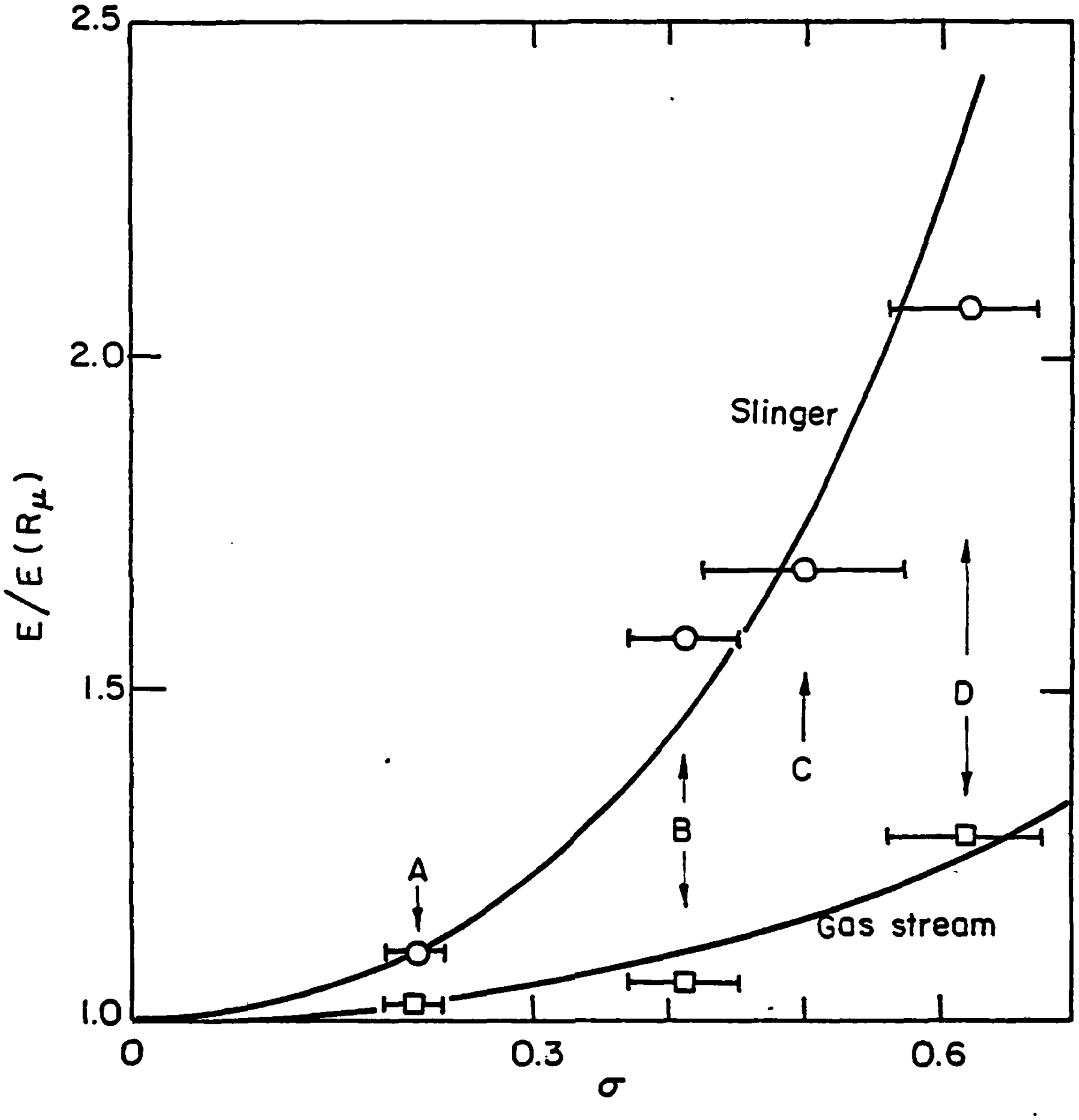

XBL8012-13452

Fig. 4

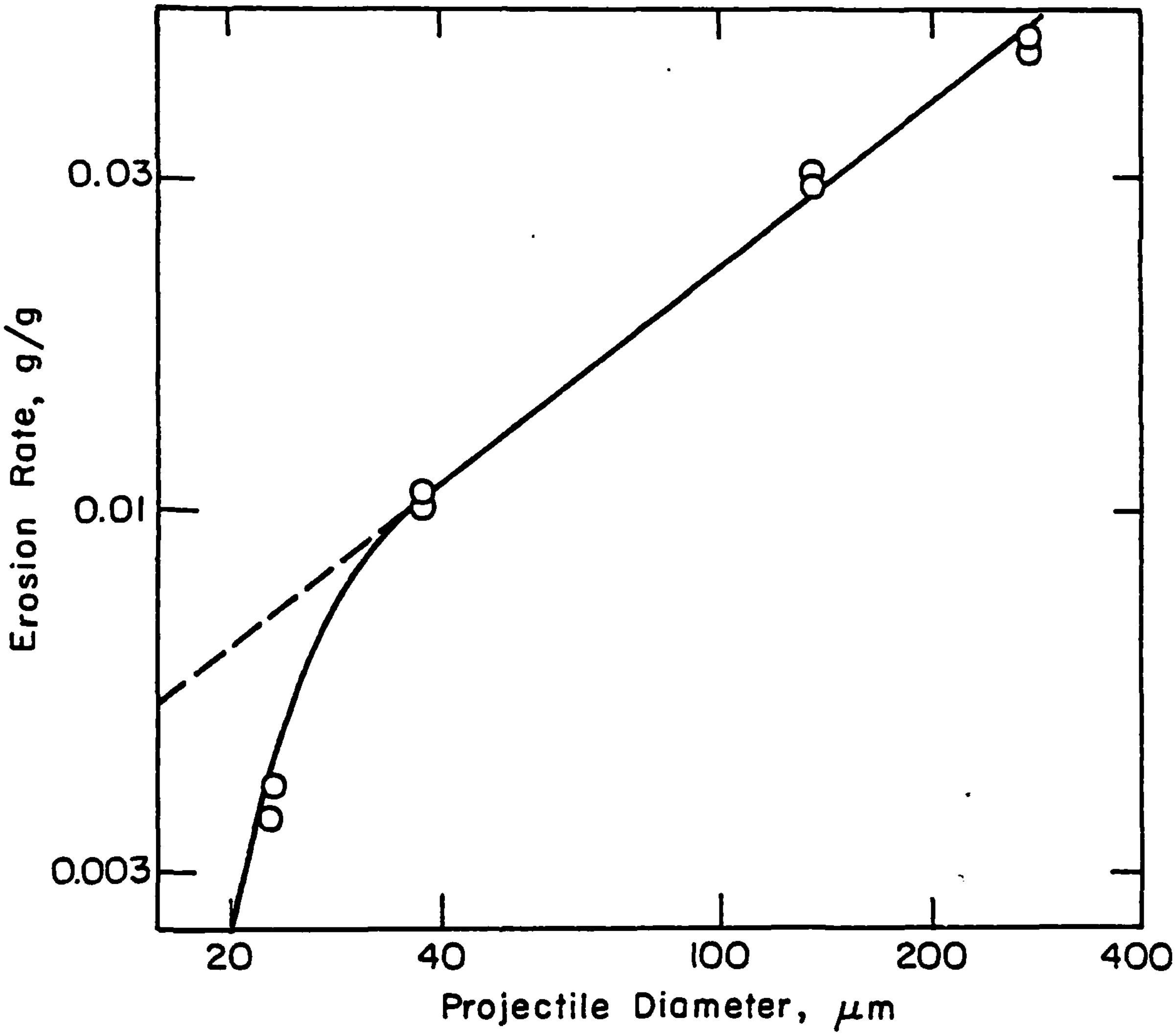

XBL8012-13453

Fig. 5

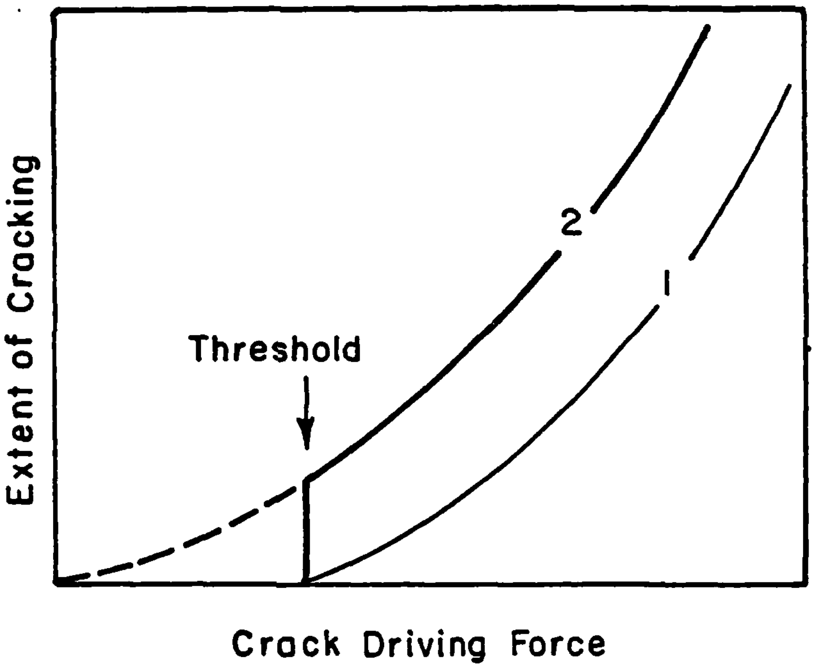

XBL 8012-13454

Fig. 6

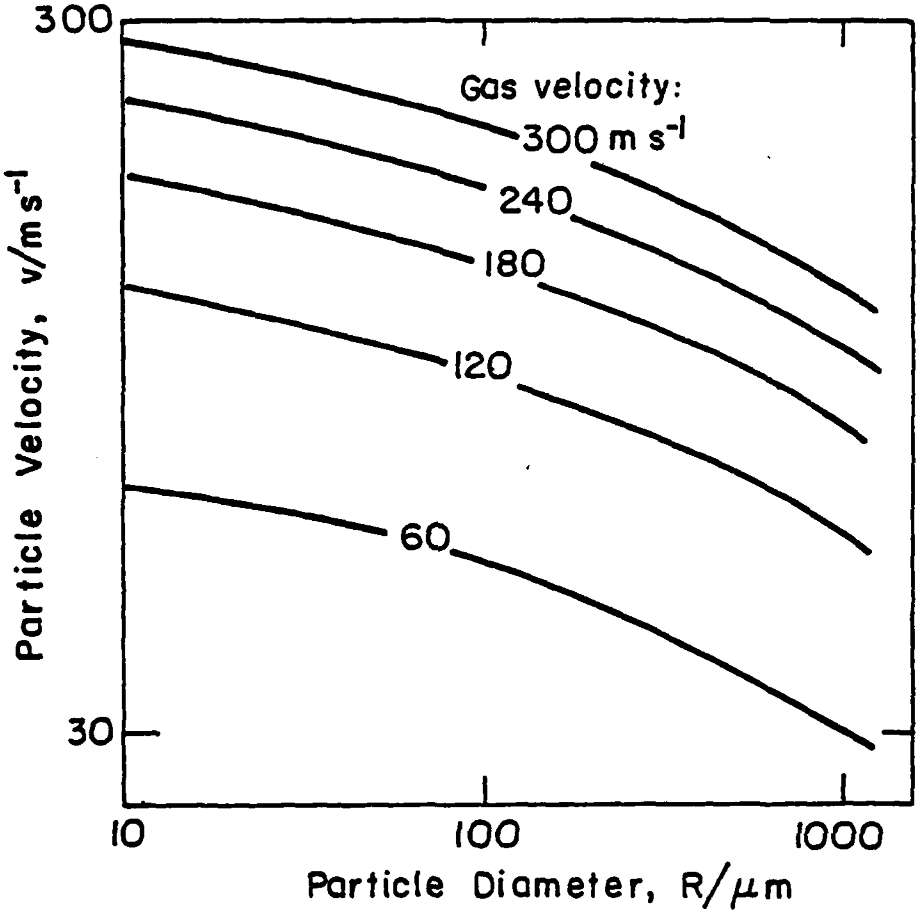

XBL 8012-13455

Fig. A1

LMED

8